Pathways to Probing the Circumstellar Environments: A Search for the Rarest Eclipses Across Stellar Populations

Anastasios Tzanidakis

A dissertation
submitted in partial fulfillment of the
requirements for the degree of

Doctor of Philosophy

University of Washington

2026

Reading Committee:

James R. A. Davenport, Chair

Eric C. Bellm

Emily M. Levesque

Program Authorized to Offer Degree:
Department of Astronomy

©Copyright 2026
Anastasios Tzanidakis

University of Washington

Abstract

Pathways to Probing the Circumstellar Environments: A Search for the Rarest Eclipses Across Stellar Populations

Anastasios Tzanidakis

Chair of the Supervisory Committee:
Professor James R. A. Davenport
Astronomy

When circumstellar dust orbiting a star crosses our line of sight, it leaves a fingerprint in the light curve: a complex dimming event that carries information about stellar evolution, planet formation, and the dynamics of circumstellar material that no other observational technique can access at scale. These dimming phenomena are rare, diverse, and until recently, were largely hidden by the lack of a digital footprint across the dynamic night sky. Their discovery required photometric baselines spanning years, sky coverage spanning billions of stars, and the computational infrastructure to flag anomalies in large survey catalogs. The following dissertation focuses on a subclass of three types of rare circumstellar eclipses that probe stellar and planetary formation. We begin with the first large-scale systematic search for main-sequence dipper stars, conducted across 63 million FGK stars using the Zwicky Transient Facility (ZTF) survey and Gaia EDR3. Using a novel light-curve scoring algorithm, we identify 81 new dipper candidates exhibiting diverse dimming morphologies, from symmetric to highly asymmetric, spanning timescales of days to years, with no detectable infrared excess or periodicity in many cases. We investigate multiple classification scenarios and compare them against typical Young Stellar Object (YSO) variability. We conclude that the dimming events are driven either by transiting circumstellar clumps or occultations by substellar companions with disks, establishing the first comprehensive census of main-sequence dippers and placing new constraints on the occurrence rates of circumstellar material around solar analogs. We then turn to the discovery of Gaia17bpp, a cool M0-III

giant star that underwent a single deep dimming event of $\sim$4.5 magnitudes lasting over 6.5 years. Gaia17bpp represents one of the longest and deepest stellar occultations recorded in the modern photometric era to date. Using optical-to-infrared spectral energy distribution fitting and a monochromatic transit model, we constrain the occulting body to be a large, optically thick disk with a radius of $\sim$1.4 au, moving at a slow transverse velocity of $\sim$0.005 km s^{-1}. We propose that Gaia17bpp belongs to a rare class of binary systems analogous to ϵ Aurigae, in which a secondary star enshrouded by a circumstellar disk periodically eclipses an evolved giant primary. The discovery of Gaia17bpp demonstrates that the disk-eclipse phenomenon is not limited to young stellar systems, and that long photometric baselines are essential for recovering such events. Finally, we report the discovery of Gaia20ehk (Gaia-GIC-1), the first giant impact candidate identified by Gaia. This system exhibits a striking anticorrelation between its optical and mid-infrared light curves: large-amplitude irregular optical dimming accompanied by sustained infrared brightening over more than four years. We identify the host as a likely young F-type star, detect a significant $\sim$380.5-day periodic modulation in the pre-outburst light curve consistent with a $\sim$1.1 au orbit, and measure a dust temperature of $\sim$900 K and a minimum dust mass of 4×10^{20} kg from WISE photometry. We interpret Gaia-GIC-1 as the afterglow of a recent catastrophic collision between two planetesimals, producing a clumpy debris cloud on a bound orbit, one of only a handful of such systems known, and the first discovered through Gaia's Photometric Science Alerts. In summary, these three results trace circumstellar dust across the full arc of stellar evolution: from the planet-forming environments of young stars, to the mature main sequence, to evolved giant systems. The following thesis demonstrates that rare dust-driven occultations are discoverable at scale when time-domain survey infrastructure is paired with targeted algorithmic search strategies, and that the coming era of the Vera C. Rubin Observatory's Legacy Survey of Space and Time (LSST) will vastly expand the known population of such systems. This thesis establishes both the observational framework and the scientific context needed to interpret that forthcoming census.

DEDICATION

To my wife, *Lily*, the rarest star I will ever know. Your love has been my guiding constellation through the darkest nights of this journey. You have been beside me from day one, through the highest pinnacles and the quietest lows. No one in this world has ever shown up for me the way you do. Over ten years ago, I made the questionable choice to take you to an astrophysics lecture at the American Museum of Natural History on our second date. I was sure I had scared you off forever. Instead, you listened, you smiled, and somehow, you fell in love with me at the forefront of what I was most passionate about: the stars. Since then, you have moved across the country with me to Seattle so I can chase my dreams. You have nurtured my soul with endless hours of deep conversations, wild adventures around the world, and a devotion that always grounded me. Loving someone as extraordinarily intelligent and compassionate as you has taught me a simple truth: love and compassion are the strongest forces in nature. You are the reason I was able to voyage this far. There are no words to say how deeply I love you, except to quote Stevie Wonder and remind you, *you can rest your mind assure that I'll be loving you, always.*

With equal devotion, I dedicate this dissertation to my parents, Lemonia and Haralampos, whom I owe it all. Growing up near the sea and under clear skies, I was surrounded by a family and a community that encouraged me to look up. My parents nurtured that endless curiosity without question. Throughout the years, they made quiet, unconditional sacrifices so I could chase my dreams. Nearly a decade ago, they made the long journey back to the United States from Greece. Through many years of hard work, they built a life that gave me the privilege of becoming the first in our family to earn a college degree, and now my life dream is to obtain a doctoral degree. Mom and Dad, I hope I can give my future children half as much as you have given me. I love you.

ACKNOWLEDGMENTS

First and foremost, I am deeply grateful to my advisors, without whom reaching this milestone would have been impossible. As my primary advisor, **Jim Davenport** taught me what it takes to be a critical, independent scientist, an engaging communicator, and a researcher driven by genuine passion. He has always gone above and beyond to ensure his students can pursue their passions, no matter the obstacle. When I made my first discovery in graduate school, I often struggled to grasp the boundaries of what we can learn from nature, yet Jim was right there with me at the edge of that understanding. He is the reason I fell in love with telling the stories of the stars, and I owe my lifelong passion for this field to his guidance and enthusiasm. I am beyond excited for the years ahead and for the many more discoveries we will share. **Eric Bellm** has always been a steadfast force of support in graduate school that guided me through the most challenging career and scientific questions. I always deeply enjoyed learning from him; his remarkable patience created a space where I felt always safe to ask tough questions, fail, and ultimately grow. Working alongside Eric has not only shaped the way I approach science, but also shown me the kind of compassionate mentor I hope to become. I am also deeply grateful to have had **Emily Levesque** on my committee and as a mentor throughout my graduate studies. Whenever I brought a bizarre new star system to discuss, she would always respond with boundless excitement and sharp and illuminating ideas about what we can learn. That passion was truly contagious, and her guidance taught me how to ask the deep, critical questions that fundamentally shaped my research approach. Her thoughtful feedback made many parts of this thesis stronger, and I am so thankful for her constant encouragement and shared love for stars. I would also like to acknowledge and thank **Saadia Pekkanen**, who served as my Graduate School Representative, for the many enlightening conversations we shared about the broader societal implications of astronomical research. I have also been fortunate to have had many incredible mentors who have nurtured my career and helped me reach this point. I would be remiss not to mention my very first research mentor, **Allyson Sheffield**, who took a chance on me over a decade ago. Allyson was the true catalyst for my journey, igniting the initial spark that made me fall in love with astronomical research and observational astronomy. With endless patience, Allyson taught me the core fundamentals of what it meant to be a scientist and a compassionate mentor. Her unconditional belief in her students left a lasting mark on me, and I aspire to lead and mentor others with the same generosity and warmth. To the undergraduate and graduate students, faculty, and staff of the University of Washington, notably to my close friends and colleagues **Tom Wagg**, **David Wang**, **Gabriella Suissa**, **Daniel Merino**, the Fab-Five^{TM}, the Stellar Cartography, Carpe Datum and Massive Stars group, the DiRAC Institute Postdocs, **Jess Werk**, **Eric Agol**, **Andy Connolly**, the **LINCC Frameworks Group**, and UW Astronomy staff **Tyneshia Valdez**, **Elisa Quintana**, **Jess Ness**, **Liza Young**, and so many others. Thank you for making UW always feel like home. Your support over the years in so many aspects of my career development, friendship, and learning

alongside you will always be the most cherished memory. Lastly, to the UW Planetarium community. I am personally overwhelmed with so much gratitude for what was an immense privilege serving as a director for three years during my graduate studies. The UW Planetarium community gave me so much, and I am deeply grateful for everyone's contributions to the planetarium over the past years. Watching students from all corners of UW lead their own astronomy planetarium programs and communicate science with visitors has been one of the highlights of my time at UW and reminds me why this work matters so deeply. I am continually inspired by their commitment and the countless hours they all have dedicated to service, uplifting each other and sharing your passion with thousands of visitors. Thank you all for your incredible service, collaboration, and friendship.

Beyond the world of astronomy, countless shining stars supported my Ph.D. journey, whom I can never thank enough. First, to my brothers, **Manoli** and **George**, who, as my older brothers, gave me the best kind of tough love, taught me the true meaning of hard work, and always had my back. You guys looked out for me and loved me unconditionally every step of the way. To my loving grandparents, **Anastasios** and **Afrodite**, who made so many sacrifices for their children and grandchildren to have a brighter future in America. To my in-laws, **Jeff** and **Jayne**, who welcomed me as their own child, and **Eliza**, the best sister-in-law I could ever ask for. I am so lucky to call you my family. You are the invisible string that held me together throughout this journey. To my childhood best friend and brother, **Emil**. There is nobody that I know who is as hardworking and passionate as you are, and who has always been a source of inspiration. You have been at the corner of so many milestones, supporting every wacky idea, and have always nurtured my deep love for astronomy. Over a decade ago, we both decided to chase our dreams in science, which sadly came at the expense of my first friendship heartbreak: living on separate continents. Though an entire ocean keeps us apart, I am so grateful that our bond has remained unshakable, and for the countless ways you have shown up for me despite distance. I cannot wait for your turn next, Dr. Pano. To **Etiowo** and **Liz**, there are no friends as loving, caring, and wildly thoughtful as you two. Our endless hours of spikeball, ridiculous karaoke mash-ups, and questionable custom music videos brought me the most healing laughter during graduate school. More than that, those moments kept my spirit whole. Thank you for always creating an open space where I can completely unwind, for loving me through every high and low, and for being the bright, joyous light that carried me through this journey. To **Abdullah**, **Andrea**, **Gabriella**, **Emmett**, and **Tom**, you are the most extraordinary, loving, caring, and thoughtful human beings I know. You are all my absolute role models of what it means to show up unconditionally for your friends, to lead with love as devoted parents, and to pursue your passion with brilliant intellect. Thank you for setting such an inspiring example of how to live, love, and excel, and I am so deeply grateful to call you my friends. To **Anuj**, you completely transformed the way I look at the world. Through our deep, late-night conversations about life, you taught me how to be fiercely independent, curious, and truly embrace living. You were a vital anchor who helped me keep pushing through the hardest stretches of my graduate career. I will forever be grateful to you and **Niki** for being so genuinely invested in my success, for asking endless questions about astronomy, and for showing up for me when I needed it the most. I am so unbelievably lucky to have you both. Finally, to the Seattle Greek Lake Pickleball community, who during the last few years of writing my thesis provided the much-needed break and fulfillment outside of work.

CONTENTS

Dedication i

Acknowledgments ii

Contents iv

1 Introduction 2

1 Preface . . . 2
2 Time-Domain Surveys as Discovery Engines . . . 3
3 Astrophysics of Stellar Eclipses . . . 4
4 Classes of Rare Transits . . . 8
4.1 Circumstellar Dust . . . 9
4.2 Disk Eclipses Around Stars . . . 13
5 Structure and Outline . . . 16

2 Main Sequence Dipper Stars 18

1 Preface . . . 19
2 Introduction . . . 19
3 Photometric Data . . . 22
3.1 ZTF Ubercalibrated . . . 22
4 Methods . . . 22
4.1 Gaia FGK Dwarf Selection . . . 22
4.2 Finding Dips . . . 23
4.3 Dipper Scoring Metric . . . 25
4.4 Addressing ZTF Systematics . . . 26
4.5 Injection-Recovery Simulations . . . 28
4.6 Discovery Process . . . 30
5 Properties . . . 31
5.1 Timescales and Depths . . . 31
5.2 Light Curve Shapes . . . 35
5.3 Light Color Evolution Properties . . . 36
5.4 Demographics . . . 38
5.5 Periodicity . . . 43
5.6 Infrared Properties . . . 44
5.7 Auxiliary Surveys . . . 45
6 Discussion . . . 47
6.1 Classification Scenarios . . . 47
7 Conclusion . . . 55
7.1 Acknowledgments . . . 56
8 Appendix . . . 58

3 Disks Eclipses Across Stellar Age **70**
1 Gaia17bpp: A Giant Star with the Deepest and Longest Known Dimming Event 71
2 Introduction . . . 71
3 Data . . . 72
3.1 Gaia . . . 72
3.2 WISE . . . 74
3.3 MAST . . . 75
3.4 Archival Photometry . . . 76
3.5 Spectroscopy . . . 76
3.6 Follow-up Photometry . . . 77
4 Primary Star . . . 78
4.1 Spectral Energy Distribution . . . 78
4.2 Primary Star Variability . . . 80
5 Dimming Event Properties . . . 82
5.1 Light Curve Properties: Optical to IR . . . 82
6 Discussion . . . 84
6.1 Intrinsic Variability Scenarios . . . 84
6.2 Extrinsic Variability Scenarios . . . 86
6.3 Occulting Disk Model . . . 87
7 Conclusion . . . 90
8 Acknowledgments . . . 92
4 A Catastrophic Planetesimal Collision Candidate **93**
1 Preface . . . 94
2 Introduction . . . 94
3 Data . . . 95
3.1 Optical Light Curves . . . 95
3.2 Infrared Light Curve . . . 96
3.3 Spectroscopy . . . 97
3.4 Spectral Energy Distribution . . . 98
4 Properties . . . 99
4.1 Light Curve Properties . . . 99
4.2 Periodicity . . . 101
5 Discussion . . . 103
5.1 Planetary Collision Impact Scenario . . . 103
5.2 Alternative Scenarios . . . 105
6 Conclusion . . . 106
7 Acknowledgments . . . 107
1 Cluster Membership Probability . . . 109
A Conclusion **110**
1 Future Work . . . 111
1.1 Gaia-GIC-2: Planet Collision with Enhanced Accretion? . . . 111
2 Surveys and Data of the Future . . . 114
2.1 The Rubin Observatory as A Real-Time Discovery Engine . . . 114
Bibliography **116**

CHAPTER 1

INTRODUCTION

Stars,
Never thought you'd fade away
Thought I'd see you in the light of day
Thought you'd take me as I am –
Thought you'd tell me who I am –
Thought you'd see me as I am

– J. Collier

1 Preface

Circumstellar dust eclipsing its host star is detectable at every stage of stellar evolution: from young planet-forming systems to mature main-sequence stars to evolved giants. The telltale signs of circumstellar occultations are a rare window into astrophysics that has otherwise been inaccessible for centuries – largely due to the digital footprint of the night sky. Yet, at the remarkable pace of mapping the Milky Way and monitoring billions of stars, we are arriving at a standpoint to understand the locus of *where* stellar populations exist, and *how* their average photometric properties are correlated. This can enable the search for *rare stellar eclipses* through *contextual variability*, when searching for interlopers. As will be discussed in this thesis, circumstellar dust in a variety of stellar environments can drive *rare stellar variability*. The advent of synoptic, wide-field, time-domain surveys now provides the photometric baselines, sky coverage, sensitivity, and alert infrastructure needed to find these events systematically. This thesis presents the discovery and characterization of three classes of such events, building toward a unified picture of how circumstellar material shapes rare stellar occultations and is shaped by stars and planets across their lifetimes.

2 Time-Domain Surveys as Discovery Engines

Every star has a story. Stellar variability offers one of the most revealing ways to tell it. Time-domain astronomy (TDA) – the systematic, repeating photometric monitoring of the sky – has become one of many powerful frameworks for discovery in contemporary astrophysics by collecting data on large scales (Paczynski, 1997). Some of the most enduring contributions of TDA include the discovery of the Period-Luminosity relationship through stellar variables (Leavitt & Pickering, 1912), which ultimately enabled distance measurements that revealed the scale of the expanding universe (Breuval et al., 2025; Fernie, 1969). The systematic collection of stellar light curves dates back to the photographic plate archives of the Harvard College Observatory in the late 1800s (Grindlay et al., 2012; Hoffleit, 1972) and many others around the world. Yet, observations of stellar variability extend far earlier – with records and oral traditions from indigenous communities suggesting that humanity has tracked the changing sky for millennia (Schaefer, 2018).

In the last century, the number of cataloged stellar variables has grown by several orders of magnitude (Catelan, 2023), driven by the rapid proliferation of wide-field time-domain surveys (Djorgovski et al., 2012). Together, these surveys now rank among the enormous data-producing enterprises in observational astronomy (Djorgovski et al., 2012), repeatedly imaging the sky at unprecedented cadence, depth, and precision. Landmark surveys include the Optical Gravitational Lensing Experiment (OGLE; Udalski et al. 1992), the Palomar Transient Factory (PTF; Law et al. 2009), the Catalina Real-Time Sky Survey (CRTS; Drake et al. 2012), the All-Sky Automated Survey for Supernovae (ASAS-SN; Kochanek et al. 2017a), Pan-STARRS (PS1; Chambers et al. 2016), and the Zwicky Transient Facility (ZTF; Bellm et al. 2019a), among others. Across the expanding catalogs of stellar variables, a central principle that drives the search and characterization of them is through deep astrophysical processes connected to stellar theory (Becker, 1987). Stellar variables are not distributed arbitrarily, but instead occupy discrete and well-defined regions of the Hertzsprung-Russell (HR) diagram (Eyer & Mowlavi, 2008; Szabados, 2014). Stellar variability in contemporary means is divided into two broad classifications: *extrinsic*, and *intrinsic*, as illustrated in the variability classification tree in Figure 1.2, including many more subdivisions of classification. The temperature, luminosity, and evolutionary state together govern the dominant variability mechanism in any given star: from the classical pulsation instability strips, to eruptive and eclipsing regimes (Fetherolf et al., 2023; Gaia Collaboration et al., 2019a; Hwang et al., 2024). To understand the underlying astrophysics of stellar variables at scale, and to find the rare needles in the cosmic haystack, stellar variable classification is a necessity.

The central challenge in exploiting the growing census of stellar variables is *classification* (Mahabal et al., 2011). Knowing the type of any given variable star is essential since it transforms a photometric time-series into a physically interpretable object and enables population-level studies across stellar evolution and Galactic structure (LSST Science Collaboration et al., 2009). On the contrary, reliably classifying every variable star is far from straightforward. The most physically robust classification requires, in addition, spectroscopic follow-up, which constrains stellar parameters and can thus yield higher classification completeness (Richards et al., 2011). Surveys such as the Sloan Digital Sky Survey (SDSS; York

et al. (2000)) demonstrated the power of this approach in targeted regimes, for example, quasar variability Wilhite et al. (2005), but full comprehensive spectroscopic coverage across the entire sky at high classification completeness remains the next frontier (Kollmeier et al., 2017).

The classification of stellar variables has motivated a large body of machine learning (ML) literature. A foundational approach is to represent each light curve as a vector of statistical descriptions (*features*), encoding period, amplitude, skewness, and other time-series properties, which can then be passed to a supervised classifier (Bloom & Richards, 2012; Richards et al., 2011). This framework, pioneered by Debosscher et al. (2007), and further extended by Richards et al. (2011) using a random forest on a 25-class dataset of 1542 variable stars, established the standard practice for automated variable star classification (Aguirre et al., 2019; Benavente et al., 2017; Debosscher et al., 2007; Mackenzie et al., 2016; Nun et al., 2015; Pichara et al., 2016; Sarro et al., 2009). The power of ML-driven frameworks and vectorizing light curve features is such that they can operate on the incoming stream of alerts, as demonstrated on the ZTF alerts by the ALeRCE Broker System and classify transients and variable sources with high precision (Sánchez-Sáez et al., 2021). In the pursuit of generating large classification catalogs of variable stars, there is a search for outliers (needles in the haystack), which often embed new astrophysics (Ishida et al., 2021). Complementing ML-supervised approaches, unsupervised anomaly detection methods have also been developed to identify objects that deviate from any known classes (Rebbapragada et al., 2009). More recently, these techniques have been applied at survey scale, including anomaly detection in ZTF (Malanchev et al., 2021), and the search for analogs of the enigmatic Boyajian's star (Giles & Walkowicz, 2020) using a K-nearest neighbor distance from light curve features. Despite the advances in supervised and unsupervised classification of stellar variables, the sheer discovery rate of new variable classes is projected to reach the billions with the Vera C. Rubin Observatory Legacy Survey of Space and Time (LSST; Ivezić et al. (2019)). Human expert classification at the survey scale is infeasible. We have entered an era in which automated, data-driven methods for discovery are no longer convenient but fully necessary. Thus, the challenge of discovering the rare gems in the vast survey data is an increasing challenge.

3 Astrophysics of Stellar Eclipses

In this next section, I will discuss the general astrophysical principles behind stellar eclipses, which this thesis mostly emphasizes. A stellar *eclipse* is defined as when one celestial body passes in front of another. A *transit* is defined as when the smaller body passes in front of the larger body, and *occultation* when the smaller body passes *behind* the larger body. Stellar eclipses are powerful diagnostic tools used in observational astronomy to understand the physical properties of the eclipsing bodies. Generally, under the assumption that an eclipse occurs between solid bodies, the change in observed flux (i.e., transit depth) is defined as the geometric radius ratio:

$$\Delta\delta = \left(\frac{R_{obj}}{R_*}\right)^2, \tag{1.1}$$

where R_{obj} is the radius of the smaller body, and R_* is the radius of the host star. Another

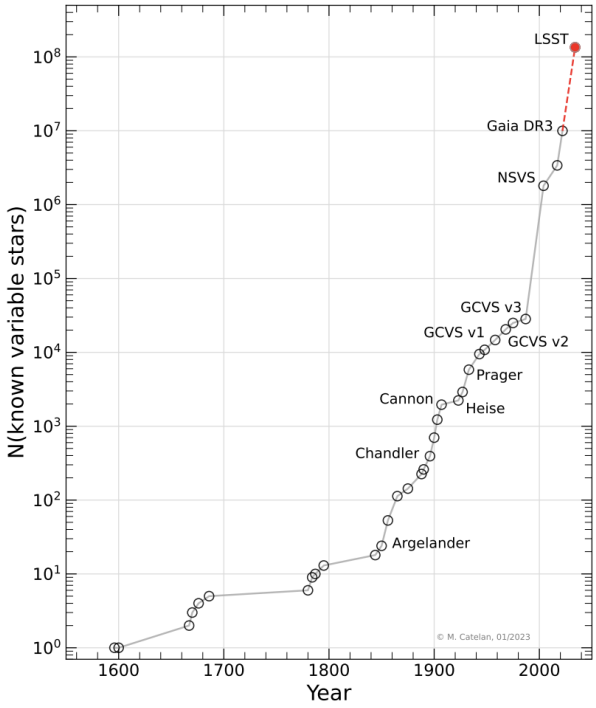


Figure 1.1: Number of known variable stars over time, including the projected estimate of variable stars in the era of the Legacy Survey of Space and Time (LSST Science Collaboration et al., 2009). Figure from Catelan (2023).

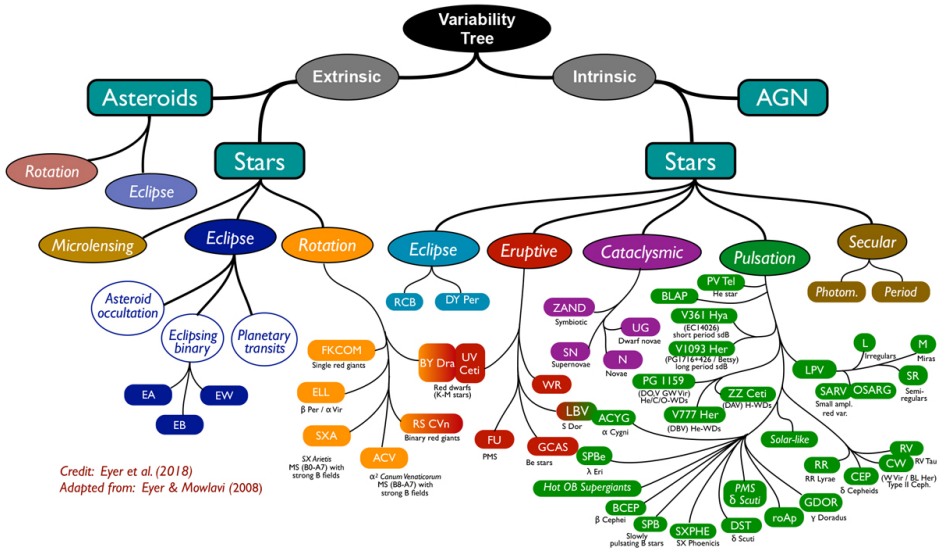


Figure 1.2: Variability classification tree by Gaia Collaboration et al. (2019b).

useful quantity is measuring the averaged sky probability of a transit/occultation, where α is the semimajor axis, and e is defined as the orbital eccentricity ($e = 0$), the transit (or occultation) probability reduces to

$$P_{tra} = P_{occ} = \left(\frac{R_* \pm R_{obj}}{\alpha}\right)\left(\frac{1}{1-e^2}\right), \tag{1.2}$$

demonstrating that the probability scales inversely with the orbital separation. The above equation highlights that for any stellar eclipse to occur, the parameter space of size, separation, and orbital eccentricity plays a crucial role in observing eclipses. This can be further generalized, such that the photometric baseline (ΔT) – meaning the survey duration required to discover a system scales approximately with the semimajor-axis. *Large photometric baselines are thus deeply connected to rare variability – due to the large baseline, and more available data.* One of the many important orbital parameters of a transiting body is the semimajor axis. In the case of a gravitationally bound system, Kepler's third law of planetary motion is expressed as:

$$P^2 = \left(\frac{4\pi^2}{GM_*}\right)\alpha^3, \tag{1.3}$$

where T is the orbital period and M is the mass of the primary host star, assuming that the secondary mass is negligible (i.e., $M_* \gg M_{obj}$). The total transit time (T_{tot}) in the case of an edge-on transit is:

$$T_{tot} = \frac{P}{\pi} sin^{-1}\left(\frac{R_*}{\alpha}\right), \tag{1.4}$$

where P is the orbital period. In the limiting case of circular orbits, we can assume that the Keplerian circular velocity is defined as:

$$u = \sqrt{\frac{GM_*}{\alpha}}, \tag{1.5}$$

which, together, can relate to the bounded orbital period of the object. The repeated measurement of either a transit or an occultation can strongly constrain the period, and thus the semi-major axis of an eclipsing body – which represents one of the many important geometrical constraints.

Studies of transiting exoplanets heavily rely on repeating, periodic signals to constrain the semimajor axis, the transit period, combined with stellar properties, which feeds directly into Kepler's third law and can be used to infer the full orbital solution Winn (2010). *Is all hope lost, however, if we only observed the eclipse once?* A common theme throughout the presented thesis is that many of the discussed systems are *non-periodic* or *quasi-periodic*. The fundamental transit observables, such as duration, depth, ingress and egress timescales, and overall transit profile, remain fully accessible even in a single observed event (Gilbert, 2022; Kenworthy & Mamajek, 2015a; van Dam & Kenworthy, 2024a; Winn, 2010).

Transit duration carries information about the chord length traversed across the stellar disk, and combined with an estimate of the stellar radius and crossing velocity, can constrain impact parameter and the physical size of the occulting body Winn (2010). One proposed

way in the literature to measure the minimum velocity (v_{min}) of the transit is using the so-called knife-edge model (Silvia & Agol, 2008a), which assumes that an opaque obscuring body that is large enough can transit its host star, and is often related to its minimum transiting velocity:

$$v_{min} \approx \frac{D_*}{|m_{max}^{-1}|}, \tag{1.6}$$

where m_{max} is the steepest observed flux gradient as defined by Pramono et al. (2024a). By measuring the smallest possible velocity from the observed transit light curve, this translates to an upper limit of the maximum semimajor axis (α_{min}), which provides useful constraints on the geometry of the obscuring body.

Asymmetric profiles, such as the characteristic forward-scattering brightening and extended egress seen in many scenarios: disintegrating planets around main-sequence stars (e.g., Rappaport et al., 2012a) and white dwarfs (e.g., Vanderburg et al., 2015a), transiting dusty exocomets (e.g., Rappaport et al., 2018a), and other complex dusty-related transits (e.g., Boyajian et al., 2016a). The transit shape of the light curve becomes a direct diagnostic of the transiting object's morphology and the physical processes driving it. Generally ignoring any atmospheric effects, rigid and symmetric bodies will produce *symmetric* transit light curves. Figure 1.3 demonstrates a schematic sub-section of light curve morphologies that can be produced by a variety of objects, linked to a plethora of complex astrophysics that is beyond the scope of this dissertation. During an eclipse, the transit of one single rigid body (i), versus many (iii), can have vastly different light curve morphological properties as demonstrated in Figure 1.3. In certain cases, the transit of dusty material can exhibit wavelength (λ) dependence, which ultimately is related to grain properties and the observed wavelength regime (Draine, 2003). More broadly, the observed intensity (I_λ) is attenuated by some intervening dusty material by the following relationship:

$$\frac{I_\lambda}{I_{\lambda,0}} = e^{-\tau_\lambda}, \tag{1.7}$$

where τ is the optical depth, and $I_{\lambda,0}$ is the intensity from the absence of the intervening material. The ratio of intensities can also be expressed in magnitudes, which gives the following relationship:

$$m_\lambda - m_{\lambda,0} = A_\lambda = 1.086 \times \tau_\lambda, \tag{1.8}$$

where m_λ and m_λ represent the magnitudes of the observed source before and after the attenuation has been applied. If we assume that the intervening dust particles are spherical and have a constant cross-sectional area (σ_λ), the optical depth can be estimated:

$$\tau_\lambda = \sigma_\lambda \int_{s_{min}}^{s_{max}} n_d(s')ds' \tag{1.9}$$

where $n_d(s')$ is the number density of the dust grains. The amount of attenuation (reddening) of light will depend on the scattering cross-section (σ_λ), where under the assumption that the wavelength of light (λ) is on the order of the dust of the dust grains (i.e., in Mie scattering) then $\sigma_\lambda \propto \lambda^{-1}$ (i.e., extinction coefficient). In the limiting case where the grain sizes are much smaller than the incident light, $\frac{2\pi a}{\lambda} \ll 1$, then generally $\sigma_\lambda \propto \lambda^{-4}$, where

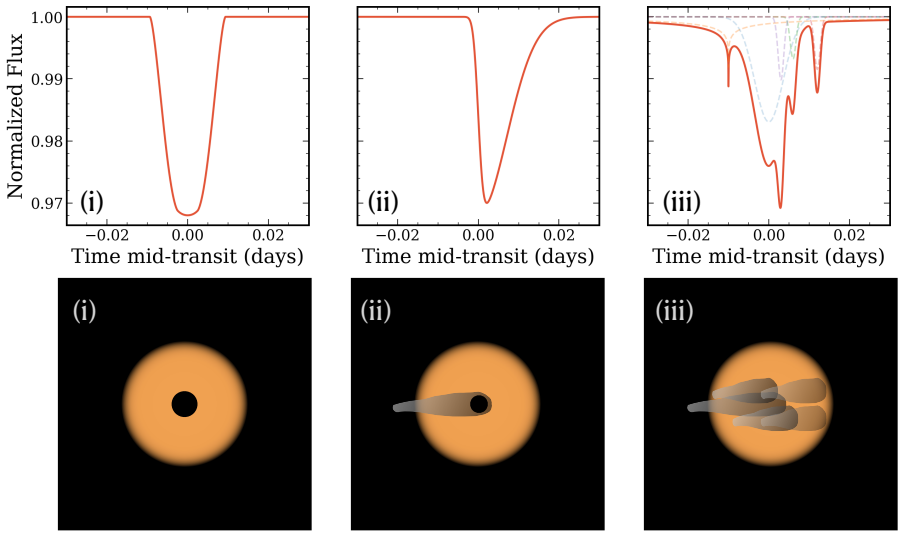


Figure 1.3: Schematic diagram of transit profiles assuming simple edge-on (b=0) stellar eclipses. **Top**: Transit light curves, reflecting those objects that are (i) uniform, (ii) asymmetric, and (iii) irregular. (**Bottom**) Schematic representing a simple transit geometry viewed edge-on for each associated light curve.

it has a much steeper wavelength dependence. Inferring dust grain size distributions from single photometric filter transit data is difficult, and robust constraints generally require simultaneous multi-wavelength observations (Boyajian et al., 2018; Schlawin et al., 2021).

4 Classes of Rare Transits

In my previous sections, I outlined the role of time-domain surveys in expanding our census of stellar variability and the classification tools and frameworks developed to make sense of the flood of data. Now I turn to the specific classes of extreme variability that are the focus of this dissertation. Circumstellar dust, often found in solid material orbiting a host star, is found across a wide range of stellar environments and evolutionary stages. Under favorable viewing geometric configurations, circumstellar dust can produce some of the most photometrically complex light curves eclipsing their host stars, which has remained an open question on their origins. As will be demonstrated in the sections to come, circumstellar dust leaves imprints on the resulting light curve in timescale, depth, color dependence, and recurrence of observed dimming events, each carry information about the underlying astrophysical process. Many systems that experience obscuration by circumstellar dust are direct probes of planetary system formation and evolution, and their discovery in increasing numbers is a direct consequence of the survey capabilities. For my thesis, I will focus on two general categories of dust-driven rare stellar variability: *circumstellar dust* across stellar age, which produces discrete and often aperiodic occultation events, and *circumstellar disks*, which drive variability across a broad range of timescales through their structure and evolution. Each is discussed in detail in the subsections that follow.

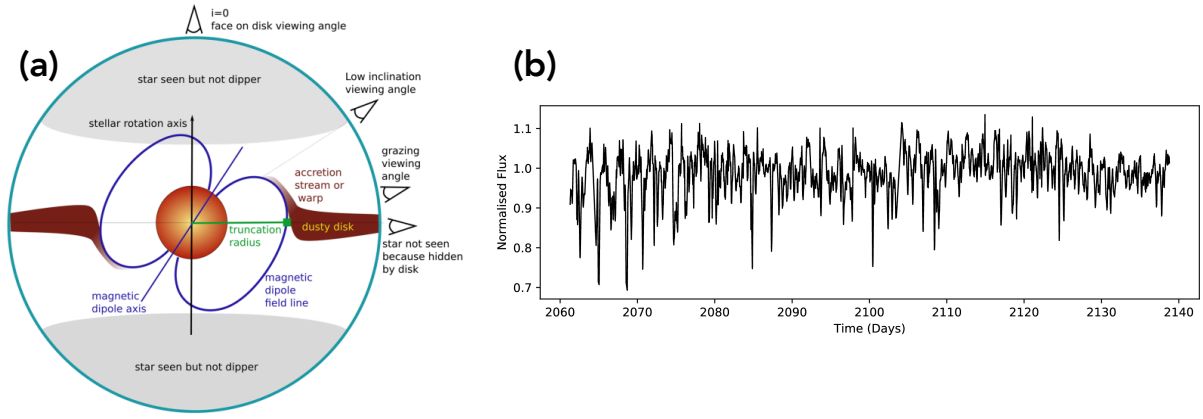


Figure 1.4: (**Left; a**) Represents a physical illustration of the dipper mechanism driven by accretion streams and warps from the magnetospheric accretion. (**Right; b**) Example light curve of a CTTS exhibiting a dipper light curve seen from the K2 mission. Figure (a) taken from Bodman et al. (2017), and (b) from Hedges et al. (2018).

4.1 Circumstellar Dust

Classical T Tauri stars (CTTS) are young low-mass stars that have long been recognized as irregular variable stars (Joy, 1945) associated with active accretion from the primordial circumstellar disks (Hartmann et al., 2016). CTTS are known to exhibit a broad range of variability patterns from accretion-driven outbursts, rotational modulation from star spots, to quasi-periodic occultations driven by dust. A particularly compelling and less understood subclass of CTTS is Young Stellar Object (YSO) *dippers* stars, which often exhibit deep (10–50%) flux drops on timescales of hours to days, often occurring quasi-periodically (Bodman et al., 2017; Stauffer et al., 2015), demonstrated in the right of Figure 1.4. YSO dipper events are widely interpreted as extinction by dusty structures located near the inner circumstellar disk edge, near the co-rotational radius, where magnetospheric accretion, where the gas ram pressure equals the outward magnetic field pressure, and truncation occurs (Hartmann et al., 2016). Large, homogeneous YSO dipper samples only recently became feasible with long, high-cadence and precision photometric baselines from space observatories. Particular examples include the K2 mission, which enabled 80-day monitoring of young associations at ∼30-minute cadence, allowing various dip morphologies and characteristic timescales to be measured at large YSO demographics (Hedges et al., 2018). Complementary campaigns with the *Convection, Rotation and Planetary Transits* satellite (CoRoT; Auvergne et al., 2009) and the Spitzer Infrared Array Camera (IRAC; Fazio et al., 2004) confirmed that, for many systems, the dimming is wavelength dependent, and persists into the infrared at reduced amplitude, supporting dust extinction rather than purely photospheric variability (Cody et al., 2014a).

The exact origins of the dusty obscuration around CTTS became clearer when many dipper events were found to recur on periods comparable to their host stellar rotation, implying that the occurring material is tied to a structure that correlates with mass-accretion (Bodman et al., 2017; Bouvier et al., 1999; Koenigl, 1991; Pouilly et al., 2021; Roggero et al., 2021). In more contemporary studies, optical CoRoT light curves in the NGC 2264 star-

forming region were found to exhibit periodic dips $3 < P < 13$ days that were consistent with dust near the Keplerian co-rotational period of the circumstellar disk (Stauffer et al., 2015). Intensive K2 observations of the Upper Sco and ρ OPH star-forming regions demonstrated a statistically significant relationship between the dipper amplitude depth and infrared excess, which was taken to be evidence that the dimming material is likely related to the inner disk material occulting the star (Ansdell et al., 2016). Within the paradigm of magnetospheric accretion, the stellar magnetic field truncates the disk where the magnetic pressure will balance the ram pressure from the inflowing gas, thus redirecting material along field lines into funnel flows and accretion shocks Bodman et al. (2017); Hartmann et al. (2016). In the magnetospheric accretion framework, misaligned magnetic dipoles naturally produce warped inner disks (Bouvier et al., 1999) or vertically extended structures that corotate with the star and periodically occult the stellar photosphere (see Bodman et al. (2017) and references therein), where the dust is far enough to not sublimate. An illustrative schematic is demonstrated on the left of Figure 1.4. Extensions of the dipper mechanism also include dusty accretion streams (Nagel et al., 2024), non-axisymmetric disk structures (Romanova et al., 2021), vortices caused by the Rossby Wave Instability (Meheut et al., 2010), and instabilities in mass-accretion regimes (Romanova et al., 2008), all of which can reproduce the diverse morphologies of quasi-periodic and aperiodic dips seen in canonical CTTS light curves.

One ongoing challenge in characterizing YSO dippers is reconciling the warp/occultation model with the disk geometry. The conceptual picture assumes that YSO dippers preferentially favor systems with nearly edge-on disks (i.e., inclination angles between 50- 70 degrees) such that vertical perturbations from dusty material near the inner rim can obscure the stellar photosphere (Bodman et al., 2017). A uniform analysis of 24 dipper stars resolved with ALMA found that the outer disk inclinations are consistent with an isotropic distribution from 0–75 degrees, with a decline only beyond 75 degrees (Hurt & MacGregor, 2023), implying that the outer ($\geq$10 AU) circumstellar disk probed at the sub-mm wavelengths is not straightforwardly responsible for the observed dipping phenomena. One hypothesis to reconcile with the observed sub-mm disk inclinations is that the dimming phenomena occur in the inner disk, as indicated by the co-rotational periods, thus proposing that the inner disk can be warped, or otherwise misaligned relative to the outer disk. Observational evidence for large inner–outer misalignment exists in at least a handful of systems, including a dipper transitional disk where ALMA CO kinematics reveal a misaligned inner gas disk inside a large cavity, and thus the dimming phenomena are driven by a shadowing effect (Mayama et al., 2018). Strong inner-outer misalignment has been hypothesized to be driven by external perturbations, such as planetary companions (Nealon et al., 2018) or stellar companions (Longarini et al., 2021), that cause large breaks in disks and produce precessing inner components shadowing signatures (Nealon et al., 2020). Most importantly, the main hypothesis of YSO dippers requires that dust survives at or near co-rotation, which imposes strong constraints on stellar mass, rotation period, and inner disk thermodynamics, suggesting that YSO dippers probe a fundamental stage in stellar and planetary evolution (Mannings et al., 2000).

YSO dipper-like stellar variability is expected to decline with stellar age, as the depletion of inner circumstellar material will reduce the likelihood of dusty occultation (e.g., Cody & Hillenbrand, 2018a). This evolution is driven by the declining mass-accretion rate as circum-

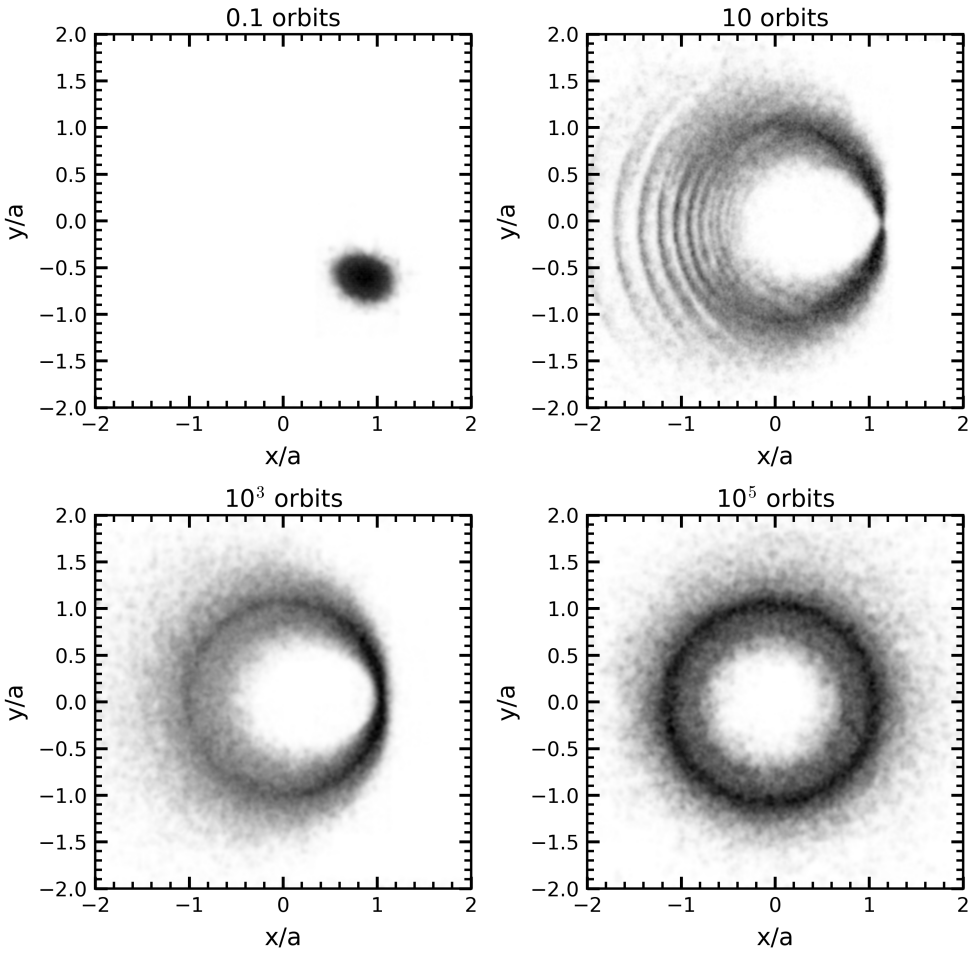


Figure 1.5: Numerical simulation snapshots of a giant impact collision shown at several key stages in the Cartesian X-Y plane. Figure adapted from Wyatt & Jackson (2016a).

stellar disks dissipate over time (Alexander & Armitage, 2006; Espaillat et al., 2008; Ingleby et al., 2014). During the transition phase from an actively accreting and warm circumstellar disk to a protoplanetary disk, stars undergo the final stages of planetary assembly (Hughes et al., 2018a). A widely accepted paradigm, and one particular and transient stage in planet formation, is the final step in planetary assembly through the catastrophic collision of planetary embryos (Canup, 2004). Another *rare* class of stellar variables is that of circumstellar disks with signatures of infrared excess – which have been broadly interpreted as the result of planetary collision afterglows. Giant impacts such as those that formed the Earth-Moon system are among the most dramatic and consequential events in planetary evolution, shaping the final architectures of planetary systems and setting the stage for habitability and life. Planetary collisions reshape planets in fundamental ways by changing their rotation periods, altering their atmospheres, and ultimately affecting their potential for life (Gabriel & Cambioni, 2023; Genda & Abe, 2005; Mrnjavac et al., 2023). Canonical planet formation theories predict that terrestrial planets reach their final assembly through collisions between Mars-sized protoplanets during the last ∼100 Myr of system evolution (Chambers, 2001; Wetherill, 1994). In most planet formation models, giant impact collisions are described as common during the terrestrial planet formation era, with collision-generated debris disks persisting for millions of years and producing detectable infrared excess signatures (Jackson & Wyatt, 2012a; Wyatt & Jackson, 2016b) in large disks, typically such as those presented in Figure 1.5. Despite the predicted importance of giant impacts to nearly every aspect of late-stage planet formation, many of the physical parameters that control their occurrence rates and observational signatures remain poorly constrained both theoretically and observationally by orders of magnitude. N-body simulations propose that catastrophic collisional debris from recent planetary collisions would be traceable as distinct stellar transit within a few orbits (Kenyon & Bromley, 2005). The presence of giant impact collisions has long been argued to sculpt many planets and moons in our solar system (Jackson & Wyatt, 2012a). Most relevant was the creation of the Earth-Moon system, which evidence argues for a giant collision, though an outstanding challenge remains to explain the isotopic similarity between the Earth and Moon (Asphaug, 2014). Other current cutting-edge theories, dubbed the *synestia* model, propose that a giant impact created a fast-rotating vaporized disk, called a synestia, which eventually cooled to create the current Earth and Moon and can explain the isotopic similarity between the Earth-Moon system (Lock & Stewart, 2019). However, throughout the literature, the exact frequency of giant impact events that the early Earth experienced remains uncertain. Numerical simulations of the evolution of Earth-like planets suggest that all-Earth analogs will experience at least one giant impact around solar analogs (Quintana et al., 2016a). While theoretical models predict Earth experienced only one giant impact during formation, isotopic evidence from helium-neon ratios in mantle-derived basalts indicates at least two giant impacts were required to explain the observed geochemical signatures, suggesting that multiple giant impacts may be a common feature of terrestrial planet formation (Tucker & Mukhopadhyay, 2014). The frequency of impact collisions is thus an important constraint for better understanding many intersecting parameters in the history of any given terrestrial planet. While traditional IR surveys have dominated giant impact searches through searches of excess in the IR (e.g., Fujiwara et al., 2013), time-domain photometric monitoring offers a new complementary and perhaps an even more sensitive pathway for discovering ongoing planetary collisions through the stellar occultations by evolving col-

lisional debris. Time-domain monitoring is now surfacing plausible giant impact aftermaths among young stars. Spitzer (Werner et al., 2004) observational campaigns revealed weeks-to-years variability in extreme debris disks with short-term modulations and long-term fades consistent with clumps and collisional evolution of impact-produced debris (Kenworthy et al., 2023a; Su et al., 2019; Su et al., 2022a), while the presence of warm circumstellar dust around Sun-like stars has been also revealed (Melis et al., 2021). The discovery of ongoing giant impact systems provides a unique opportunity to study the outcomes of dust produced by giant impact collisions; however, their rarity and physical constraints, such as dust location, temperature, mass, and composition, remain poorly understood on the population level. One unique advantage of time-domain studies of transiting dust from giant impact collisions is that they can provide independent measurements of the dust semimajor axis by searching for periodic modulations in the stellar light curve, which have important consequences for the dynamics of the collisions.

Not all dust-driven dippers can be explained by young stars with disks or collisional debris connected to planet formation. A rare class of dipper-like variability emerges among older, more mature, main-sequence stars, where accretion-disk and other catastrophic planetary collision interpretations are firmly ruled out. The archetype of this class is KIC 8462852, which exhibits deep, aperiodic dimming events of up to ∼20% on timescales of days with no clear periodicity and, most importantly, no detectable infrared excess (Boyajian et al., 2016b). KIC 8462852 is understood to be an otherwise normal F3-V middle-aged (>100 Myr) main-sequence star, ruling out accretion-driven or disk-mediated variability and instead requiring a transient obscuring medium (Boyajian et al., 2016b). Subsequent multi-band monitoring (Boyajian et al., 2018; Davenport et al., 2018) demonstrated that the dips are chromatic and consistent with optically thin extinction by sub-micron grains, reinforcing the interpretation that the obscuration arises from transient dust clouds rather than opaque bodies. Millimeter and sub-mm non-detections have placed upper limits on the total available dust mass around KIC 8462852 to be $< 7.7 M_{\oplus}$ within 200 AU, with the dust-mass equivalent of 30 Comet 1/P Halley-type objects (Thompson et al., 2016). Interestingly, KIC 8462852 exhibits both short-term variability and long-term secular dimming ranging from ∼1% over the Kepler baseline to ∼0.1-0.2 mag per century (Montet & Simon, 2016; Schaefer, 2018), whose astrophysical origins are still heavily debated (Wright & Sigurdsson, 2016). Collectively, observations of KIC 8462852 have motivated scenarios involving dynamically produced dust, such as star-grazing exocomets or the catastrophic disruption of a planetesimal or planetary body, or the recent collision of two planetary bodies (see Wright (2018) and references therein). KIC 8462852 poses a key challenge that the dust must be produced in sufficient quantities to yield deep photometric dips, while remaining short-lived and geometrically sparse to avoid being detectable in the infrared. Analogues to KIC 8462852 are rare and not driven by a stable inner disk structure, but rather by stochastic processes capable of delivering copious amounts of generated dust with unknown origin (Wright, 2018).

4.2 Disk Eclipses Around Stars

Circumstellar and circumplanetary disks are natural byproducts of stellar and planetary formation (Andrews, 2020; Armitage, 2011; Williams & Cieza, 2011). Under favorable viewing

geometries, *circumsecondary* disks[1] can obscure their host star along the line of sight, producing unique, rare dimming events that can last from days to years. To date, only a handful of such systems have been confirmed (Stencel, 2016). Despite their rarity, disk-eclipse systems offer a remarkable and rare window into a wide range of astrophysical processes that govern stellar and planetary evolution. The structure and geometry of transits encode the radial and azimuthal density structure of the disk, providing a probe of disk composition, opacity, and substructure that otherwise is only accessible for nearby systems. Beyond the physical constraints of circumsecondary disks, the stars or planets that host these disks place important constraints on binary evolution, circumplanetary disk lifetimes, and possibly the early stages of moon and planet formation (Kenworthy & Mamajek, 2015a; Kloppenborg et al., 2010). To date, the known sample of disk-bearing eclipsing systems spans a wide range of stellar ages, with the earliest examples found around young pre-main-sequence stars.

Although the frequency of disk-eclipse systems spans a wide range of stellar evolution, their occurrence is expected to be strongly biased toward young stellar populations, where disks are both more prevalent (Mamajek, 2009) and dynamically structured (Andrews et al., 2018). In such young stellar environments, the high frequency of binary companions as high as $> 80\%$ (Duchêne & Kraus, 2013; Ghez et al., 1993; Kraus & Hillenbrand, 2008) and circumsecondary disks significantly increases the probability of observing disk-driven occultation. Mamajek et al. (2012) estimated that a survey of $\sim 10^4$ young ($\sim$10 Myr) post-accretion pre-main-sequence (PMS) stars should yield a handful of deep eclipses caused by circumplanetary disks and disks surrounding low-mass companion stars, owing to the high frequency of binary systems in young clusters, many of which are hypothesized to likely host circumplanetary disks. Mamajek et al. (2012) presented one such candidate, 1SWASP J140747.93-394542.6=ASAS J140748-3945.7 (hereafter J1407), a nearby young ($\sim$16 Myr) weak-lined CTTS that underwent a series of complex eclipses lasting $\sim$2 months, believed to be driven by an unseen secondary companion, J1407b, with a giant ring system and gaps on an unconfirmed orbital period (Kenworthy & Mamajek, 2015b; Kenworthy et al., 2015). To date, follow-up studies have attempted to search for the companion either by archival eclipses or through sub-mm emission searched with ALMA, though none have been able to reliably identify J1407b (Kenworthy et al., 2020; Klaassen et al., 2025; Mentel et al., 2018). In contrast to J1470b, PDS 110 (HD 290380), is an $\sim$10 Myr star with a large IR excess in the Orion OB1a association (Brown et al., 1994) was identified with the SuperWASP and KELT surveys. PDS 110, which was found to be eclipsed by a low-mass 1.8-70 M_{Jup} companion, PDS 110b, on an 808-day orbital period equivalent to a 2AU orbit, with a circumsecondary disk of diameter $\sim$0.3 AU around a low-mass planet or brown dwarf (Osborn et al., 2017). More recently, ASASSN-21js has been another disk-bearing young star analog with a prolonged optical dip at large semimajor axis of 13,000 AU orbit, placing it at the Oort cloud equivalent of the host star (Pramono et al., 2024b).

In contrast, deep-eclipse systems are not exclusive to young stars; some of the longest studied and most perplexing examples involved primaries with Epsilon Aurigae standing as the standard paradigm. Epsilon Aurigae (ϵ-Aur) has been extensively studied due to its perplexing long-timescale photometric properties that in the last century challenged ideas of

[1]Circumsecondary is purposefully used to be agnostic of the host type, such as a stellar or sub-stellar companion.

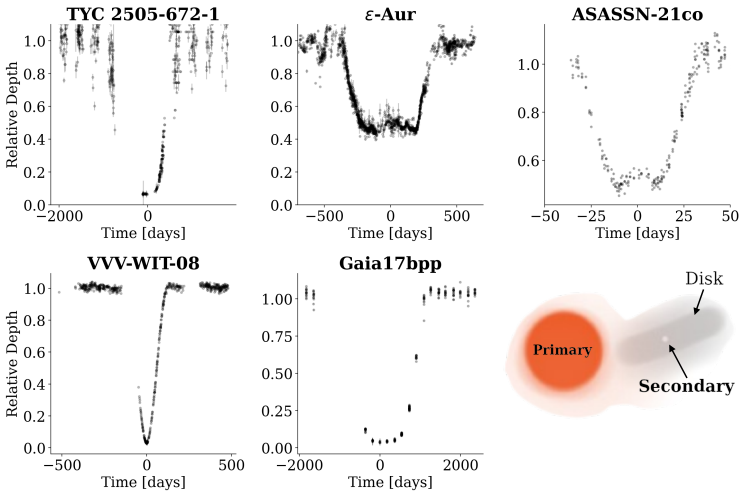


Figure 1.6: Normalized optical light curves of known giant stars eclipsed by disks. The bottom right schematic represents a cartoon illustration of the system geometry.

stellar evolution. The earliest reported document of the variability of ϵ-Aur was reported by Fritsch in 1824 (Wood, 1985a), who discussed the photometric measurements of the minimum in 1821 (Wood, 1985b). Ludendorff (1903) provided a full context of the photometric minima between 1847 and 1875 and was among the first to propose that this star was an Algol-type light curve. There was an issue with the "eclipse theory" that was because the spectroscopic data remained consistent during the totality of the light curve (Wood, 1985a), among other reports of concern between the inconsistencies between the photometric properties (i.e., the light curve) versus spectroscopic observations. Ultimately, what made this system puzzling was the large period and long duration of the "dimming phase", and it was unclear, looking back at the literature, if the community was fully convinced it was another star going around ϵ-Aur. Around the 1960's, models of what could be causing the eclipse began to surface, but Huang (1964) was the first to suggest the theory of a co-rotating opaque gaseous disk.

Today, ϵ-Aur is known to exhibit its single 2-year-long flat-bottomed dimming event, which has long challenged the understanding of binary star formation (Carroll et al., 1991). Recent studies have characterized ϵ-Aur as an F0-Ia supergiant star surrounded by a young low-mass B5V-type star companion with an extended cool optically thick disk that periodically eclipses the primary star every 27 years (Kloppenborg et al. (2012) and references therein). Despite significant advancements in verifying the presence of the occulting disk around ϵ-Aur, questions regarding the origins and lifetime of the disk, occurrence rates, and formation channels of such systems remain largely unexplored (Kloppenborg et al., 2010). Despite the two centuries passing since its discovery, only a handful of analogue systems with more extreme parameters, including event duration, dimming depth, and orbital period (Rodriguez et al., 2016; Smith et al., 2021), have been found, as demonstrated in the optical light curves in Figure 1.6. For example, Rodriguez et al. (2016) found a hot (∼8000 K) companion around the primary M Giant (∼3400 K), TYC 2505-672-1, proposed to be a possible pre-He WD/ low-mass B-type subdwarf (sdB). However, issues with such an interpretation challenge the current orbital period distribution of most pre-He WD that are found typically within orbital periods of < 2.1 days (Maxted et al., 2014). If it is true that the companion is a hot sdB,

then such a valuable system might be pointing to the product of white-dwarf mergers since current theory suggests that sdB formation channels only occur under binary interaction (Clausen et al., 2012; Han et al., 2002). Such rare binary stars developed by large opaque disks remain poorly understood and have important constraints on binary star evolution.

5 Structure and Outline

In the previous section, I have given a broad overview of the diversity of rare stellar eclipses driven by circumstellar dust. The core theme of my thesis is the agglomeration of rare stellar variables driven by circumstellar material, many of which pose ongoing challenges. As a whole, this thesis demonstrates that both archival and real-time surveys can enable the discovery of such unique systems and can be conducted systematically, given the breadth of photometric coverage conducted across many surveys. In more detail, my dissertation is organized accordingly:

- **Chapter 2: Main-Sequence Dipper Stars** – First, we will undertake the first-ever systematic study of searching for "main-sequence dipper stars" which are analogues to the KIC 8462852 system. In this work, we present the discovery of 81 new dipper systems that are potential analogues to KIC 8462852 and the J1407 systems, conducted through a large 64 million FGK star catalog search enabled by ZTF and Gaia. In this work, I demonstrate: (i) novel algorithmic and computational methods and tools for finding these dippers, (ii) conduct a comprehensive search for KIC 8462852 analogs, (iii) compile optical and near-IR data from data archives, and (iv) suggest tentative classifications based on the observed properties.

- **Chapter 3: Occultation by Disks Across Stellar Age** – Next, we present the discovery of Gaia17bpp, identified as an evolved RGB star that underwent a large (>4.5 mag) and long (∼7 year) occultation, unlike anything that has been reported before in the literature of disk-bearing eclipses. In more detail, we characterize the properties of the system and provide clues on its potential origin, ranking it as one of the largest stellar occultations to have been discovered in digital data archives.

- **Chapter 4: Transient Hot Dust Probing Planet Evolution** – Next, we are challenged by the discovery of Gaia20ehk that looked like a bizarre dipper star we had considered in the previous chapters. I will discuss the inverse optical/mid-IR light curve properties of Gaia20ehk and our interpretation of this unique system. We suspect that we have discovered *Gaia's* first planet impact collision, one of only a handful of known systems. We thus call *Gaia's* Giant Impact Candidate (GIC). I will end this chapter with a brief discussion on the potential rates of such objects and how to find more in the future.

- **Chapter 5: Future Directions & Conclusions** – The future ahead is exciting in this realm, as we are making strides in continuous photometric surveys at remarkable timescales and depths. In this final chapter, I will discuss the future directions that include some of the most exciting surveys turning on in the coming years that will help

answer many of the questions posed in this thesis. I will conclude with the primary takeaways of my thesis.

CHAPTER 2

MAIN SEQUENCE DIPPER STARS

1 Preface 19
2 Introduction 19
3 Photometric Data 22
4 Methods 22
5 Properties 31
6 Discussion 47
7 Conclusion 55
8 Appendix 58

1 Preface

This work presented in this chapter has been accepted for publication in *The Astrophysical Journal*. I gratefully acknowledge all my collaborators, with a particular emphasis on my colleagues with the LINCC Frameworks collaboration, who made the tools and development scalable algorithms and techniques used in this work possible via the Large Survey Database (`lsdb`). The publication

2 Introduction

The era of synoptic time-domain surveys has revolutionized the taxonomy of variable stars. Among these variables is an emerging new class of main-sequence stars, dubbed as "main-sequence dippers" that can exhibit non-periodic variations in their luminosity and whose origin is still largely debated in the community. The most well-known system is KIC 8462852 (hereafter "Boyajian's star") (Boyajian et al., 2016c), a seemingly ordinary F3V dwarf star that underwent irregular photometric deep dimming events, including a long-term secular dimming (Montet & Simon, 2016) during the primary Kepler survey (Borucki et al., 2010). The four main observed features to be interpreted of the Boyajian star system are the aperiodic dimming events during the Kepler mission, the transit shape of the dimming events, a secular dimming on the timescale of years to centuries (Montet & Simon, 2016; Schaefer, 2016), and the lack of infrared excess indicating the presence of warm dust (Marengo et al., 2015). Kiefer et al. (2017) showed that two dimming events in the Boyajian star system showed similarities, occurring 928.25 days apart, suggesting a potential repeated transit of a large ring system or a string of exocomets. Despite extensive follow-up studies, pinpointing any periodicity in the dimming events remains unconfirmed (Boyajian et al., 2018), but follow-up multiband photometry shows the dimming events show the reddening of non-grey extinction of sub-micron dust. The interpretation of the observable dimming events and lack of infrared excess continues to spark debate in the literature, with possible explanations including transiting exocomets (Boyajian et al., 2016c), comet swarms (Bodman & Quillen, 2016; Makarov & Goldin, 2016), large ringed planets with Trojan asteroid swarms (Ballesteros et al., 2018), the consumption of a planet (Metzger et al., 2017), the tidal disruption of orphan exomoons (Martinez et al., 2019), or the presence of a potential technosignature of a transiting megastructure (Wright et al., 2016). A comprehensive review of these competing theories, including an analysis of their advantages and disadvantages, is provided by Wright & Sigurdsson (2016) and references therein.

More recently, ASASSN-21qj (Rizzo Smith et al., 2021), a G dwarf, underwent a dramatic dimming event that was later attributed to either the collision of two planetesimals producing a debris field (Kenworthy et al., 2023a) or the breakup of exocometary bodies (Marshall et al., 2023a). Unlike the Boyajian star, ASASSN-21qj exhibited an optical dimming event while the infrared data from the *Wide-field Infrared Survey Explorer* (WISE; Wright et al. (2010a, 2019)) showed a brightening that lagged behind the optical dimming. The infrared excess observed was constrained to originate between 2 and 16 AU from the star, suggesting that the debris was warm enough (∼1000 Kelvin) to emit significant infrared radiation that is hypothesized to be involved in the collision of two Earth-size planets (Kenworthy et al.,

2023a). Findings from Marshall et al. (2023a) suggest the occulting material consists of submicron-sized dust grains at much smaller semimajor axes of ∼0.2 AU, with a minimum total circumstellar dust mass of 10^{-6}M, alluding to a different origin and timescale for the dust production. No additional large amplitude dimming events have been reported from this system to date. Although both ASASSN-21qj and the Boyajian star exhibit aperiodic and complex dimming events, ASASSN-21qj shows an infrared excess from warm dust, indicating more recent and possibly close-in material. In contrast, no infrared excess has been detected around the Boyajian star, suggesting that the dust production mechanisms differ in timescale, mass, orbital geometry, and other parameters.

Another class of poorly understood variable stars exhibiting similar dimming behavior involves rare occultations by large and or opaque disks, typically associated with both young and evolved stars. Mamajek et al. (2012) suggests that a survey of young (∼10 Myr) post-accretion pre-main sequence (PMS) stars should yield a handful of deep eclipses caused by circumplanetary disks and disks surrounding low-mass companion stars, due to the high frequency of binary systems in young clusters, many of which can likely host circumplanetary or circumsecondary disks (e.g., Prato & Weinberger (2007)). Mamajek et al. (2012) presented one such candidate, 1SWASP J140747.93-394542.6 (hereafter J1407) which was a nearby young (∼16Myr) weak-lined T Tauri star that underwent a series of complex eclipses that lasted for two months and is believed to be caused by an unseen secondary companion, J1407b, with a giant ring system with gaps with an unconfirmed orbital period (Kenworthy & Mamajek, 2015b; Kenworthy et al., 2015). In contrast, PDS 110 a ∼10 Myr star with large infrared excess in the Ori OB1a association was found to be eclipsed by a low-mass (<70 M_{Jup}) companion, PDS 110b, on an ∼ 800-day orbital period, with a circum-secondary disk around a low-mass planet or brown dwarf of diameter ∼0.3 AU (Osborn et al., 2017). The shared characteristics of J1407b and PDS 110b are both located in regions of ongoing star formation, suggesting stellar youth. In more extreme cases involving more evolved primary stars, systems such as ϵ Aurigae and other analog systems (Forés-Toribio et al., 2025; Kloppenborg et al., 2010; Pramono et al., 2024b; Rodriguez et al., 2016; Saito et al., 2019; Tzanidakis et al., 2023; Zakamska et al., 2025a) are believed to result from occultations by large opaque disks on extremely long orbital periods. The dipper phenomenon is more common among Young Stellar Objects (YSO) that have been found to exhibit periodic, quasiperiodic, or aperiodic dimming events from timescales of hours to years (Cody et al., 2014b; Fischer et al., 2023), attributed to line-of-sight effects of magnetospheric accretion disk columns and dust around PMS stars (Bodman et al., 2017). Large-scale monitoring campaigns, such as the CSI-2265 project, have shown that over 20% of disk-bearing stars exhibit discrete fading events proposed to be circumstellar obscurations or changes in the inner disk. Similar detection rates of YSO dipper stars have been reported among young stellar associations in high-precision photometric missions, Kepler/K2 and the Transiting Exoplanet Survey Satellite (Ricker et al., 2015), (Capistrant et al., 2022; Hedges et al., 2018).

Resolving the main-sequence dipper phenomenon requires careful systematic investigations into analog systems and shared properties. Previous limited sample studies have been deficient in key aspects such as samples of main-sequence stars, thorough completeness measures in search techniques, and a comprehensive understanding of systematic effects and contamination. LaCourse (2016) reported an absence of Boyajian star analogs among 315,000

stars in the Kepler/K2 fields, despite the large presence of known systematics that must be carefully removed (Angus et al., 2016). The largest search to date was done by Schmidt (2019) who conducted a blind search for Boyajian star analogs using the Northern Sky Variable Survey (NSVS; Woźniak et al. (2004)) and the All Sky Automated Survey for Supernovae (ASAS-SN; Kochanek et al. (2017b)), looking through 2.3 million stars. From 200 initial candidates, they identified 21 dipper stars across the main-sequence and red giant branch, with varying dimming timescales classified as "rapid" and "slow". The largest challenge in interpreting the Schmidt (2019) results lies in determining whether these identified main-sequence dippers are true analogs to the Boyajian star. Several critical factors remain unaddressed, including: searches for infrared excess measurements that would indicate warm circumstellar material, detailed characterization of dip durations and amplitudes comparable to Boyajian's star, rigorous vetting of photometric data for systematic effects, and analysis of any underlying periodic signals that might distinguish these events from the complex aperiodic dimming characteristic of Boyajian's star. Without comprehensive assessments, the classification of the candidates reported as true Boyajian's star analogs remains uncertain. Other variables such as R Coronae Borealis Stars (Karambelkar et al., 2021), massive stars with mass-loss events (Montargès et al., 2021), and planetary debris around white dwarfs (e.g., Vanderbosch et al. (2021)), can also exhibit stochastic dimming events. Thus, careful attention is needed to systematically select regions in the color-magnitude diagram to conduct careful searches and understand the underlying selected stellar population. While uncertainties remain about NSVS sample completeness, contamination, and other possible camera systematic artifacts, their work demonstrated that such dimming phenomena are rare, with a similar occurrence rate of $\sim$1 in a million (Schmidt, 2019) for main-sequence solar-like stars. As investigated on a case-by-case basis, searching the origins of such dimming phenomena around main-sequence stars is still a big challenge, and requires extensive multi-wavelength observational campaigns to place meaningful interpretations on what drives their variability. The increasing discovery rate of stochastic dimming events seen among main-sequence stars calls to action for a systematic search to possibly shed more insight into the underlying mechanisms.

In this study, we present a systematic search for main-sequence dipper stars using multiwavelength photometric surveys. Our analysis is based on a carefully selected sample of high-cadence light curves from the Zwicky Transient Facility, combined with infrared archival data to characterize the long-term variability of these systems. We investigate the underlying physical mechanisms driving the observed dimming events and assess their potential classifications. This paper is organized as follows. In Section 3, we describe the data acquisition process, including the selection criteria and crossmatching with auxiliary surveys. Section 4 outlines our dipper search pipeline, detailing the methods used for event identification, classification, and the mitigation of systematics. Next, in Section 5, we analyze the properties of our identified dipper candidates, such as timescales, depths, color properties, and other auxiliary infrared/Hα data. Section 5 provides a discussion of the potential classification scenarios, including eclipsing binaries, young stellar objects, cataclysmic variables, and occultations by circumstellar material, including disks. Finally, in Section 6, we summarize our findings and discuss future directions of our study.

3 Photometric Data

3.1 ZTF Ubercalibrated

The Zwicky Transient Facility (ZTF) is a wide-field time-domain survey utilizing the 48-inch Schmidt telescope at Palomar Observatory. It covers the northern sky in g, r, and i bands with a 47 square-degree field of view, achieving median 5σ limiting magnitudes of g$\sim$20.8, r$\sim$20.6, and i$\sim$19.9 mag in 30-second exposures (Bellm et al., 2019b; Dekany et al., 2020; Graham et al., 2019a; Masci et al., 2019). For our dipper detection pipeline, we use the ZTF Ubercalibration (Zubercal) DR16 photometry that spans observations from March 2018 to March 2023. Zubercal is a new set of photometry based on a detailed recalibration of the ZTF PSF photometry that achieves 1% or better photometric accuracy. The current ZTF PSF calibration is based on the comparison of each quadrant image with a set of calibration stars selected from Pan-STARRS1 (PS1; **?**). However, certain limitations arise, such as the crowding, available PS1 calibration stars, and Galactic reddening at the line of sight, which will overall reduce the accuracy of the estimated zero points and thus the photometric accuracy. The Zubercal pipeline also corrects for varying spatial, chromatic, and temporal structures in the photometry that are inherent due to the CCD inhomogeneities (Drake, 2023). Zubercal works to our advantage for performing such large photometric searches since it achieves significantly higher accuracy photometry compared to the reported nominal ZTF PSF photometry (Drake, 2023). In addition, Zubercal comes with more photometry from the ZTF CCD edges since it does not require a ZTF reference frame and compensates for areas with little to no reference frames. Due to the high accuracy, removal of temporal systematics, and additional detections, Zubercal is a well-suited data product to help us achieve a systematic search for dipper main-sequence stars. All dipper candidates investigated in this work are compared against the standardized NASA/IPAC Infrared Science Archive[1] ZTF photometry and ZTF science images (IRSA, 2022) to ensure that no other unwanted systematics are present.

4 Methods

4.1 Gaia FGK Dwarf Selection

The selection of FGK dwarfs represents optimal targets for detecting main-sequence dipping events due to their relatively stable photometric behavior compared to more active variable stellar populations. Using early Kepler data, Ciardi et al. (2011) demonstrated that G dwarfs exhibit the lower photometric scatter, with a dispersion floor near 0.04 mmag, while F and K dwarfs show somewhat higher variability, typically a few mmag on the timescale of weeks due to rotational modulation, magnetic activity, and stellar pulsation. On longer timescales of years, studies of magnetic activity cycles of FGK dwarfs have found typical variability amplitudes of 10-30 mmag with an average timescale of 6-8 years (Suárez Mascareño et al., 2016).

[1] https://irsa.ipac.caltech.edu

In this work, we utilize `StarHorse 2022` (Anders et al., 2022), a Bayesian isochrone-fitting framework developed to derive robust stellar astrophysical parameters, including distances and extinction values. Using a Bayesian statistical framework, `StarHorse 2022` combines observational data with prior information about Galactic metallicity, geometry, and interstellar extinction. `StarHorse 2022` delivers a catalog of 362 million stars from Gaia EDR3 (Gaia Collaboration et al., 2021a), cross-matched with photometric surveys like PS1, SkyMapper (Onken et al., 2019), Two Micron All Sky Survey (2MASS; Skrutskie et al. (2006)), and WISE. The derived stellar parameters of `StarHorse 2022` are validated through comparisons with other similar works such as Bailer-Jones et al. (2021a), Andrae et al. (2018), Queiroz et al. (2020), as well as through open cluster data, astroseismic measurements, and spectroscopic observations. Findings suggest systematic errors are smaller than the nominal uncertainties for the majority of objects, making it a well-suited catalog to select most of our FGK main-sequence stars.

First, we selected all `StarHorse 2022` sources with declination above -30 degrees to match the footprint of the ZTF survey. Next, we select `StarHorse 2022` sources with $\log(g)$ between 4 and 5, and $T_{\rm eff}$ between 4000 Kelvin and 7220 Kelvin (Pecaut & Mamajek, 2013). In addition, we impose an astrometric criterion to be `fidelity` >0.9 from `StarHorse 2022` to ensure that our sample excludes sources with unreliable astrometric solutions (see Figure 15 Rybizki et al. (2022)). We apply this cut to significantly reduce the contamination from objects whose positions in the color-magnitude diagram are compromised due to poor Gaia astrometric measurements and thus increase the reliability of our FGK stellar selection. The query yielded ∼106 million stars. Next, we crossmatched these stars to the Pan-STARRS1 survey, assuming a 1-arcsecond nearest neighbor crossmatch that resulted in ∼70 million stars. To further ensure we have selected a strict sample of stars on the stellar locus, we have selected sources that only fell within 2σ of the PS1 color-color stellar locus in the $(g-r)$ and $(r-i)$, as any outliers in the PS1 stellar locus were likely due to unwanted systematics. Our selected stellar locus was visually compared to the stellar locus of Covey et al. (2007), and found strong agreement, although we raise the possibility of a few contaminating M-dwarfs at the redder (g-r)∼1.2 colors (Davenport et al., 2014). In , we present our stellar locus selection compared to the work of Covey et al. (2007). The final resulting catalog contains 63 million candidate FGK main-sequence stars that are to be used for this analysis. In Figure 2.1, we present the color-magnitude diagram of our final selected sample of FGK main-sequence stars.

4.2 Finding Dips

Here we describe how we conduct our systematic search for main-sequence dipper stars. First, we match our selected FGK dwarfs object catalog (see Section 4.1) to the Zubercal photometric catalog to access the photometry for each source. We reject all sources with fewer than 50 detections in each ZTF *gr* photometric filter. Crossmatching is conducted using the Large Survey Database[2] (`LSDB`) (Caplar et al., 2025) framework that enables rapid crossmatch on large astronomical catalogs leveraging Hierarchical Adaptive Tiling Scheme

[2] lsdb.io

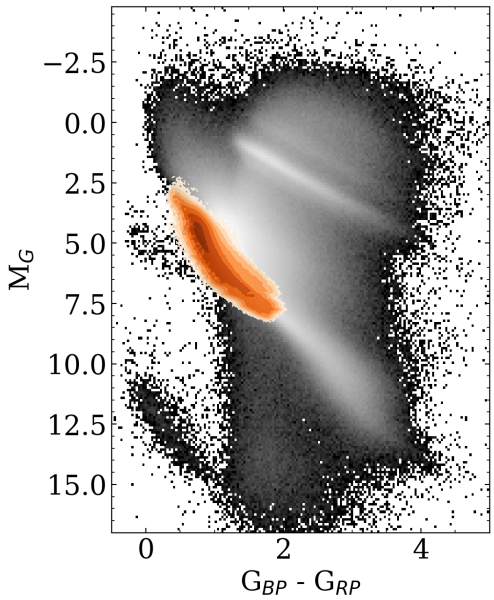


Figure 2.1: Gaia DR3 color-magnitude diagram (in gray) for the nearby Gaia DR3 sample (Gaia Collaboration et al., 2022a) shaded by the number of stars per bin. Overplotted in the orange contours is the color-magnitude diagram selection of the FGK main-sequence stars using `StarHorse 2022` (Anders et al., 2022) used for this study.

(HATS) data format for survey structure[3]. To scale our computations of all Zubercal light curves, we utilize the `Nested Pandas`[4] package for large-scale time-series computations. We used `Dask`[5] to implement a CPU-bound parallelization of the computing tasks using 25 cores.

For each star, we compute the biweight magnitude deviation of their ZTF *gr* light curves defined as:

$$\delta_i = \frac{m_i - R}{\sqrt{\sigma_{m_i}^2 + S^2}}, \tag{2.1}$$

where R and S are the robust biweight location and standard deviation of each light curve, respectively, using the `astropy` implementation. Since we are looking for large amplitude deviations in our time series data, the selection of the biweight is intentional, as it is more robust against outliers than traditional measures such as the mean and standard deviation, which can be strongly influenced by outliers.

Next, using the magnitude deviation of the ZTF r-band light curves, we search for peaks above a threshold $\delta > 3$ using the SciPy `find_peaks` utility, which finds local minima by comparing neighboring values of a given array (Virtanen et al., 2020). To avoid the detection of redundant peaks in our running deviation metric, we enforce a minimum separation of 50 ZTF detections, which corresponds to a time interval of approximately 100-150 days, assuming a typical ZTF cadence of 2-3 days. This criterion is designed to reduce false positives from unnecessary detections of structured dips with multiple minima within the ∼150 day interval. In a few cases, our criterion may result in sources being flagged to contain

[3]hats.readthedocs.io
[4]https://nested-pandas.readthedocs.io/
[5]https://docs.dask.org/

simply one dip as compared to more; however, it should not affect the identification of at least one dip. The peak-finding algorithm returns the times at each identified peak. To eliminate spurious dips from systematic effects, we enforce that a corresponding dip must also be present in the g-band data within two days of the r-band magnitude deviation peak. To identify significant dips, we compare the deviation at the median time of the r-band dip with the corresponding g-band detections within the defined dipper window, and calculate the z-score statistic between the two deviation estimates measured for the g and r light curves. A dip is considered significant if the z-score exceeds 1σ. While we acknowledge that this threshold is relatively low, through trial and error, we found that it best minimizes bias against events with moderate color dependence. Finally, each identified peak in the ZTF-r band is fitted using a Gaussian function with mean (μ) and standard deviation (σ).

4.3 Dipper Scoring Metric

Various dipper score metrics have been carried out throughout the literature to identify dips in time-series data. For example, Cody et al. (2014b) introduced the flux asymmetry score that measures the asymmetry in flux fractions of a given light curve. Asymmetry flux-related metrics have been used successfully to identify YSO variability, some of which have stochastic variability, such as the signal this study wishes to address. Other more sophisticated machine learning techniques have been utilized before to find anomalous ZTF light curves using a series of machine learning outlier techniques (Malanchev et al., 2021) that have been successful in the past in identifying anomalous light curves. Such workflows have previously benefited from the computationally cheap time-series metrics capable of identifying interesting light curves. We found that previous methods do not take into account the frequency of dips, duration, and the number of available data points at the signal of interest. Such parameters are key in deriving a robust metric that will allow the identification of good candidate main-sequence dipper stars in sparse and noisy light curves such as ZTF. In this work, our aimed scope is not necessarily to discover "anomalous" light curves but instead to build a metric that quantifies the number of dips that occur in each light curve as a function of amplitude, duration, and available data (i.e., data quality) over the full light curve history. We introduce a novel light curve dipper score metric as:

$$\mathcal{S} = \frac{1}{ln(N+1)^N} \sum_{n=i}^{N} \left(\frac{\delta_i}{2} \times \Phi_i \times N_{det,i} \times \frac{1}{\chi_i^2} \right), \tag{2.2}$$

where we define the number of dips (N), the deviation at the peak of the dip (δ_i) as defined in eqn (1), the full-width half-maximum (FWHM) at each peak (Φ_i), number of r-band detections within the dip window (N_{det}), and the measured chi-square statistic of our Gaussian fit (χ^2). We define the dip edges (i.e., window) by locating the nearest points before and after the dip center where the light curve magnitude first returns to within half a standard deviation below the mean magnitude. We note this metric is for the entire ZTF light curve. Our heuristic scoring metric is designed to capture the full dipper history of a given light curve and rewards light curves with an overall small number of dips conditioned on the quality of the data (i.e., number of data available, and duration of the event). Our light curve scoring metric has a complicated selection function, in nature, due to the noisy ZTF light

curves. It is possible that a deep-short dipper can be scored similarly with a shallow-long dip, depending on the amplitude, duration, and number of available points in the duration of the dip. Since we also impose a chi-square penalty on the Gaussian fit, systems that are asymmetric will generally have slightly smaller scores compared to those with symmetric light curves. Throughout the analysis, we discovered events with very small χ^2 fits are likely bogus outliers with only one detection that has good agreement with a Gaussian; we penalized these events by implementing criteria that reduce or negate their score contribution when they exhibit narrow profiles (FWHM < 1.5 days), minimal deviation from the mean magnitude, or suspiciously perfect model fits. To test our light curve score metric in Section 4.5, we perform an injection-recovery analysis to understand the limitations and biases of our scoring system.

4.4 Addressing ZTF Systematics

ZTF photometry exhibits notable and known systematic effects, particularly near the CCD edges, where vignetting and other edge-related issues degrade the photometric accuracy across the *gri* filters, for example, see Malanchev et al. (2021). Additionally, columns with known defects or objects near saturated sources may cause spurious variability and can result in the misidentification of dipper-like candidate stars. Current bulk data releases of ZTF light curves, including Zubercal, do not provide PSF catalog-level information for individual detections nor any spatial constraints relative to the CCD edges. The absence of key parameters in the ZTF bulk release light curves, to assess the quality of the PSF of each source, including its position on the CCD, complicates the application of a straightforward spatial-photometric cut. In the ZTF Science Data System Advisories and Cautionary Notes[6], for instance, the PSF chi, and sharp parameters can be used to remove further spurious photometry, however, they are only available via the time-costly IRSA light curve GUI service query and not the bulk data release. In Figure 2.2, we display the ZTF-r band light curve of two commonly identified systematic effects via the light curves and ZTF Science images before and after we apply PSF-level queries from IRSA. We note that similar effects take place in the g-band filter with similar durations. Based on their light curves alone, such spurious detections that cause "dips" at first inspection can look convincing; however, stricter PSF requirements and inspection of the images provide more important context to reject such spurious events.

We investigated the distribution of dip times with the highest amplitude dip that occurred in each r-band light curve shown in Figure 2.3. Figure 2.3 reveals, there are several nights throughout the survey where large overdensities (on the order of 10^4 stars) of dips occur within the same night, and have a seasonal pattern. We suspect that this issue specifically arises during the warmest ambient temperature months at the Palomar Observatory, or can generally be attributed to bad weather conditions that cause spurious dips. In the final scoring distribution seen in Figure 2.4, we removed all dips that were within ± 0.5 days from the identified overdensity ($>10^4$) of stars that we have deemed likely bogus.

To assess and mitigate the impact of false dipper signals, we analyzed a subsample of 1,000 potential dipper candidates, uniformly sampled from the raw score distribution without

[6]ZTF Science Data System (ZSDS) Advisories and Cautionary Notes

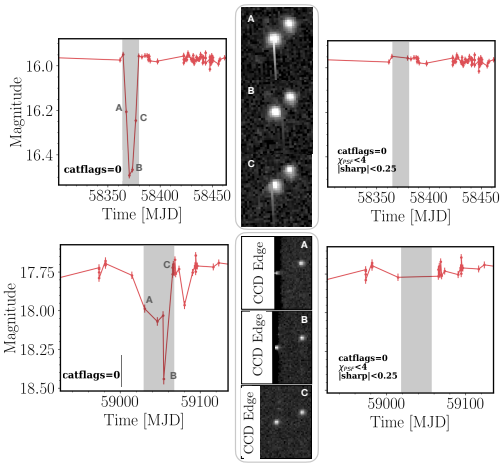


Figure 2.2: Examples of the two most common types of spurious dips in the ZTF r-band photometry: (top) OID 744211200016789 and (bottom) OID 736206200012619. The first column highlights the prominent dip-like directions with letters A-C, using only the catflags=0 condition. The central column shows the corresponding ZTF science image of each dip detection, where image artifacts are visible. The right column shows the light curve using constraint detections based on catalog-level PSF photometry, which is only available through IRSA.

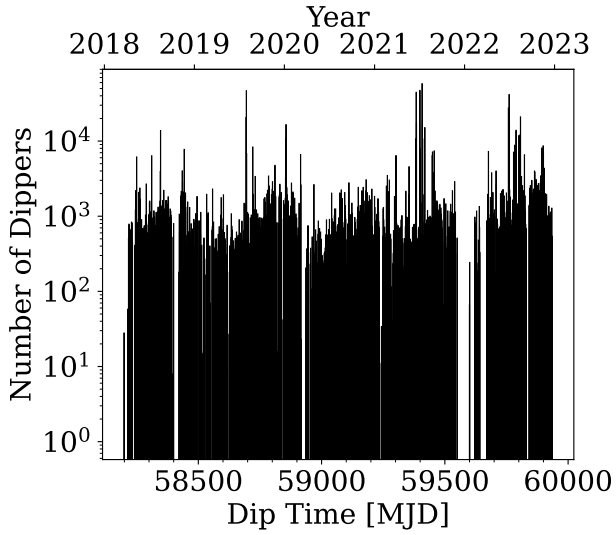


Figure 2.3: Modified Julian Date time of the highest magnitude deviations for each light curve, binned by a 1-day cadence. The systematics presented are temporary and spatially correlated.

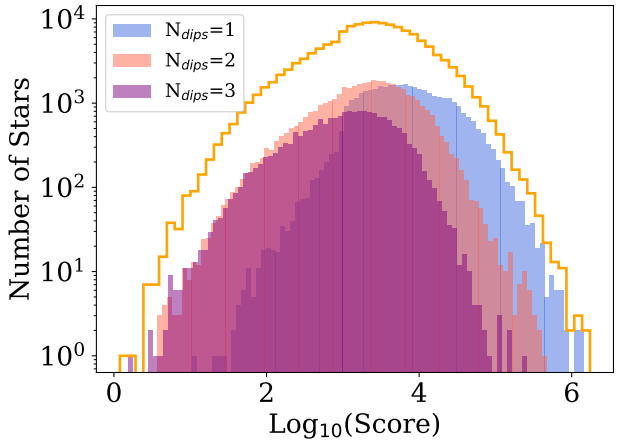


Figure 2.4: Histogram of the light curve dipper scores after removing bulk systematic errors from the sample. The orange line represents the total score distribution with minimal quality cuts, requiring each dip to have at least one detection at its minimum. The colored histograms, distinguished by the number of significant dips, apply more stringent criteria such that each dip has at least three detections during the dimming phase.

filtering for spurious dips. For each candidate, we retrieved IRSA-level photometry and applied more stringent PSF cuts, following the guidelines outlined in the ZTF Science Data System Advisories and Cautionary Notes (see right panel of Figure 2.2). After reprocessing the light curves through our scoring pipeline, we found that ∼90% of the sample failed to meet the scoring threshold, as spurious dimming events were effectively removed. The remaining light curves, however, exhibited subtle systematic effects not captured by our PSF cuts, requiring visual inspection to confirm their validity. We conclude that without more specific PSF-level parameters for each detection, we are currently unable to eliminate spurious signals without manual inspection of the science images. While this limitation does not preclude the discovery of our main-sequence dipper stars, we caution that the initial light curve scoring distribution includes a high contamination rate alongside bona fide events.

4.5 Injection-Recovery Simulations

To evaluate the efficiency of our light curve scoring pipeline, we conducted a basic injection-recovery test using simulated dipper events with the characteristics of the ZTF light curves. We selected a uniform sample of 10,000 stars across the sky footprint and magnitude range from the original 63 million sources that did not meet the initial $\delta > 3$ criterion to select an unbiased control set for our injection-recovery analysis, and avoiding sources that may exhibit significant photometric dips. We modeled each dipper-like event using a skew-normal distribution characterized by parameters for the mean (μ), standard deviation (σ), skewness (α), and offset term (C_0). To introduce variability and mimic observational noise, we perturbed the model as follows:

$$f(\mu, \sigma, \alpha, C_0) + \mathcal{N}(0, \sigma_{mag}) + \mathcal{N}(0, \sigma_{\sigma_{mag}}), \tag{2.3}$$

where $\sigma_{\rm mag}$ represents the standard deviation of the light curve, and $\sigma_{\sigma_{\rm mag}}$ is the standard deviation of the magnitude errors. To account for the dependency of magnitude errors on brightness, we estimated a 5th-order polynomial to approximate the average uncertainty as a function of magnitude for all 10,000 of our initial ZTF light curves. The modeled dimming event was then added to the observed data to produce the final simulated light curve. For simplicity, we assumed the dimming event amplitude to be identical in the *gr* bands.

We acknowledge that our simple skew-normal injection model does not physically simulate the underlying mechanisms driving the optical dimming events. This reflects the broader challenge that, to date, no study has conducted (i) a systematic search or (ii) a comprehensive characterization of light curve dimming profile shapes, which are likely influenced by complex and competing processes. For example, Boyajian's star and ASASSN-21qj have exhibited complex dimming profiles that deviate significantly from symmetric Gaussian shapes, while other dipper stars such as HD 166191 (Su et al., 2022a) show Gaussian-like symmetric dimming events in their optical light curves. Other optical dimming events have been characterized by the sum of multiple superimposed Gaussians with an underlying Poissonian component (Scaringi et al., 2016). Given the diversity in optical light curve phenomenology, the true functional form of the dimming profile remains uncertain. Thus, we recognize that the skew-normal distribution represented in our injection-recovery modeling is only an approximation for these events.

To evaluate our pipeline's performance, we simulated a grid of 100,000 amplitudes and durations to generate synthetic light curves by randomly sampling from the initial 10,000-star dataset. The mean time of the dimming event was randomly sampled from the time axis of the ZTF-r band light curve. For each synthetic light curve, we also drew a skewness parameter value randomly between -0.5 to 0.5 to simulate both symmetric and asymmetric dimming. Each light curve was injected with a single simulated dip. We processed these simulated light curves through our scoring pipeline and assessed the fraction of events that met our scoring criteria. Candidates were considered "detected" if they had $\log_{10}$(score)>3 and at least three detections during the dimming phase. To match observations, we translate each injected light curve by computing its fractional transit depth and timescale in Figure 2.5 and estimate a grid of the detection efficiency. Demonstrated in Figure 2.5, we found that our scoring pipeline is most sensitive (∼100% completeness) for events over 50 days with fractional transit depths above 40%. For shorter timescales around 10 days or less, we found that our detection efficiency varies between 20-60%.

Besides the detection efficiency, we also investigated the score distribution of our synthetic dipper light curves and other key summary statistics. For example, from the above example, we found the score distribution to be tightly marginalized between 8>$\log_{10}$(score)>3, which all contained a minimum of three detections in the dimming phase in the ZTF-r band light curve. The marginalized bounds of the light curve score ultimately reflect the cadence and noise properties of the ZTF light curves. In addition, we computed other auxiliary time-series statistics, such as the skewness, Von Neumann Ratio (von Neumann, 1941a,b) that measures the correlated variance and variance of each light curve that can inform our quality cuts based on the real ZTF light curves.

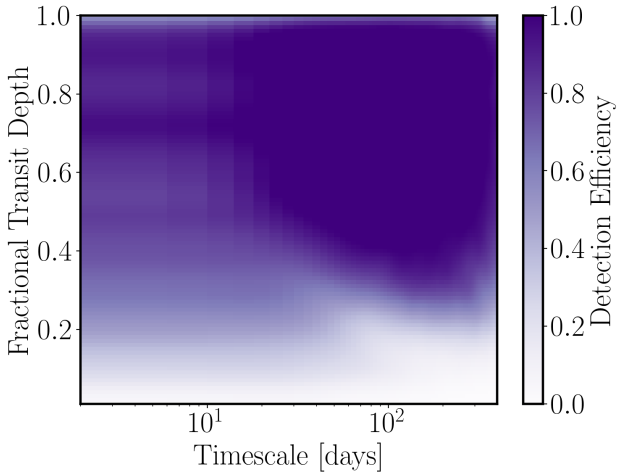


Figure 2.5: Simulated dipper star amplitude versus duration of the dimming event for our injection-recovery simulations. The color scale represents the median detection efficiency fraction, defined as the ratio of successfully detected events that pass our minimum light curve score criteria to the total number of simulated events per bin. The detection efficiency decreases for shallower and longer-duration dips, reflecting the limitations of our selection criteria and survey cadence.

4.6 Discovery Process

As discussed in the previous section, our first pass at removing ZTF systematics is presented in the light curve $\log_{10}$(score) distribution presented in the orange histogram of Figure 2.4. Based on our findings from the injection-recovery testing, we restrict our sample to consider potential candidates as those with $\log_{10}$(score)>3, must contain at least three detections within the identified dip, and have a skewness value above 0.6. With these first cuts, our sample is cut down to 57,729 candidates to investigate (23,185 one dip, 25,153 two dips, 9,391 three dips). We expect that these candidates remain dominated by false dips due to systematics (Section 4.4). Taking our estimated contamination rate of ∼90% would yield approximately 5,773 stars to investigate as true candidates that deserve more attention. We noticed that in our 57,729 candidate sample, there was still correlated temporal and positional structure across the sky, likely reflected by the untreated systematic effects present in the light curves. To further remove any systematic errors that are temporally and positionally correlated, we computed a spherical sky distance between each pairwise star[7] in our sample. We used the closest pairwise distance in this distribution as a threshold, removing sources that were unusually close in this 3D space that we believe are temporally and spatially correlated.

[7]We define the distance as

$$\mathbf{D} = \sqrt{r^2 + r'^2 - 2rr' \left(\sin\delta \sin\delta' \cos(\alpha - \alpha') + \cos\delta \cos\delta'\right)}$$

, where **r** and **r'** are the dip times of each source, multiplied by the speed of light (i.e., $r = c_0 \cdot t_{dip}$), resulting in a sky distance that accounts for the temporal distance between each dip. The terms α, α' and δ, δ' refer to the sky coordinates of each pair of sources.

The remaining 21,607 candidates were visually inspected to check for dipper signals and any unwanted systematic errors. Each source was inspected with the SNAD Viewer tool (Malanchev et al., 2023) to investigate each candidate. The SNAD Viewer provides interactive access to ZTF light curves, science images, and complementary data from other surveys. We visually inspected the dimming events in both ZTF *gr* science images found throughout our search and flagged sources that appeared as bona fide candidates. We repeated this process for events with up to three identified dips. Out of the ∼20,000 candidates, we have identified 81 promising candidates that we deem as main-sequence dippers.

We are aware of the shortcomings of this approach in combining both quality cuts and visual inspection, which may yield inconsistencies and biases toward certain variability signals. It is beyond the scope of this study to understand the complex selection function at play since we are dominated by systematic effects, as has been found in other studies (Malanchev et al., 2021). For example, Malanchev et al. (2021) showed a simple rule to potentially identify systematics in the ZTF light curves by noticing that they generally have higher reduced χ^2 and low period amplitudes. Future studies should consider prior treatment of the ZTF light curves to identify common light curve trends per ZTF field via techniques such as Cotrending Basis Vectors (Petigura & Marcy, 2012).

5 Properties

For the analysis of our 81 newly identified main-sequence dipper stars, we downloaded the most recent ZTF gr-band[8] ZTF 22 photometry directly from IRSA. To remove any spurious photometry, we applied the standard photometric quality criteria (i.e. `chi` > 4, |`sharp`|$<$ 0.25, and `catflags` $= 0$) recommended by the ZSDS as discussed in detail in Section 4.4. We provide Table 2.6 that contains the associated coordinates, magnitudes, distance, time of dip, and number of dips in the ZTF light curves.

5.1 Timescales and Depths

The photometric behavior of our main-sequence dipper sample exhibits diverse light curve morphologies that provide important clues into the underlying occulting mechanisms. Through systematic analysis of the ZTF light curves, we identify several distinct categories of dimming events characterized by their temporal evolution, amplitude, and shape symmetry. Complex and irregular stellar dimming events have been observed across various systems, including VVV-WIT-07 (Saito et al., 2019), ASASSN-21qj (Kenworthy et al., 2023a; Marshall et al., 2023a), J1407 (Mamajek et al., 2012), EPIC 204278916 (Scaringi et al., 2016), and KIC 8462852 (Boyajian et al., 2016c). These events have revealed diverse occulting phenomena, including giant ring systems (Kenworthy & Mamajek, 2015b), tidally disrupted circumstellar disks (Rodriguez et al., 2013), dust clumps in YSO accretion disks (Bodman et al., 2017; Bouvier et al., 2003), and planetesimal interactions (Grinin et al., 2010). Our search yielded a total of 81 dipper candidates, which we categorized based on the frequency of observed dipping events: 62 candidates (76.5%) exhibited a single dip, 11 candidates (13.6%) showed

[8]We exclude the ZTF i-band data since none of our dips contained any i-band detections.

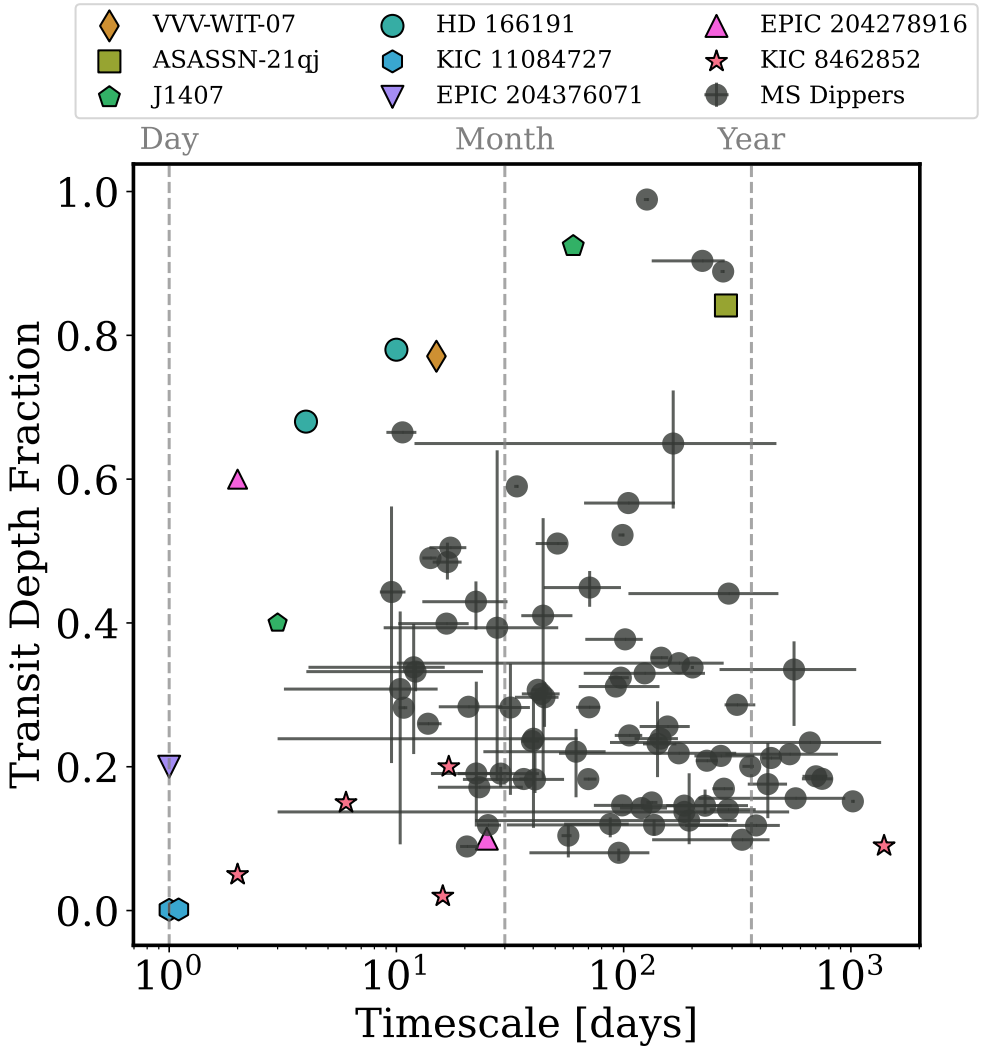


Figure 2.6: Fractional transit depth versus dimming timescale for main-sequence dipper stars. The fractional transit depth is defined as one minus the minimum normalized flux. Black points represent data from this work, and error bars indicate the range of dimming durations and depths for sources with multiple dimming events. The dashed lines indicate the timescale of days, months, and years. For comparison, data from analogous dipper-like phenomena reported in the literature are included: VVV-WIT-07 (Saito et al., 2019), ASASSN-21qj (Kenworthy et al., 2023a; Marshall et al., 2023a), J1407 (Mamajek et al., 2012), HD 166191 (Su et al., 2022a), KIC 11084727 (Rappaport et al., 2018b), EPIC 204376071 (Rappaport et al., 2019), EPIC 204278916 (Scaringi et al., 2016), and KIC 8462852 (Boyajian et al., 2016c).

two distinct dips, and 8 candidates (9.9%) displayed three dipping events during the photometric baseline conducted for this study. Table 2.1 summarizes the number of light curves classified as symmetric, asymmetric, and erratic, determined through visual inspection of their ZTF light curves. In this work, we present ZTF *gr*-band normalized flux light curves from our newly identified main-sequence dipper stars presented in the , Figures 2.24–2.28. The normalized flux is computed as f=$10^{m-M/-2.5}$ where M is the estimated biweight mean of the baseline quiescent light curve.

Morphology Type	**Count**	**Fraction**
Symmetric	20	0.25
Asymmetric	35	0.43
Erratic	26	0.32

Table 2.1: Light curve morphology classification based on visual inspection.

Our analysis reveals two distinct populations: systems exhibiting single isolated high-amplitude dimming events and those showing multiple dimming episodes. Figure 2.6 presents the normalized fractional depth versus event timescale for our sample, with fractional depth defined[9] at the baseline quiescence of the star. Event durations were determined through visual inspection, marking the start and end time on the epochs of the onset of the ingress and egress of each dip. This deliberate choice was due to ZTF's relatively sparse sampling and the irregular morphology of the dimming events. For context, we include previously reported dipper-like phenomena from the literature. Our light curve timescales span from 3-2000 days, with an average of 100-day duration, with typical fractional depths of ∼35%. A small subset (∼6%) exhibits more extreme characteristics, with fraction depths exceeding 60% with an average duration of 120 days, suggesting these events are intrinsically rare compared to the low-amplitude-long-duration events. Notably, three of these sources, ZTF18aaypgug (Delgado et al., 2019), ZTF18acebnyy, and ZTF18aboksfn exhibit transit-like features, with fractional transit depths exceeding 90%. Our findings support the bimodality in event timescales previously suggested by Schmidt (2019), with distinct populations of fast and slow dimming events. The sample displays diverse morphologies, including symmetric, asymmetric, and erratic dimming profiles, as demonstrated more carefully in a selected subset of ZTF light curves shown in Figure 2.7.

Our sample exhibits clear selection effects favoring week-to-month timescale events, primarily driven by two factors: our light curve scoring criteria and ZTF's optimal sensitivity window, which is better suited for detecting longer-duration events compared to those approaching the sampling cadence. Nevertheless, the observed distribution of timescales and depths reveals a population of dimming stars spanning broad ranges in both parameters. Notably, extreme dimming events with depths >80% are rare, comprising only 3.7% of our main-sequence dipper sample. The absence of distinct clustering in the timescale-depth parameter space (Figure 2.6) suggests these phenomena occur across a wide temporal range. We found at least 5 candidates that are close to the timescales and depths seen in one of the Boyajian star dips (Dip 8 D1500), and a surprising resemblance in light curve morphology, however, with substantially higher amplitude and duration, for example, shown in Figure

[9]Normalized fractional depth is defined relative to the baseline flux level normalized to 1.

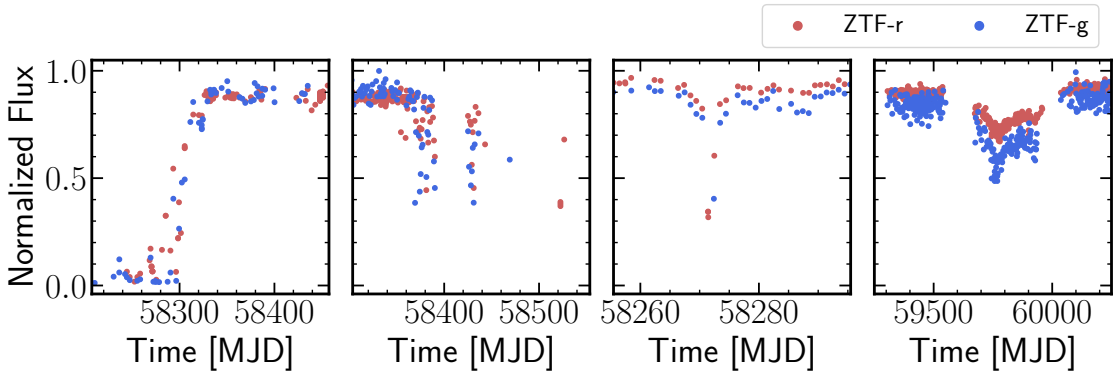


Figure 2.7: Example trimmed light curves of four identified main-sequence dipper candidates, focused on the identified dips. Each panel represents a different dipper star, showing distinct dimming events with varying depths, durations, and structures. The dips exhibit a range of morphologies and timescales.

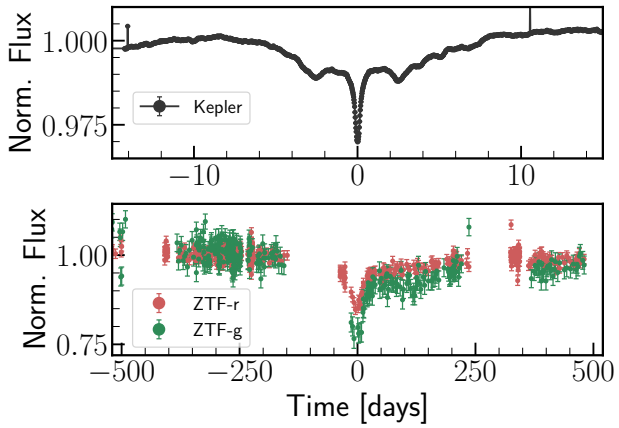


Figure 2.8: (Top) Normalized Kepler light curve of the Boyajian star (D1500 Dip 9) over a ±10-day interval. (Bottom) Normalized ZTF-*gr* light curve of ZTF18acqbwiz for comparison, shown over a ±500-day interval. We note the striking resemblance in light curve morphology, though the dip in ZTF18acqbwiz is significantly deeper and longer in duration. Each light curve is shown with its original time baseline to maintain the observed temporal structure.

2.8. The apparent absence of events with depths <10% reflects ZTF's noise floor, particularly at timescales below 3 days, which are constrained by the survey's average two-night cadence.

5.2 Light Curve Shapes

Understanding the light curve shape of the dimming events could help constrain the physical structure and motion of the obscuring material. For instance, asymmetric dimming profiles like those seen example candidate, Figure 2.7, could be attributed to extended dust tails, warped disks, and circumstellar material on non-circular orbits. We therefore assess the degree of symmetry in each light curve dip to identify potential patterns in our newly discovered main-sequence dipper stars. For each main-sequence dipper light curve dimming event, we measure the light curve dipper symmetry score defined as follows:

$$\mathcal{I}_{i,j} = \sum_{n=i}^{j} (R_m - f_n) \cdot \frac{t_{n+1} - t_{n-1}}{2}, \tag{2.4}$$

where t_n is the time and f_n the normalized flux at which observation n was taken, and R_m is the robust biweight mean of the normalized flux ZTF-r light curve, which we assume to be the quiescent baseline of the light curve. To measure the symmetry score of a dip, we compare the integrals from a point in the center of the dip at index c to the start and end of the dip window at indices s and e, respectively. We calculate the asymmetry score as:

$$\text{Symmetry Score} = \frac{\mathcal{I}_{s,c} - \mathcal{I}_{c,e}}{\sqrt{\sigma^2_{\mathcal{I}_{s,c}} + \sigma^2_{\mathcal{I}_{c,e}}}}\ , \tag{2.5}$$

where we combine the normalized flux of each *gr* light curve, linearly interpolate them, and estimate the asymmetry score as defined from above. In Figure 2.9, we present the light curve dipper symmetry scores against the identified dipper timescales. Events close to zero are generally considered to be symmetric dimming events, while those with positive or negative values will have skewed dimming profiles, such as longer ingress or longer egress, respectively. We find no strong correlation between the light curve symmetry score and dip timescale. However, the overall distribution of symmetry scores (top panel of Figure 2.9) shows a modest negative skew of -0.3, with a median of -0.7, suggesting a small preference for dips with shorter ingress and longer ingress timescales. Since ZTF's irregular cadence can lead to poor sampling, we assess whether this asymmetry could arise purely from sampling effects. Using the simulated light curves in Section 4.5, we simulated 1,000 dipper light curves with symmetric dimming (i.e., skewness parameter $a = 0$) with varying amplitude and time of dip, while keeping the duration constant. Following the same light curve symmetry score calculation, we ran a Monte Carlo simulation sampling our synthetic symmetric dimming and sampling them without replacement, and recorded the number of events with negative values. We find that the number of negative symmetry scores in the real data lies $\sim 3\sigma$ above the expected mean from our simulations, indicating that the observed negative skewness is moderately unlikely to result from sampling noise. Our tests indicate a statistically significant excess of dips with faster ingress and longer egress, perhaps consistent

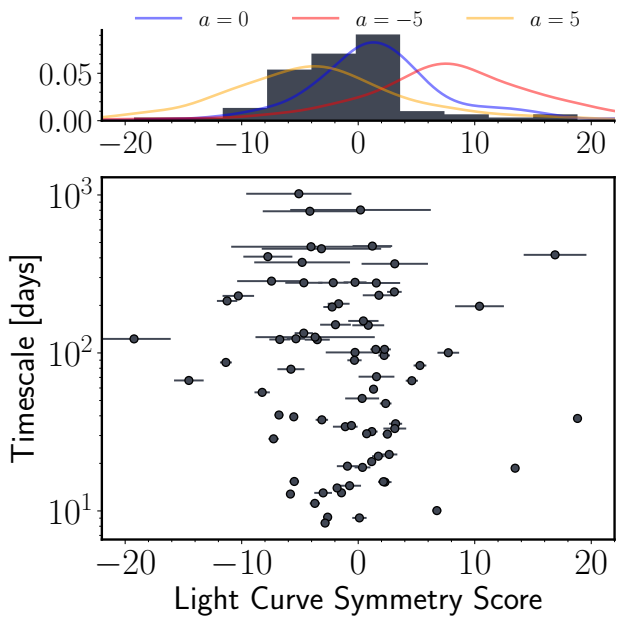


Figure 2.9: (Bottom) Dipper timescale versus light curve dipper symmetry score. The symmetry score quantifies the temporal structure of each dimming event, where values near zero represent symmetry dimming events. Positive values indicate longer ingress phases, while negative values denote longer egress phases. (Top) Normalized density histogram of light curve dipper symmetry score. Solid colored lines are simulated distributions of dipper light curves with symmetric dimmings (blue; $a = 0$), positive skew (orange; $a > 0$), and negative skew (red; $a < 0$).

with the scenario where trailing structures, such as dust clumps with extended trails, can cause leading edge occultations, as we will further explore in Section 6.1.

5.3 Light Color Evolution Properties

Beyond the amplitude, temporal, and shape variations alone, the temporal color behavior of our main-sequence dippers provides additional constraints on the nature of the obscuring material. Here, we analyze the ZTF-*gr* color evolution of our sample to determine whether significant chromatic changes accompany any dips, and if those changes support reddening scenarios or point to alternative scenarios.

We analyze the ZTF *gr* color properties of dippers through multiple approaches. First, we examine the color difference between quiescent baseline and dimming events for all the observed dips in their ZTF light curves. Figure 2.10 shows the distribution of ZTF $(g - r)$ color differences between the stellar baseline (measured as the median magnitude outside the dimming events) and during dimming episodes (computed as the mean magnitude during the dip defined in Section 4.3). The median color difference is -0.01 mag, with a 2.3 standard deviation that extends to both redder (<0) and bluer (>0) color changes. We found 77% and 23% of the dips were below and above zero, respectively, suggesting that most dimming exhibited moderate levels of reddening compared to their quiescent baseline. Interestingly,

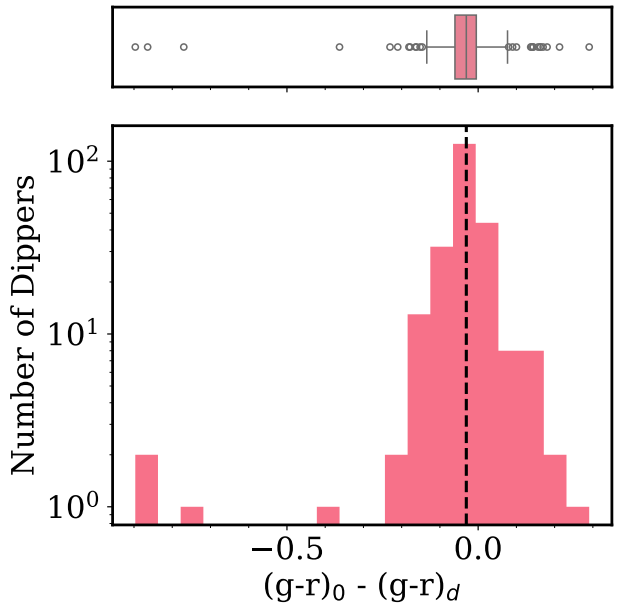


Figure 2.10: (Bottom) Histogram of the ZTF $(g-r)$ colors for the identified main-sequence dippers. The color excess, defined as $(g-r)_0 - (g-r)_d$, represents the deviation from the mean of the quiescent phase of each light curve, where $(g-r)_d$ is the median color near the centroid of the dimming event. The black dashed line marks the median of the distribution. (Top) A box plot of the color excess is shown at the top of the histogram, illustrating the interquartile range.

we discovered a significant negative correlation between color change and dip amplitude, with higher amplitude events generally exhibiting redder colors, which likely reflects the extinction effects from the occulting material.

Next, to investigate the color magnitude diagram (CMD) across our entire observation period, we implemented a modified 3-day running median on the combined light curves. Standard running median methods were found to underestimate the true color behavior. To estimate as closely as possible the true color properties of our light curves, we developed an adaptive binning approach where the maximum magnitude within each 3-day window was selected when the light curve showed excursions exceeding 0.3 mag from the baseline. Following the methods outlined in Poppenhaeger et al. (2015), for each source, we constructed CMD and quantified their slopes using Orthogonal Distance Regression via `scipy.odr`, which employs a Levenberg–Marquardt algorithm that accounts for uncertainties in both axes. The slope angles, defined as the inverse tangent of the linear regression coefficients, were compared against typical interstellar medium (ISM) reddening laws (Fitzpatrick, 1999a; Fitzpatrick & Massa, 1990). We show a typical fit to the CMD in Figure 2.11. To ensure our results were not an artifact of the temporal binning, we repeated the analysis with bin widths of 0.5, 1, and 3 days, obtaining consistent results across all trials. Our analysis reveals that the majority of sources exhibit shallower slopes than those predicted by high-RV ISM extinction curves, where roughly 10% of our sources are within the margin of typical RSM reddening slopes. The median slope angle in our sample is 54.7 degrees, substantially lower than typical

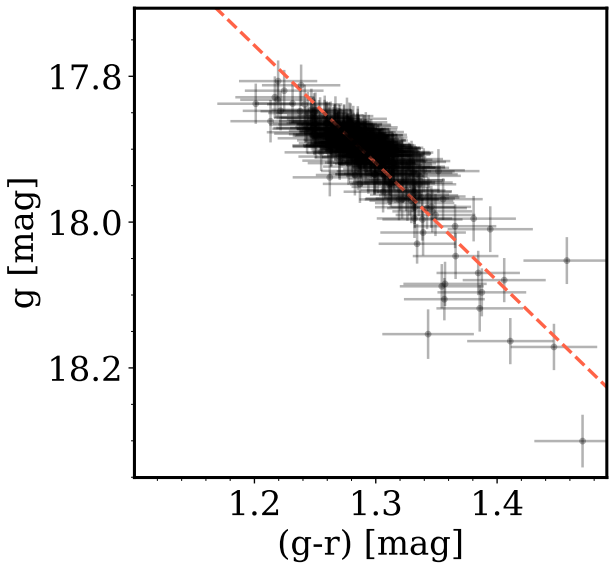


Figure 2.11: Example of ZTF19aawfjbq ZTF color-magnitude slope. The dashed red line represents the best-fit line.

ISM slope angles between 74.1 and 79.2 degrees for Rv values of 3.1 and 5, respectively (Hillenbrand et al., 2022a). The distribution of CMD slopes is presented in Figure 2.12. The observed slope angles suggest that if extinction is responsible for the dimming, the occulting material likely has small R_v values (<2), indicating grain sizes smaller than or comparable to the observed wavelength ($\sim$ 0.4μm), though based on CMD slopes, our results seem to indicate that are shallower than other anticipated effects such as hot spots, cool spots, accretion or scattering Poppenhaeger et al. (2015). We interpret the skewed $(g-r)$ slope angle away from ISM reddening slopes as potential evidence for localized and non-symmetric obscuration events with different geometry or grain properties than typical ISM values. We detect a moderate but statistically significant correlation (Pearson-R = 0.46, p <0.0001) between event timescale and color-magnitude slope, as shown in Figure 2.13. The global color properties and temporal correlation could indicate an intrinsic relationship between event duration and the dimming properties, though we note that longer-duration events inherently provide a better sampling of color evolution, potentially introducing a measuring bias.

5.4 Demographics

The current work contains one of the largest samples of main-sequence dipper stars in a confined color-locus and marginalized stellar parameter phase space. At the moment, it remains unclear if all discovered systems in our sample are indeed driven by the same mechanism of variability (i.e., intrinsic or extrinsic). For simplicity, we will assume that broadly most of our discovered systems belong to the same class of variable stars, for example, systems with one versus multiple dips, or characteristic timescales.

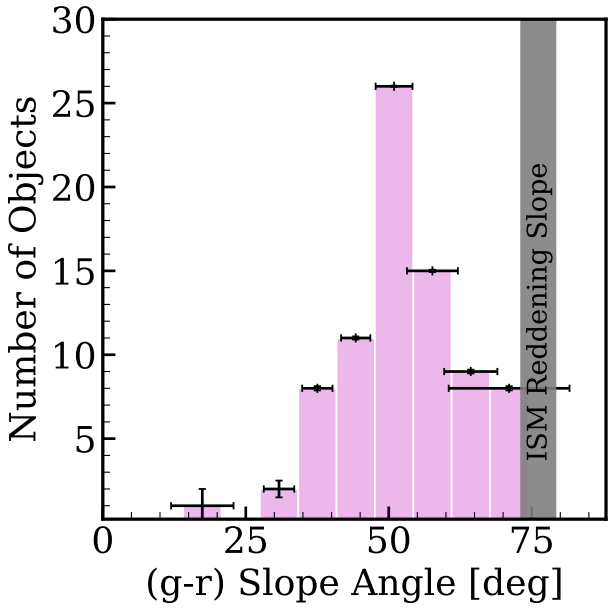


Figure 2.12: Histogram of the fitted ZTF $(g-r)$ slope angle in degrees, including their standard errors and median slope angle errors. We denote in the gray region, where typical ISM reddening slope values occur between $3 < Rv < 5$.

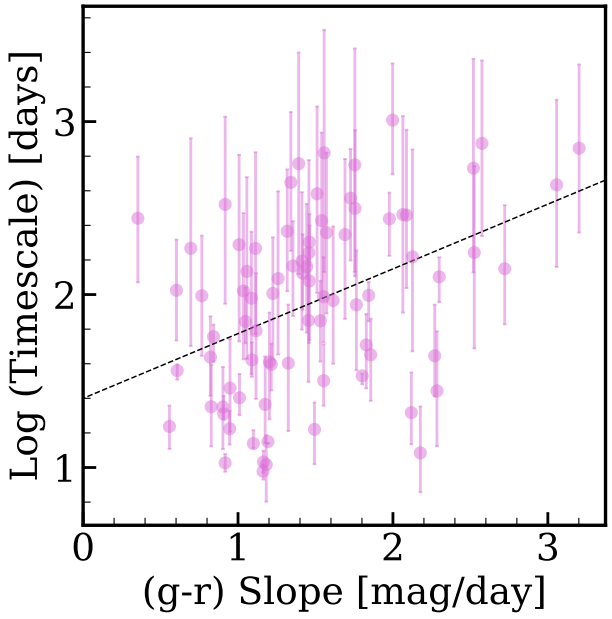


Figure 2.13: Correlation between event timescale and $(g-r)$ color slope. The obtained data suggest that longer-timescale dimming events generally exhibit steeper $(g-r)$ slopes compared to shorter-timescale events. The black line represents the best-fit line using a least-squares optimization.

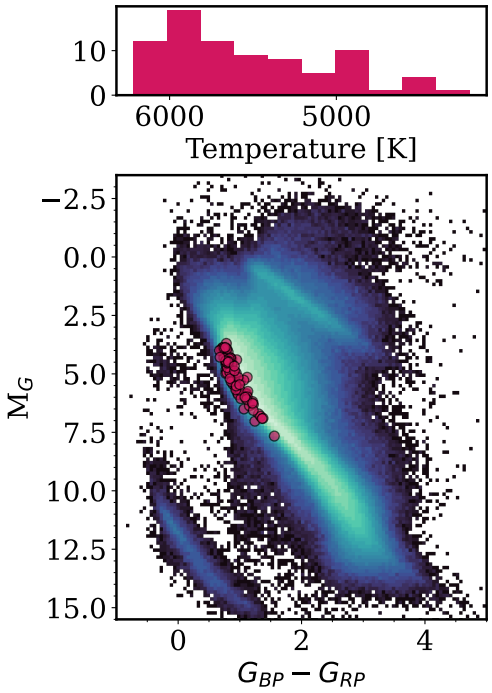


Figure 2.14: Color-magnitude diagram (blue) for the nearby Gaia DR3 sample (Gaia Collaboration et al., 2022a), shaded by the number of stars per bin. The positions of our identified main-sequence dipper stars, corrected for extinction using estimates from Anders et al. (2022), are overplotted. The top panel shows the 50th percentile of the effective temperature posterior distribution for our main-sequence dipper stars obtained by the `StarHorse` 2022 catalog.

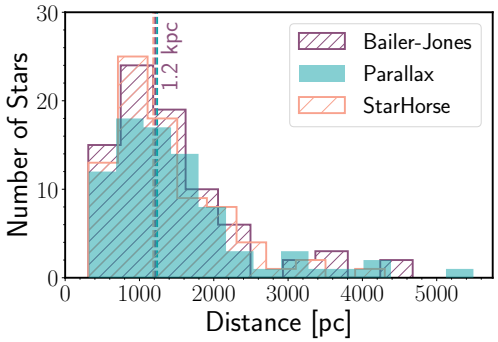


Figure 2.15: Histogram of the distances to our main-sequence dipper stars, as measured in three separate catalogs: Bailer-Jones (Bailer-Jones et al., 2021a), parallax (Gaia Collaboration et al., 2022a), and `StarHorse` 2022. The dashed lines indicate the median distance for each distribution.

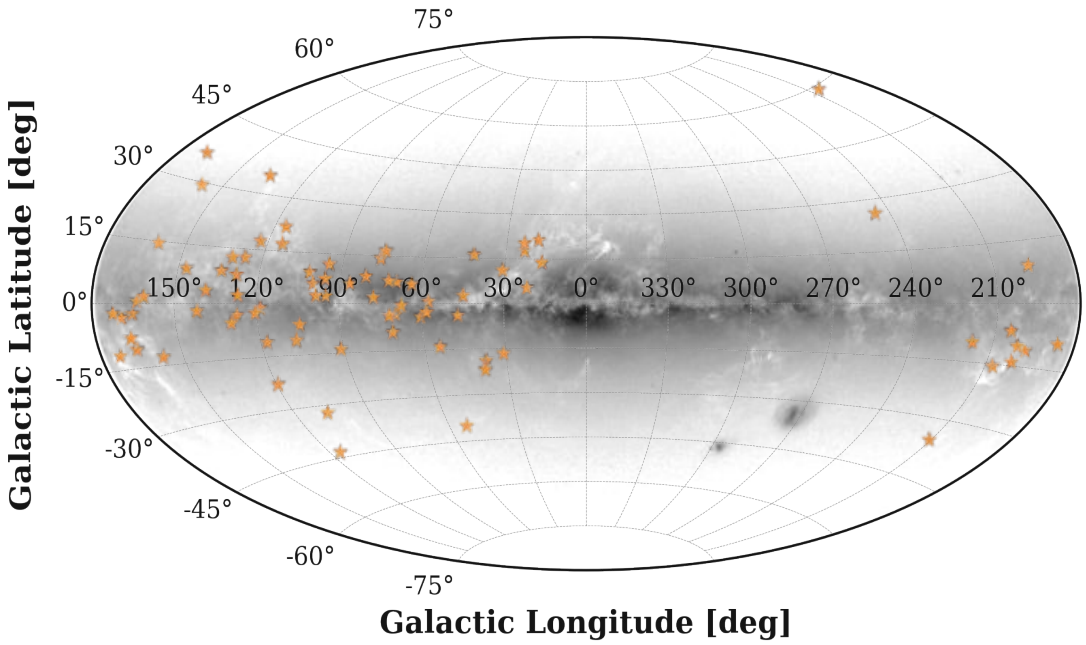


Figure 2.16: Sky positions of the identified main-sequence dipper candidates (orange points) in Galactic coordinates. The background color map represents the number of Gaia DR3 sources per bin, highlighting the density of stars across the sky.

First, we investigate the position of our discovered main-sequence dipper sample on the Gaia color-magnitude diagram. In Figure 2.14, we display a sample of the Gaia color-magnitude diagram (background blue density) and overplot the positions of the main-sequence dippers using distances estimated by `StarHorse 2022` that have also been corrected for the inferred line-of-sight extinction in the Gaia-G band (A_G). As expected, our sample lies along a tight locus near where we expect most FGK dwarfs to be found. On the top panel of Figure 2.14, we show the 50^{th} percentile effective temperature of the stellar parameter and notice a slight overdensity of events above >5,500 Kelvin. We went back to our initial sample and ran a Kolmogorov-Smirnov (KS) test on the two distributions to investigate if the overdensity in hotter stars was real. We found strong agreement with the two distributions, with p-value >0.05, thus not able to reject the null hypothesis and therefore conclude that our bias temperature likely comes from our sample selection criteria. The median distance is 1.2 kpc with an average uncertainty at $G_{mag} < 18$ around 30%, confirmed by the Bailer-Jones (Bailer-Jones et al., 2021a), Parallax (Gaia Collaboration et al., 2022a), and `StarHorse 2022` measurements, shown in Figure 2.15.

The sky distribution of our main-sequence sample is biased toward the Galactic disk (see Figure 2.16), where the stellar density is the highest. The median proper motions reported by Gaia DR3 μ_α=-0.09 mas yr^{-1}, μ_δ=-3.0 mas yr^{-1} with standard deviation 6.7, 5.8 for each vector, respectively. These values are well within the average velocity dispersion for field stars, although without the full 6D (i.e., missing radial velocity measurements), we cannot confidently rule out this scenario.

Given the positions and distance of our main-sequence dippers, we investigated whether

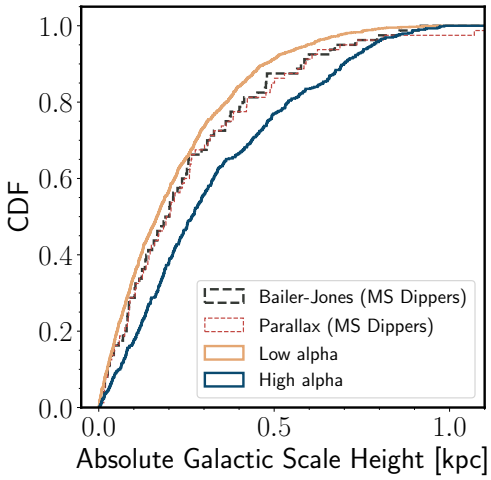


Figure 2.17: Cumulative distribution function (CDF) of the absolute Galactic scale height for main-sequence dipper candidates, compared with low-alpha and high-alpha disk populations of single stars. The dashed and dotted lines represent the distributions for dipper candidates based on distance estimates from Bailer-Jones (Bailer-Jones et al., 2021a) and the Gaia DR3 parallax measurements, respectively. The solid orange and blue lines correspond to the low-alpha and high-alpha disk populations.

any are associated with young stellar associations or star-forming regions. First, we used the BANYAN Σ code (Gagné et al., 2018) that estimates the Bayesian probability of members of young stellar associations within 150 pc of the Sun. We used the reported Gaia DR3 proper motion, parallax, and coordinates of each candidate to assess the BANYAN Σ probabilities. For each star in our sample, we found the probability of being a field star is $> 99\%$. We note that the majority of our sources do not contain any radial velocity measurements[10] Next, we searched using a 1-arcsecond cone search in a homogeneous catalog of 1867 well-characterized stellar clusters using Gaia DR2 astrometry and photometry with cluster distances and ages (Cantat-Gaudin, T. et al., 2020) and identified two candidates with well-matched distances. ZTF18abbvemu, which is a member of the ASCC 114 open cluster (Kharchenko, N. V. et al., 2005) with an estimated age of 7 Myr (Elias et al., 2009), and ZTF18aboksfn, which is part of the RSG-5 cluster with an estimated age of ∼40 Myr (Bouma et al., 2024; Röser et al., 2016). We conducted another cone search centered on known star-forming regions and clusters listed in Table 1 of Prisinzano et al. (2022) within <1.5 kpc, chosen to approximately match the radius that contains half of the identified members. While 10 of our sources are colocated in proximity to known SFRs, only one appears to be located at a distance consistent with the associated region. This source has been flagged as a potential YSO, ZTF19aayvizm, and may be associated with the Cygnus X star-forming complex, which has an estimated age up to ∼10 Myr. At least two other candidates have been identified to belong to open clusters, though with low probability, as discussed in Table **??**. Future

[10]As noted in Gagné et al. (2018), typically the missing quantities (i.e., radial velocity) are marginalized over using Bayesian inference, integrating across the full range of plausible radial velocities at the given position. This approach accounts for the uncertainty introduced by the missing data while still enabling robust membership probability estimates.

spectroscopic follow-up programs could fill in missing radial-velocity data to check more concretely for membership probabilities. Stellar age is a particularly interesting proxy for contextualizing the classification observed in stellar variability. For example, young stars can exhibit a spread in photometric morphology (Cody & Hillenbrand, 2018a) across many timescales and amplitudes (Fischer et al., 2023). The stellar age of our discovered systems has significant constraints on the progenitor material that must produce a large portion of the occulting material. Stars younger than 20 Myr, for example, may still have evidence of prominent bursts or dust occultation due to accretion and substructure of circumstellar material (Capistrant et al., 2022). We performed another KS test to compare our sample's distribution with the low and high alpha disk populations of the Milky Way within 1 kpc using `Cogsworth` (Wagg et al., 2025) code. Our results show a strong agreement with the low-alpha disk, with a p-value of 0.59, suggesting that our sample is dominated by younger, low-alpha stars. In contrast, the high-alpha disk comparison yielded a lower p-value of 0.036, indicating a statistically significant deviation from this older stellar population.

5.5 Periodicity

In this section, we discuss the potential implications of discovering periodic sources. To assess the presence of any periodic signal in our discovered systems using a Lomb-Scargle Periodogram (LSP) (Lomb, 1976a; Scargle, 1982a). We used the `AstroML` LSP implementation (Vanderplas et al., 2012). We run this implementation for the ZTF-r band light curves. To estimate the significance of each LSP iteration, we used a bootstrap simulation of 1,000 simulations by re-drawing from the original light curve with replacement, and computed the 1% and 5% significance level of each periodogram. For each computed periodogram, we investigated all peaks that were above the 1% significance level as potential periodic signals in our data. To exclude possible systematic cadence effects from ZTF light curves, we removed any significant periods that were within a few hours of known alias frequencies and their harmonics close to the sidereal day and cadence of ZTF (Coughlin et al., 2021). For the remaining period candidates that were above the 1% level and are not near known alias periods, we then took each light curve and phase-folded each at the period to investigate the overall scatter in the light curve. We identified at least one candidate (ZTF19adgqwvh; coordinates (ra, dec)=144.75644, -20.05037, seen in the second column of Figure 2.28) that appears to be strongly periodic close to an orbital period of 0.992 days, and we suspect it to be an eclipsing binary close to the ZTF average cadence. For a few candidates, we identified a ∼0.1 mag periodic modulation at approximately 29.6 days that could well be within the anticipated nominal stellar rotation of main-sequence stars (e.g., Nielsen et al. (2013)), though we caution that this period is also very close to the lunar phase period. The majority of our candidates appeared to have no obvious periodic signals that coincide with the observed dips. For additional validation, we conducted a conesearch around a ZTF periodic catalog by Chen et al. (2020). We found 14 crossmatches from their catalog and visually inspected the phase-folded ZTF light curves at the reported periods by Chen et al. (2020). In our investigation, we identified one compelling source (ZTFJ213811.15+535115.4), which appears to have a low-duty cycle ∼0.1 mag variability at 2.57 day period and has been flagged as a BY Draconis-like variable. The remaining sources appeared to have no coherent structure in their phase-folded light curves. We also inspected the Renormalized Unit

Weight Error (RUWE) from Gaia DR3 to infer the likelihood of a companion leading to astrometric excess noise. Generally, systems with an RUWE score of ∼1 are consistent with single stars, while thresholds above 1.4 can indicate the presence of a companion (Belokurov et al., 2020; Ziegler et al., 2020). Out of the 81 candidates, we found 5 stars with RUWE above 1.4 (ZTF18absdnwk, ZTF18actxeox, ZTF18actxeox, Gaia DR3 3807152512626432000, Gaia DR3 1084506523872363008) that could potentially host companions. Although Fitton et al. (2022) has suggested that large RUWE scores can also be associated with young stars with circumstellar disks, these 5 systems do not seem to have any particular infrared excess in the 2MASS and WISE bandpasses. However, further high-resolution imaging or radial velocity observations are still required to determine the presence of a potential companion and its properties.

5.6 Infrared Properties

To characterize the infrared properties of our main-sequence dipper stars, we analyzed archival data from 2MASS and WISE. We utilized the unWISE catalog (Schlafly et al., 2019) for the WISE data, which is particularly valuable for our candidates located in crowded Galactic fields. The unWISE catalog combines approximately 25 million single-frame WISE images into a deep coadd, enabling more accurate modeling of heavily blended sources in the WISE 3-5μm W_1 and W_2 bandpasses. To measure the infrared magnitudes with unWISE, we utilized the time-domain data from the unTimely data (Meisner et al., 2023a). Using the ZTF coordinates, we crossmatched to the 2MASS and unTimely catalogs, assuming a 1-arcsecond radius. We found 69 such sources, making up 85% of our initial sample. To measure the W_1 and W_2 magnitudes we took all source detections from unTimely and enforced that the fraction of flux in this object's PSF that comes from this object is above 50%, the quality factor above 90%, and target distance is less than 3-arcseconds from the initial query coordinates, and take the median of all epochs W_1 and W_2 measurements. In Figure 2.18, we show the color-color diagram of our identified stars, including the Z-score variability of the W_1 unTimely light curves of each star. For comparison, we included the 2MASS-WISE color-color positions of known Class I and Class II, and transition disk young stellar objects discovered in the Sh2-112 Filamentary Cloud Complex Panja et al. (2022). We marked the boundary separations for Class I, II, and traditional disks following the separation boundary described by (Koenig & Leisawitz, 2014). In Figure 2.18, we found that all 69 sources are well within the main-sequence stellar locus, though we interpret the small W_1-W_2 spread for the stellar locus to be due to the effects of metallicity (Davenport & Dorn-Wallenstein, 2019). Our search resulted in no obvious sources with bright infrared magnitudes, or any large amounts of time-domain infrared W_1 variability less than $< 3\sigma$. Within the 2MASS-WISE CMD, it appears that all 69 sources are within the color-color regime of either the main-sequence locus or transitional disks. In addition, we visually inspected the unTimely W_1 and W_2 light curves. We did not find any peculiar sources that exhibited infrared brightening or dimming within the identified times of our main-sequence dipper stars within the average 187-day unTimely light curve cadence. It remains unclear if the remaining 12 main-sequence dipper sources have infrared excess or large amounts of variability, and we encourage follow-up.

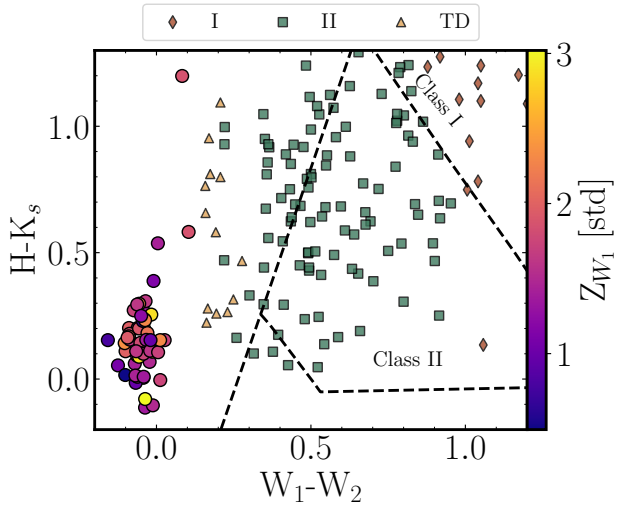


Figure 2.18: 2MASS and WISE color-color diagram of our identified main-sequence dippers, color-coded by the WISE W_1 variability Z-score indicated in the color bar. The dashed lines indicate the typical boundaries for Class I and Class II young stellar objects, following (Koenig & Leisawitz, 2014). For comparison, we include the 2MASS/WISE colors obtained by Panja et al. (2022).

5.7 Auxiliary Surveys

The identification of H_α excess emission can be a telltale sign of the type of variable star that can be driving such anomalous dips. Since most of our sources are in the Galactic plane, we searched to find our sources in the INT/WFC Photometric H_α Survey of the Northern Galactic Plane (IPHAS) Data-Release 2 catalog (Barentsen et al., 2014). We crossmatched our stars to the IPHAS DR2 survey with a 1-arcsecond cone search and found 33 sources. In Figure 2.19 we demonstrate the IPHAS color-color diagram of our identified sources with the IPHAS $(r - H_\alpha)$ and $(r - i)$ photometry. The majority of our stars lie on a locus that is consistent with the predictions of the SED stellar locus of main-sequence stars seen in the solid and dashed line obtained by Drew et al. (2005). Using the relationship between the color-color locus, we show in Figure 2.19 the anticipated equivalent width (EW). Based on the reported IPHAS photometry, only one source was found to have moderate levels of H_α emission. As we mentioned, we found one of our systems to have a high excess in the IPHAS $(r - H_\alpha)$ color, which is interpreted to have the presence of H_α emission. We have identified the candidate ZTF18aaypgug (also reported as Gaia19aow Delgado et al., 2019). Upon closer inspection of the ZTF-*gr* light curve of ZTF18aaypgug near the start of 2019, the identified source exhibited a >1.5 mag dimming event that lasted for several months. After the 2019 dimming event, the light curve has a significant scatter outside of the dimming event of 0.1 mag in each band. We inspected the ZTF science images and ruled out contaminating neighboring sources (the closest star is >5 arcseconds away). We ran several iterations of the LS periodogram on the data by sampling various timelines of the ZTF-r light curve and were unable to find any significant periods between a few hours and 150 days that minimized the initial intrinsic scatter of the phase-folded light curve.

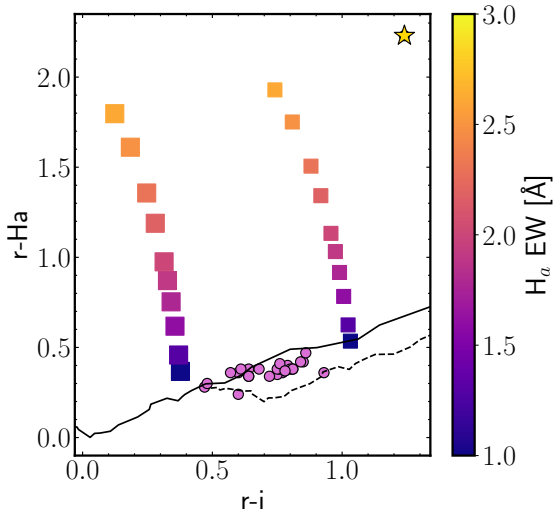


Figure 2.19: IPHAS color-color diagram showing (r–i) versus (r–H_α) for our identified dipper candidates. The pink dots represent the identified main-sequence (MS) dippers, including a bona fide Hα emitter (star symbol) in the top right corner. The black solid and dashed lines indicate the main-sequence stellar locus for extinction values of E(B–V) = 0 and E(B–V) = 1, respectively. The square-colored markers represent the predicted color evolution of a G2V star, color-coded by the logarithm of the Hα equivalent width (in Å), with separate tracks corresponding to E(B–V) = 0 and E(B–V) = 1. Out of our 81 identified dipper candidates, 33 are found in the IPHAS DR2 catalog.

By comparing the color-color location of ZTF18aaypgug, we note that these colors are within the range of typical S-type Symbiotic binaries (Sb). S-type Sb systems are interacting long-period binaries composed of a compact hot white dwarf accreting wind from a cool Red Giant Branch (RGB) star companion (Corradi et al., 2008). The majority of these systems are known for large orbital periods between 200 to 6000 days (Corradi et al., 2003) and can exhibit complex light curve behavior that involves ellipsoidal variability connected with orbital motion (S-type), radial pulsations, and semi-regular variation of the cool component (Gromadzki et al., 2013) due to dust (D-type). D-type Sb are known to have larger orbital periods on the order of at least >20 years. Based on the position of ZTF18aaypgug on the IPHAS color-color diagram, such a system is likely to have an H_α EW emission of at least ∼1000 Å. Assuming the D-type Sb classification is a reasonable classification, this would be in line with why our LS periodogram attempts were unable to recover any meaningful period constraints from the relatively short baseline of such unique systems. We conclude that while ZTF18aaypgug is not our targeted main-sequence dipper candidate, we encourage follow-up and source characterization.

6 Discussion

6.1 Classification Scenarios

In the following sections, we examine potential classification scenarios for our identified population on a case-by-case basis, considering common distinguishing characteristics and underlying physical mechanisms.

Eclipsing Binaries

In this section, we examine the possibility that some fraction of our light curve sample may be canonical eclipsing binaries (EB) as potential sources of contamination. Stellar multiplicity is ubiquitous across both low- and high-mass stars, with studies incorporating theory and observations suggesting a multiplicity fraction of FGK stars in the order of 40–50% (Offner et al., 2023). The wide-binary fraction for FGK stars within 100 pc is on the order of 10% (Gaia Collaboration et al., 2021b).

Our light curve analysis revealed multiple lines of evidence against EB contamination in our main-sequence sample. Most compelling are the distinctive morphological characteristics of our light curves. First, in Section 5.2, we demonstrated that many of our light curves show asymmetric single erratic dimming profiles rather than multiple symmetric occultations expected from EBs. Second, highlighted in Section 5.5, we do not find any periodic light curves in our sample, except for one. While ZTF's sparse sampling could potentially mask some features, the consistent pattern of asymmetric and non-periodic dimmings argues against the case of canonical EB.

Next, the timescale of our main-sequence dippers is not compatible with those of typical stellar EBs. To estimate the expected eclipse durations, we assume simple Keplerian circular orbits. While we acknowledge that eccentricity tends to increase with orbital period (Tokovinin & Kiyaeva, 2016), which could lead to longer eclipses at periastron, the overall duration of an eclipse is still constrained by the companion's transverse velocity and primary/secondary radii, given by:

$$t_{dip} = \frac{2(R_1 + R_2)}{v}, \tag{2.6}$$

where R_1 and R_2 are the radii of the primary and companion, and v is the transverse velocity of the companion across the stellar equator.

As shown in Figure 2.6, the median timescales of our events range from weeks to months. Assuming a solar-mass primary star with a negligible mass companion in a circular orbit (semi-major axis ∼1.8 AU) and a single eclipse within a ∼2.5-year ZTF baseline (roughly half of the full ZTF light curve duration), we would expect an eclipse duration of only ∼1.5 days (tangential velocity of 21 km/s).On the contrary, producing eclipses lasting weeks to months, comparable to the observed timescales of our main-sequence dippers, would require semimajor axes to be between 10 and 10,000 AU. The probability of a transit occurring for such a wide binary is given by:

$$P_{transit} \propto \frac{(R_1 + R_2)(1 + e)}{\alpha(1 - e^2)}, \tag{2.7}$$

where e is the eccentricity, α is the semi-major axis, and R_1, R_2 are the radii of the stars. For wide binaries at separations of 10–10,000 AU, the transit probability is on the order of 10^{-4} to 10^{-7} assuming an eclipse between a solar and sub-solar companion with circular orbit (e=0), making such chance alignments remarkably rare. While these low transit probabilities could account for the rarity of such events, they fail to explain the complexity of the observed transit shapes. One possible alternative is the simultaneous transit of multiple stars, but the probability of such a rare alignment is increasingly improbable.

If such wide binaries were the cause of our observed dips, we would expect a considerable fraction of our sample within 1 kpc to be resolved as binaries with separations greater than 1000 AU due to *Gaia*'s superb ∼1-arcsecond angular resolution, though, at epochs of transit, the semimajor axis might not be the largest depending on if this is a bounded orbit. Given the observed light curve morphologies and timescales, it is more plausible that some sources are wide binaries with companions enshrouded by circumstellar material, as we will discuss in later sections. Furthermore, a search through known ZTF eclipsing binary catalogs yielded no matches to our sources. We therefore conclude that the vast majority of our main-sequence dipper candidates are unlikely to be due to canonical eclipsing binary systems.

Cataclysmic Variables

Cataclysmic Variables (CVs) exhibit complex photometric variability across timescales ranging from minutes to years, with these binary systems consisting of a primary white dwarf accreting material from a secondary high-mass donor star (Robinson, 1976). The observed variability manifests through multiple mechanisms: periodic optical variations on hour-long timescales corresponding to orbital dynamics, and state transitions in the accretion disk producing high-energy outbursts. Nova-like variables display stochastic large-amplitude variability driven by fluctuations in mass-transfer rates, transitioning between high and low accretion states on year-long timescales (Scaringi et al., 2017), while certain geometric configurations where the accretion disk occults the donor star can generate large-amplitude dips over hours (Campbell et al., 2015).

As discussed in Section 5.7, 33 stars were identified in the IPHAS catalog, one of which showed a clear excess in Hα, while the remaining had Hα and broad colors consistent with the MS locus. Many subtypes of CVs display Hα emission, which can often be found in photometric Hα surveys (Witham et al., 2006) that have equivalent widths upward of 10 Å. Though this eliminates the interpretation for the scenario of those 32 stars, the remaining MS stars could be potential candidates since we do not have Hα constraints.

The broadband optical photometry collated in this study also disfavors the scenario of a CV interpretation. By taking a catalog of known CVs from Abrahams et al. (2022), we crossmatched all sources to the PS1 catalog to obtain broadband *grizy* photometry. We then used `isochrones`[11] to simulate the stellar FGKM main-sequence locus for stars between ages of 7-10 Gyr, assuming a uniform metallicity prior and maximum distance of 10 kpc. We used

[11] https://isochrones.readthedocs.io/en/latest

a Gaussian Kernel Density Estimator (KDE), assuming an adaptive bandwidth using the Silverman approximation (Silverman, 1986), to model the shape of the stellar locus. To statistically validate if any given main-sequence dipper color locus is consistent with either the CV or main-sequence locus, we implemented Bayes' theorem:

$$P(Class|X) = \frac{P(X|Class)P(Class)}{P(X)}, \tag{2.8}$$

where the class is either a main-sequence or cataclysmic variable. The evidence term can be written analytically, assuming that the product of the prior and the likelihood function over all alternative hypotheses:

$$P(X) = \sum P(H_i)P(X|H_i) \tag{2.9}$$

For each of our candidate stars, using its corresponding PS1 *grizy* photometry, we computed the posterior distribution that it belongs to either the main-sequence or CV, assuming a uniform prior. In all 81 cases, no candidate exceeds a 50% probability of belonging to the CV population. Based on the 4-dimensional color-color locus of the PS1 photometry, we have considered this study. We conclude that all of our sources are consistent with the stellar main-sequence locus and are likely not CVs. In addition, the lack of any detections from the Galaxy Evolution Explorer (GALEX; Martin et al. (2005a)) prevents firm conclusions about the excess UV emission. However, all our candidates have redder and brighter Gaia colors compared to canonical CV's, which typically lie between the main-sequence and the white dwarf cooling sequence in the Gaia CMD (Rodriguez et al., 2025). In future follow-up studies, if any undetected CV did not meet our search criteria, low to medium-resolution spectroscopy can easily reveal telltale spectroscopic features of emission lines that could test our hypothesis and rule out with higher fidelity.

Starspots

Low-mass cool stars with convective envelopes exhibit dark regions where the local magnetic field suppresses convection, forming starspots that can cover a significant fraction of the stellar surface and yield a few percent change in flux (Strassmeier (2009), and references therein). Pre-Main-Sequence (PMS) stars are characterized by rapid rotation and strong surface magnetic activity, leading to heightened chromospheric emission (Toriumi & Wang, 2019). We explored whether starspot activity could explain the observed variability in our main-sequence dipper sample and found multiple inconsistencies that argue against this interpretation. While the timescales of our observed dimming events (weeks to months) overlap with typical starspot lifetimes (e.g. Giles et al., 2017), the morphology of the light curves appears highly incompatible with rotational modulation of spot groups. The amplitude of the observed dimming events substantially exceeds expectations for starspot-induced variability. Typical starspot contrasts produce photometric variations of only a few percent, well below our observed dimming depths and below the ZTF detection threshold. The light curve amplitudes, morphologies, and timescales do not well match the interpretation of starspots.

Intervening ISM

It has been proposed that a significant fraction of Galactic baryonic dark matter may reside in cold, dense clouds of gas and dust (De Paolis et al., 1995; Gerhard & Silk, 1996). Observations from the Submillimetre Common-User Bolometer Array (SCUBA) have identified cool, compact clumps with temperatures of ∼10K, suggesting such cold structures could be Galactic in origin (Lawrence, 2001). Kerins et al. (2002) proposed that these dense clouds could produce transient dimming events of background stars with timescales ranging from 10 to 1000 days, and extinction levels reaching 5 magnitudes, leading to sharp cutoffs in stellar light curves. These hypothesized clumps bear similarities to one class of solutions proposed by Wright & Sigurdsson (2016) for the dimming events of the Boyajian star, in which localized interstellar dust structures on sub-AU scales in the Interstellar Medium (ISM) obscure a background star.

A full investigation of this scenario is beyond the scope of this study for several reasons. First, testing the hypothesis that dark interstellar clouds occult our sources requires precise knowledge of the full kinematics for our stars, which is currently unavailable. This explanation would likely only be viable for sources exhibiting a single discrete dimming event, as multiple photometric dips make the scenario highly improbable. Drake & Cook (2003) conducted a search for such events across 4.8 million stars and found no viable candidates with masses in the range of within the 10^{-4}–10^{-2} $M_\odot$ under any extinction exceeding $A_V > 0.2$ mag. Our observed rate of main-sequence dippers is therefore inconsistent with the expected event rate for occulting dark clouds, which is predicted to be >100 events per year per million stars (Kerins et al., 2002). Finally, we find no evidence that neighboring sources exhibit similar photometric dips, though one could argue that intervening material might be highly localized.

Young Stellar Objects

Our main-sequence dipper stars exhibit variability possibly resembling YSO "dipper" stars, which show quasi-periodic or stochastic flux drops lasting days to years. YSO dippers are attributed to dusty disk structures, including wraps, clumps, and accretion streams (Bouvier et al., 2003; Cody et al., 2014b; McGinnis et al., 2015; Morales-Calderón et al., 2011). In the magnetospheric-accretion paradigm, the elevated inner-disk material briefly crosses our line of sight, occulting the stellar photosphere on the timescale of days (Bodman et al., 2017; Hartmann et al., 1994). Beyond short-term events, some YSOs show extreme variability with dips >2 magnitudes over months to years. The AA Tau 2011 dimming episode was attributed to increased circumstellar disk density beyond 7.7 AU (Bouvier et al., 2013). These prolonged dimming episodes typically result from non-axisymmetric density waves and scale height perturbations, possibly induced by planetary-mass companions (Kley & Nelson, 2012; Rodriguez et al., 2017).

As noted in Section 5.1, 75% of our sample exhibits single isolated dimming episodes over the 5.5-year ZTF baseline, unlike typical YSO dippers, which characteristically show quasi-periodic variability with multiple dips (Hillenbrand et al., 2022a). In some rare circumstances, such as the case of EPIC 204376071, a ∼10Myr system in the Upper Scorpius Association (Rappaport et al., 2019), which exhibited an 80% dip that lasted for one day.

Similarly, a handful of main-sequence dipper stars with prolonged dimming deep events ($>$ 100 days) pose a light curve resemblance with AA-Tau analogs. It is conceivable that the remaining 25% of our main-sequence stars with multiple dips could fit with canonical YSO variability. We found that our main-sequence dippers do not share the ZTF $(g-r)$ color properties of YSO studies (Hillenbrand et al., 2022a), which are dominated by extinction and accretion effects. Instead, Figure 2.10 shows that some of these stars become redder during their dips, indicating sub-micron dust.

YSO classification relies on infrared and Hα properties. Classical T-Tauri stars (CTTs) show Hα equivalent widths $>$ 10 Å and strong IR excess from inner disks, whereas weak-line T-Tauri stars (WTTs) have equivalent widths $<$ 10 Å with little excess, indicating WTTs are more evolved (Galli et al., 2015). In Figure 2.18, we show the 2MASS/WISE color-color diagram for our main-sequence dippers and Type I, II, and Transition Disks identified in the Sh2-112 Filamentary Cloud Complex, including their associated photometric boundaries determined by Koenig & Leisawitz (2014). We also overlay the unWISE W_1 Z-score variability at the color-color position of each star, but do not find any obvious trends. The 2MASS-WISE color-color diagram shows that almost all of our main-sequence dipper stars are bluer than the transition region between class II and transitional disks, and the class I disk. Table **??** presents the case of 8 of our main-sequence dippers stars that have been flagged as class II YSO; however, their indicated probability is $\sim$0. The narrow IR occupied region of our main-sequence dippers could be consistent with either the WWT or the main-sequence stellar locus. Similarly, the color-color IR diagram highlighted in Figure 2.19, shows that for the fraction of sources that have been observed by IPHAS, show no signs of Hα excess.

To evaluate the possibility of a disk, in Figure 2.20 we present stellar disk models and compare them to the WISE upper limits. We use the BT-NextGen stellar photospheric model grid (Allard et al., 2012), assuming emission from a Sun-like star. Our model includes an excess disk component with temperature (T_d) and radius (R_d=250 AU) using `Species` (Stolker et al., 2020). By varying disk temperature and stellar distance, we integrated the spectral energy distribution to obtain theoretical W_3 and W_4 bandpasses. In Figure 2.20 we show the color-magnitude diagram of the hypothetical disk excess with varied dust temperatures between 150-800 Kevlin, and distances between 500-2000 pc. Our models predict that the hotter disk $\gtrsim$500 Kelvin at all three distances would most likely preclude being bright enough to be detected with WISE. Based on our models, we find that a 250 AU disk with T_s>500 Kelvin can be eliminated. This can be further argued by the fact that disks of YSO dipper stars near the co-rotational radius of the star are at least $\sim$915 Kelvin (see Table 1 in Bodman et al. (2017)). Out of the 81 candidates, only two sources have a >2 σ W_3 and W_4 detections. Namely, we have identified one of those stars to be, ZTF18actxeox, which exhibits one $\sim$0.23 mag dip and is located near the H-II LBN 140.77-1.42 and W5 and star-forming regions (Deharveng et al., 2012; Karr & Martin, 2003) though its distance seems to be closer $\sim$500 pc compared to the estimated 2kpc predicted distance of these H-II regions and its W_3-W_4 color has been estimated to be 3.8. The other star has been identified as ZTF19abtaugz with W_3-W_4 3.2; however, we did not find any nearby neighboring sources to determine if it is part of any obvious H-II regions.

Under the assumption of circular orbits, depths, duration, and lack of periodicity of the dimming events, the transiting material must be located at large separations from the host

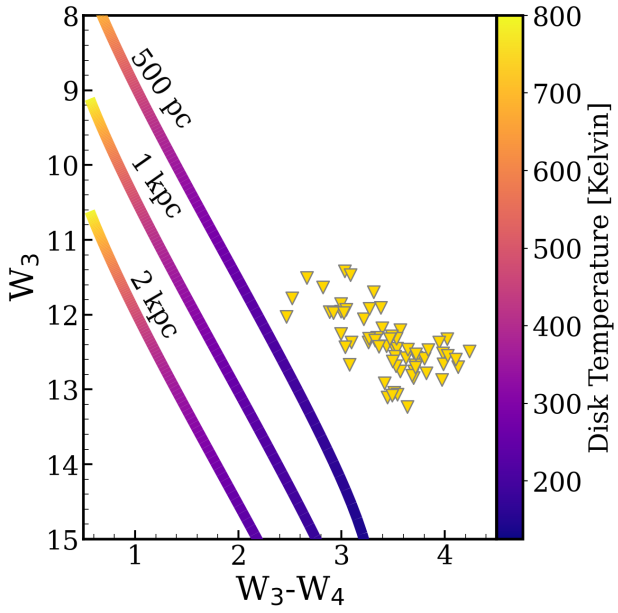


Figure 2.20: WISE color-magnitude diagram displaying the upper limits of our identified main-sequence dipper stars with SNR $<2\sigma$ (gold markers). The lined models represent BT-NextGen SED models, incorporating an additional disk emission component with a radius of 250 AU. The color bar indicates the variation in disk temperature, while the different models are explored across multiple distances.

star, and clump sizes would thus be comparable to the star. However, without deeper IR observations, we cannot rule out that some systems may harbor cool disks responsible for the observed dimmings. Inspection of a low-resolution optical spectrum obtained by the Palomar 200-inch reveals, at least for one of these sources, typical photospheric line FGK absorption lines without the presence of any emission lines, shown in Figure 2.21.

Circumstellar Material

Circumstellar disks evolve from primordial gas-rich protoplanetary disks into dust-dominated debris disks as gas dissipates and planets form (Wyatt, 2008a). Debris disks are continuously replenished by planetesimal collisions, producing dust observable as IR sources and potentially causing optical stochastic dips (Su et al., 2022a; Su et al., 2020). Among older low-mass field main-sequence stars with >1 Gyr, are found with extreme mid-IR excesses, which may result from frequent planetary collisions (Theissen & West, 2017).

The deep and prolonged brightness dips observed in our main-sequence dippers could hint at distant, substantial dust clouds orbiting the star. Assuming this material is bound to the star, we attempt to constrain its semimajor axes. We start with the assumption that the occulting material is completely opaque on a circular equatorial transit, then the fractional depth will be:

$$\max(\tau) \approx \frac{2(R_* + S)}{\Delta t}, \tag{2.10}$$

where τ is the fractional normalized transit depth, Δt is the timescale of the occultation,

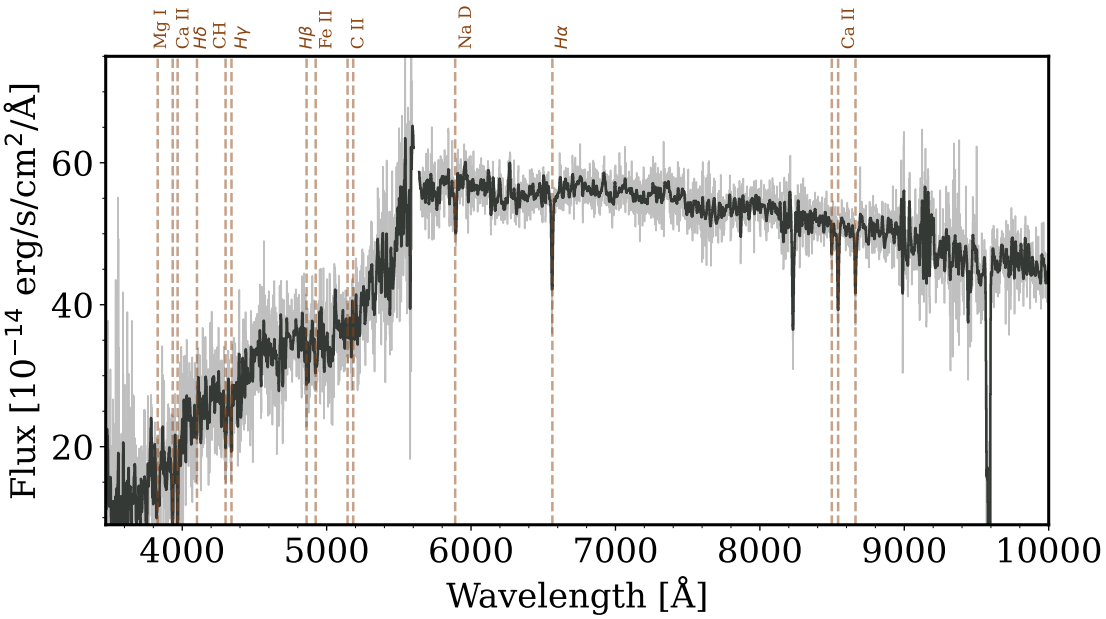


Figure 2.21: Low-resolution optical spectrum of the dipper candidate ZTF18abbtykf, obtained with the Double Beam Spectrograph (DBSP) on the Palomar 200-inch telescope (P200; reduced spectrum provided courtesy of C. Fremling, priv. comm.), The spectrum is used primarily for spectral classification and feature identification; the dashed vertical lines mark the detected absorption features.

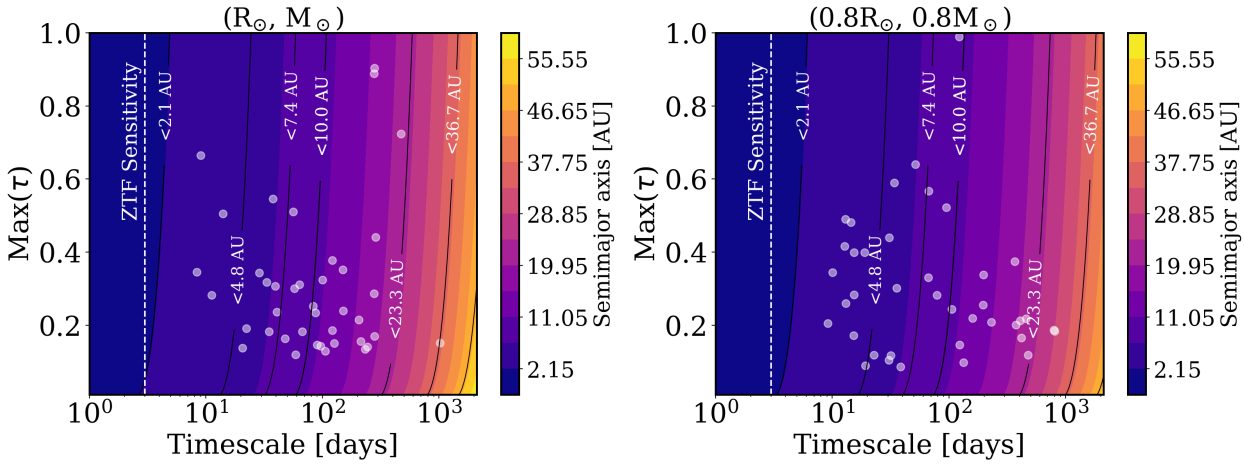


Figure 2.22: Timescale versus maximum transit depth (τ), defined as 1− minimum normalized flux. The background color contours represent the estimated semimajor axis of the occulting bodies, assuming simple Keplerian circular orbits. The sample is divided into two stellar mass bins: stars with $R_\odot \leq 0.8, M_\odot$ (right) and those with $R_\odot \geq 1, M_\odot$ (left). The dashed vertical white line marks the ZTF cadence sensitivity limit. White points indicate the identified dipper candidates.

and the occulting size S. Under this assumption, we can estimate the upper limit to the semi-major axis of such a clump, assuming that it has a mass much less than the primary star and is on a circular orbit with an equatorial transit, then the semimajor axis upper limit will be:

$$a_{\rm circ} \approx M_* \left(\frac{S - R_*}{\Delta t} \right)^{-1/2}, \tag{2.11}$$

where a_{circ} will be the semimajor axis, M_* will be in solar masses. In Figure 2.22, we separated sources near 0.8 solar radii and masses from the `StarHorse 2022` parameters, which include a mass estimate derived from the isochrone fitting. In both mass regime scenarios presented in Figure 2.22 we note that the median is ∼10 AU, which makes sense since the bulk of our dippers have long timescales. We caution against the interpretability of such results and suggest they be understood as upper limits, given competing effects such as observational selection biases (favoring longer-timescale events), circular orbits, and the assumption that the transiting material is optically thick. The presence of transiting dust clumps at large semimajor axes is compelling, as it naturally explains the complex light curve morphology, extended timescales, and lack of infrared excess observed in many main-sequence dippers. This interpretation fits well with the data at our disposal, namely, that collisional evolution of planetesimals at $\geq$ 10 AU can generate long-lived, asymmetric dust structures without necessarily producing detectable near-IR signatures (Wyatt, 2018 and references therein). As suggested in our light curve shape analysis in Section 5.2, many of our discoveries have clear asymmetric shapes that can support the theory of transiting dust structures. It is plausible that structures that persist over Myr timescales provide a mechanism for transient dimming events in systems where circumstellar material periodically obscures the star on such large timescales. We also note in Section 5.4 that at least three of our main-sequence candidates appear to be in open clusters, are appropriate ages where planetesimal collision and formation are expected, and thus can be the origin of the circumstellar material. Interestingly, material near ∼2 AU under Keplerian velocity would have an orbital period on the order of ∼3 years, assuming negligible mass compared to its corresponding solar mass, which would suggest that with the 5.5-year-long ZTF baseline to see at least one more transit of such occulting material.

Disk Occultation

Circumstellar and circumplanetary disks represent important evolutionary stages in stellar and planetary systems, and are considered a ubiquitous feature among young stars (Hughes et al., 2018a). Stellar eclipses by disks provide rare opportunities to study their structure, composition, and dynamics. The transits of such disks around their primary stars are thought to be rare. For example, it has been found that the fraction of detached EBs that host disks in the Large Magellanic Cloud (LMC) is approximately 1/1000, and mostly biased toward young systems (Meng et al., 2014), while Mamajek et al. (2012) estimated that transiting events around a weak-line T-Tauri star with a secondary low mass companion with a disk to be at least 1/100.

In a handful of instances, there have been reports of transiting disks around young stars (Hodapp et al., 2024; Kenworthy & Mamajek, 2015b; Pramono et al., 2024b; Rappaport

et al., 2019) that could be intriguing laboratories for understanding disk structures and perhaps the formation sites of disk formation around stars, exomoon formation (Kenworthy & Mamajek, 2015b) and planetary interior structure (Schlichting & Chang, 2011). However, these confirmed candidates exhibit a diverse range of light curve morphologies, timescales, ages, and color properties that complicate the identification of disk occultation events solely on photometry. Some events show highly symmetric profiles, while others display complex dimming events with multiple minima that can be attributed to disk substructure (Kenworthy & Mamajek, 2015b). Asymmetric light curve ingress and egress profiles have also been reported, potentially resulting from projection effects of inclined disks creating elliptical occulters (van Dam & Kenworthy, 2024b).

As discussed in Section 6.1, due to the large timescales and depths of our observed dips, the occulting material must be at large semimajor axes. If we interpret the results from Figure 2.22 such that many of our systems have large semimajor axes, then the Hill sphere of a 1 $M_\oplus$ orbiting a sun-like star would have a $\sim$21.5 $R_\odot$ hill radius at $\sim$ 5AU, well enough to replicate the occultation size ratios observed in some instances of this sample though at the moment the formation mechanisms of such disks remain unclear.

Detailed radial velocity follow-up is needed to confirm the presence of another body that could contain such rings or disks. Assuming circular orbits, periods must be on the order of >5.5 years to explain the lack of recurring transits.

7 Conclusion

This work presents the results from the first comprehensive search for main-sequence dippers among 63 million FGK main-sequence stars using ZTF Zubercal photometry. Our statistical light curve scoring framework has successfully identified 81 new dipper candidates exhibiting a diverse set of photometric behaviors, some reminiscent of KIC 8462852, others, such as those seen among occultations by disks. Our findings represent a significant expansion of the known population of main-sequence stars experiencing dimming episodes, some of which we hypothesize to be true analogs of Boyajian's star, and analogous stellar systems being occulted by dusty clumps of circumstellar material whose origin remains undetermined. Our conclusions are as follows:

- We developed and implemented a novel statistical light curve scoring framework, enabling efficient analysis of 63 million stellar light curves. Our novel search has revealed 81 new dipper candidates. 76.5% of these candidates have only one dip within the ZTF photometric baseline of 5.5 years, while the remaining have fewer than 23.5% <3 dips. Due to systematic errors present in the ZTF data, visual inspection is still fundamental in identifying bona fide candidates.

- Our sample reveals a large spread in dipper light curve morphologies, with timescales spanning 3 days to $\sim$3 years, and depth amplitudes spanning from 1-99%. We find a marginally statistically significant excess of main-sequence dippers with asymmetric dimmings, with a slight excess with longer egress profiles, which is highly compatible with the scenario of transiting circumstellar dust debris.

- We investigated the ZTF $(g-r)$ color evolution across the light curves of our main-sequence dippers and found a spread of colors, though marginally, with more events that typically reddened by 0.2 mag. Through an analysis of the ZTF-gr CMD, we found their slopes to be below the typical grain sizes of the ISM, possibly pointing to either smaller particle size or different particle properties. We find several statistically significant correlations, such as dip amplitude and $(g-r)$ color, and timescale versus the ZTF-gr CMD slope.

- An analysis of auxiliary infrared and Hα photometric datasets was conducted. The temporal variability of WISE $W_{1,2}$ data did not reveal any variability beyond a $> 3\sigma$ level on a $\sim$4 month timescale. The position of the 2MASS-WISE and IPHAS CMD indicates nominal positions where the stellar main-sequence locus, suggesting that the majority of our stars have no infrared excess within wavelengths $< 4\mu$m, and no Hα emission.

- At least 4 of our main-sequence dipper stars are coincident and members of known open clusters and star-forming regions at ages consistent with planetary impacts. Based on their absolute scale height distributions, we propose that most stars are consistent with a low-alpha Galactic disk, indicating their relative youth.

- Based on the dip timescale, depth, frequency, lack of periodicity, and infrared excess, we propose that the majority of discovered main-sequence dipper stars are the result of transiting circumstellar dust clumps. Under the assumption of circular orbits, the observed timescales suggest typical semimajor axes of $\sim$5-10 AU. If true, such main-sequence dipper stars may be one-of-a-kind laboratories for understanding the origins of circumstellar dust features at large semimajor axes, intimately tied to planet formation and evolution.

Given the discovery of these puzzling dipper stars, it becomes evident that more auxiliary data is necessary to perform a more robust classification and remove any potential outliers. Namely, deeper IR imaging and high-resolution R$\sim$10000 Å spectroscopy will be required to provide more concrete clues to robust classification scenarios. The upcoming Vera C. Rubin Observatory Legacy Survey of Space and Time (LSST; Ivezić et al., 2019) will provide crucial measurements through high-precision photometry across the *ugrizy* bandpasses. Additionally, the Nancy Grace Roman Space Telescope and follow-up observations from *JWST* will extend our sensitivity beyond 1 μm, potentially revealing new populations of such systems and providing critical constraints on the nature of the occulting material.

7.1 Acknowledgments

We thank Ann Marie Cody, Andrew Drake, Tobin Wainer, and Ishan Ghosh-Coutinho for their insightful discussions related to this paper. Additionally, we thank Christoffer Fremling for obtaining spectra for us using the Palomar 200-inch telescope. AT and JRAD acknowledge support from Breakthrough Listen. The Breakthrough Prize Foundation funds the Breakthrough Initiatives, which manage Breakthrough Listen. AT acknowledges the generosity of Eric and Wendy Schmidt, by recommendation of the Schmidt Futures program

through the LSST Discovery Alliance (LSST-DA), is building an LSST Interdisciplinary Network for Collaboration and Computing (LINCC) program. LINCC Frameworks is supported by Schmidt Sciences. A.T. also acknowledges the support from the DiRAC Institute in the Department of Astronomy at the University of Washington. The DiRAC Institute is supported through generous gifts from the Charles and Lisa Simonyi Fund for Arts and Sciences and the Washington Research Foundation. This publication makes use of data products from the Wide-field Infrared Survey Explorer and NASA/IPAC Infrared Science Archive, which is a joint project of the University of California, Los Angeles, and the Jet Propulsion Laboratory/California Institute of Technology, funded by the National Aeronautics and Space Administration.

8 Appendix

Appendix A

Here we present a compilation of all our identified main-sequence dipper ZTF light curves in the g and r bandpasses. The data have been collated from IRSA Data Release 22. Figures 2.24-2.23 show light curves exhibiting a single identified dipping event, while Figures 2.27-2.28 display systems with multiple dimming events detected during our observational baseline. At the top of each light curve, we list the ZTF coordinates for each identified star.

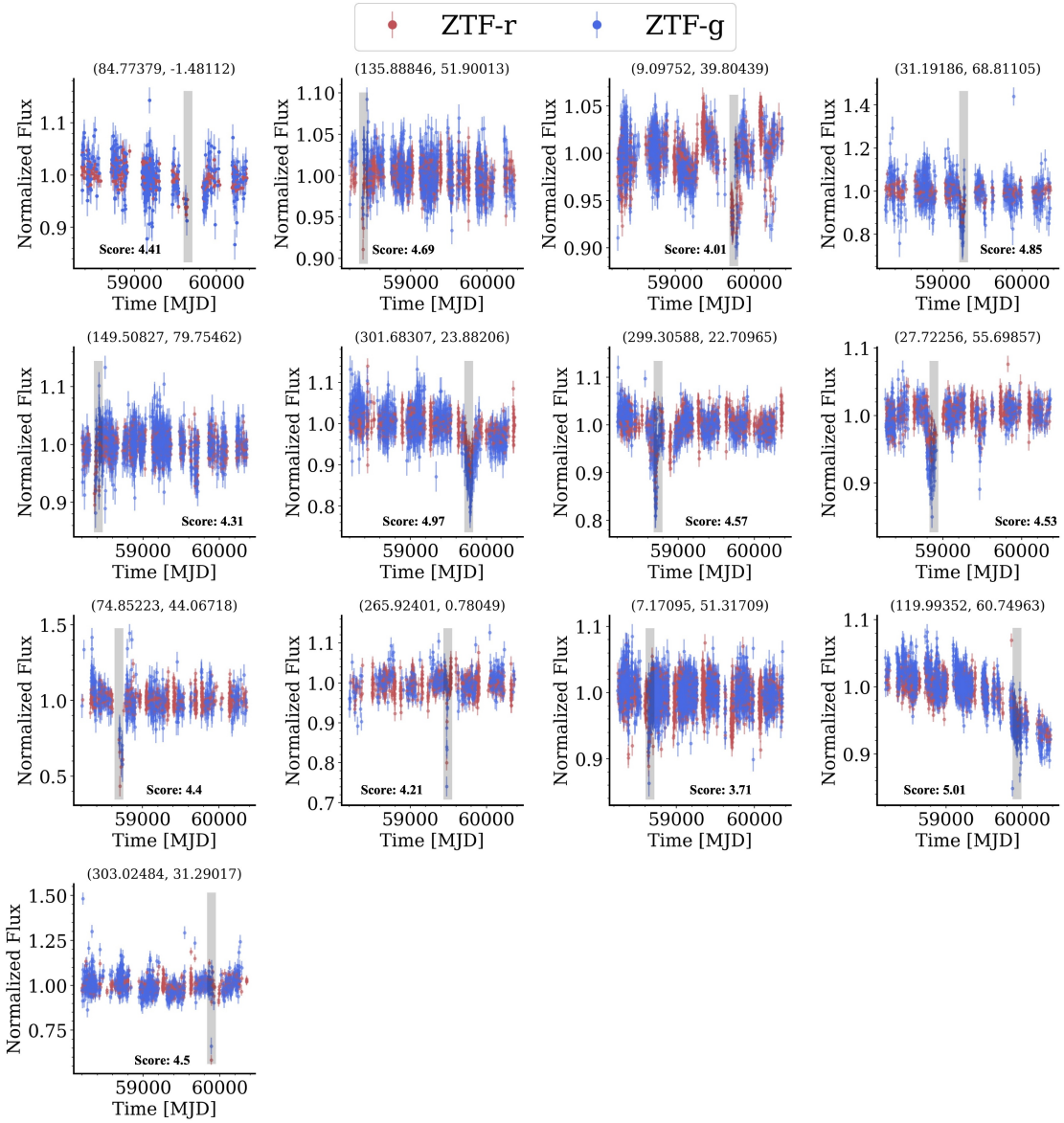


Figure 2.23: Normalized flux ZTF *gr* light curves identified with one unique dip. The black shaded line indicates the time of the photometric dip identified in this study.

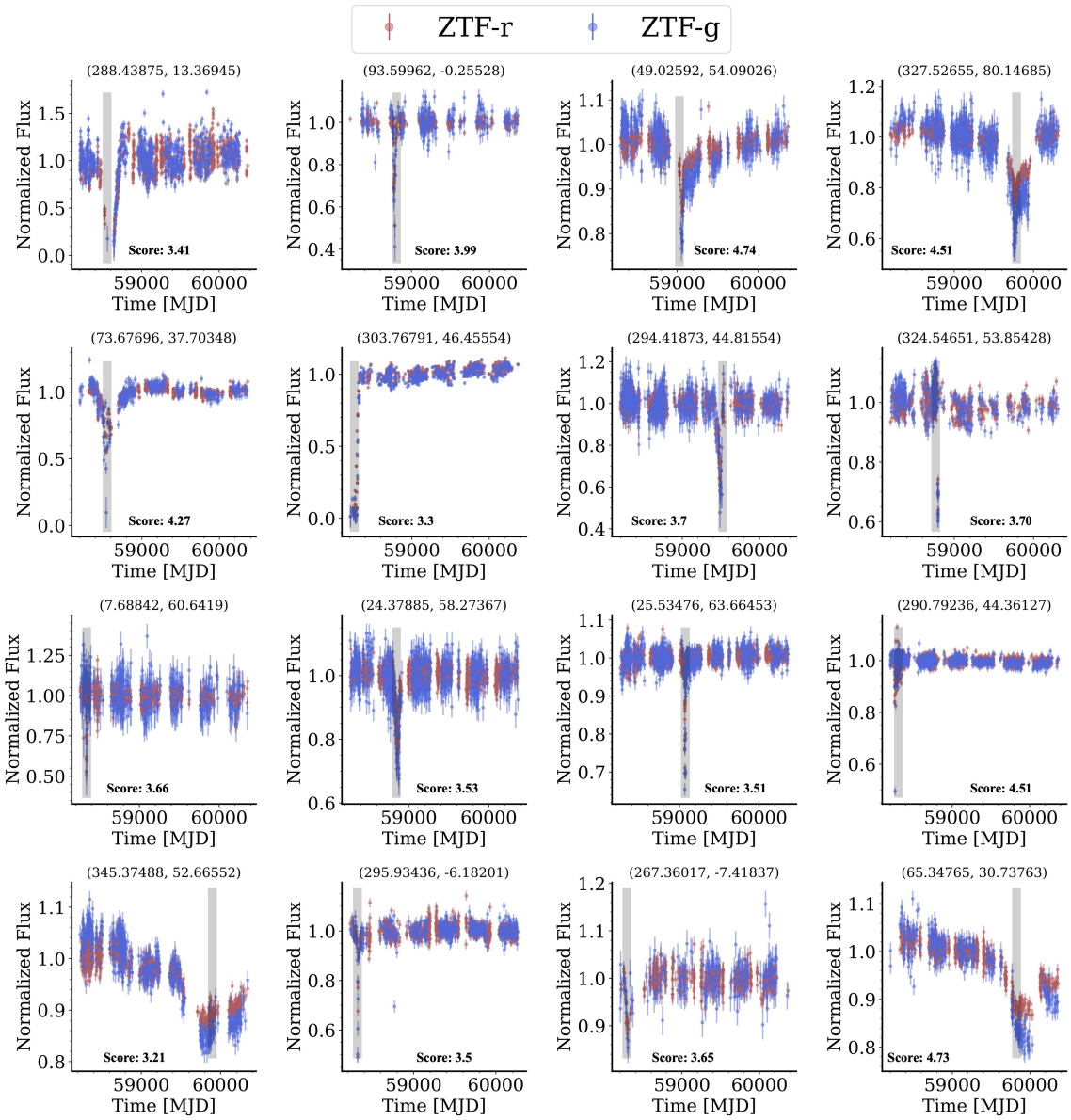


Figure 2.24: Continued, normalized flux ZTF *gr* light curves identified with one unique dip. The black shaded line indicates the time of the photometric dip identified in this study.

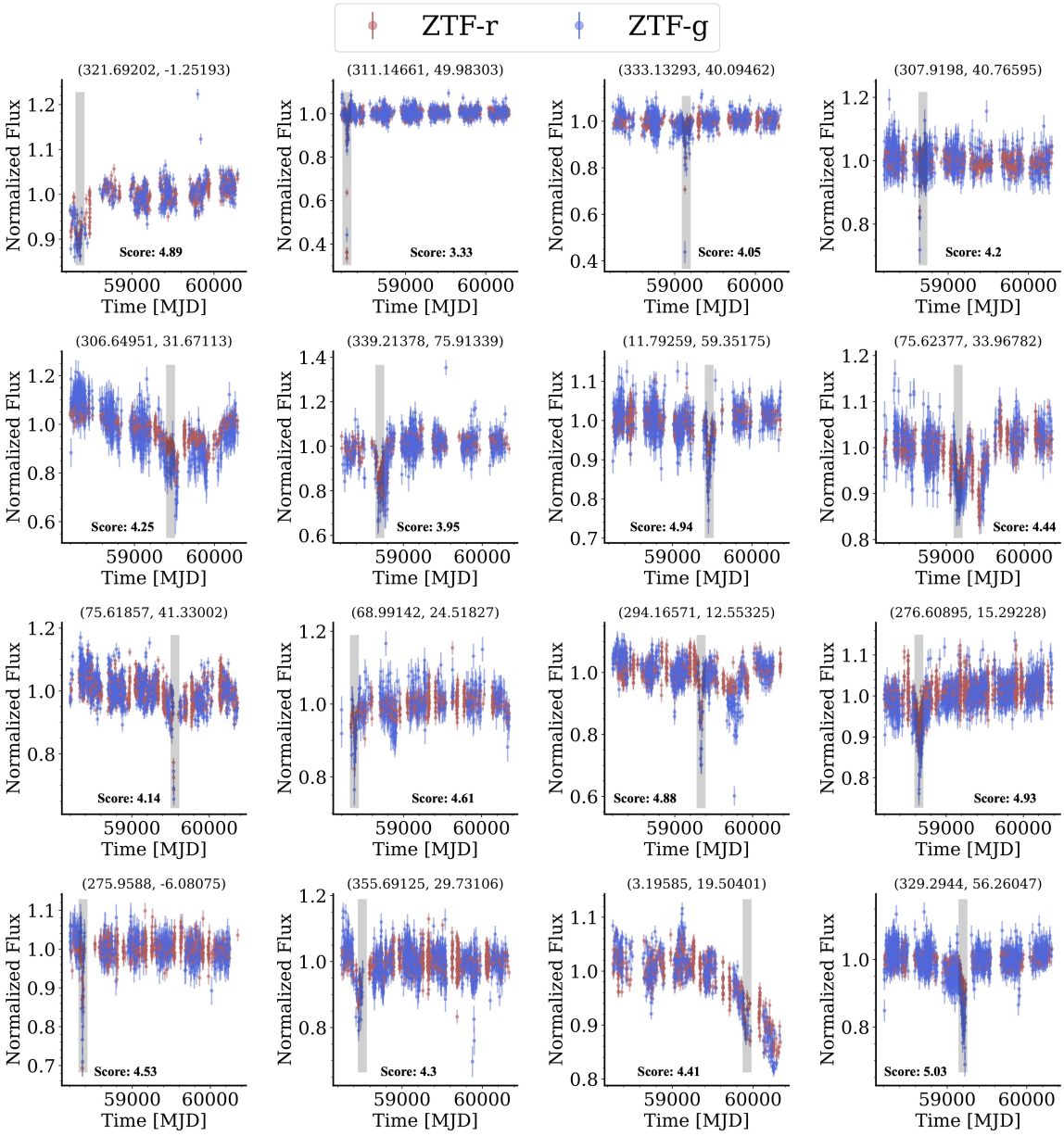


Figure 2.25: Continued, normalized flux ZTF *gr* light curves identified with one unique dip. The black shaded line indicates the time of the photometric dip identified in this study.

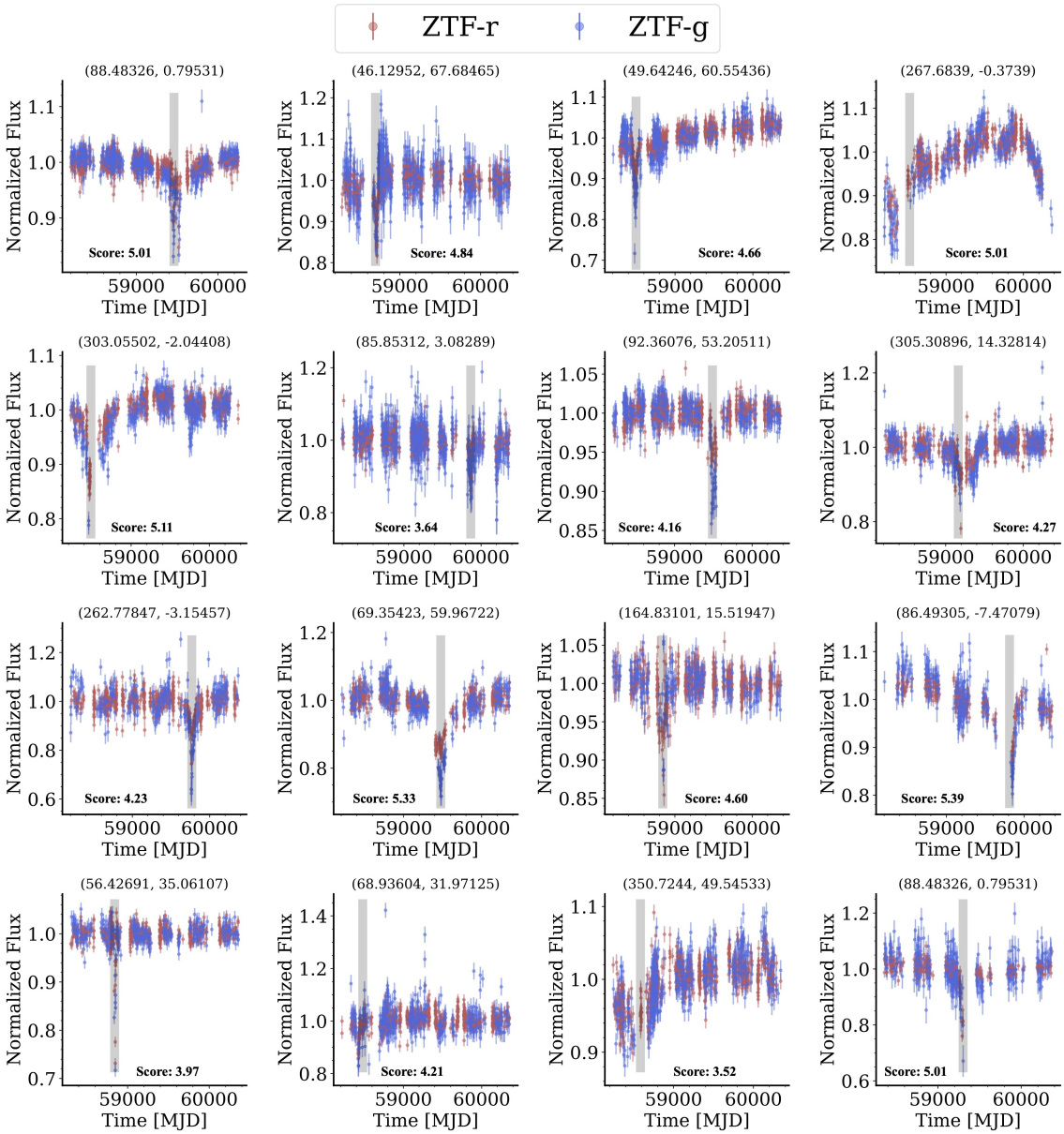


Figure 2.26: Continued, normalized flux ZTF *gr* light curves identified with one unique dip. The black shaded line indicates the time of the photometric dip identified in this study.

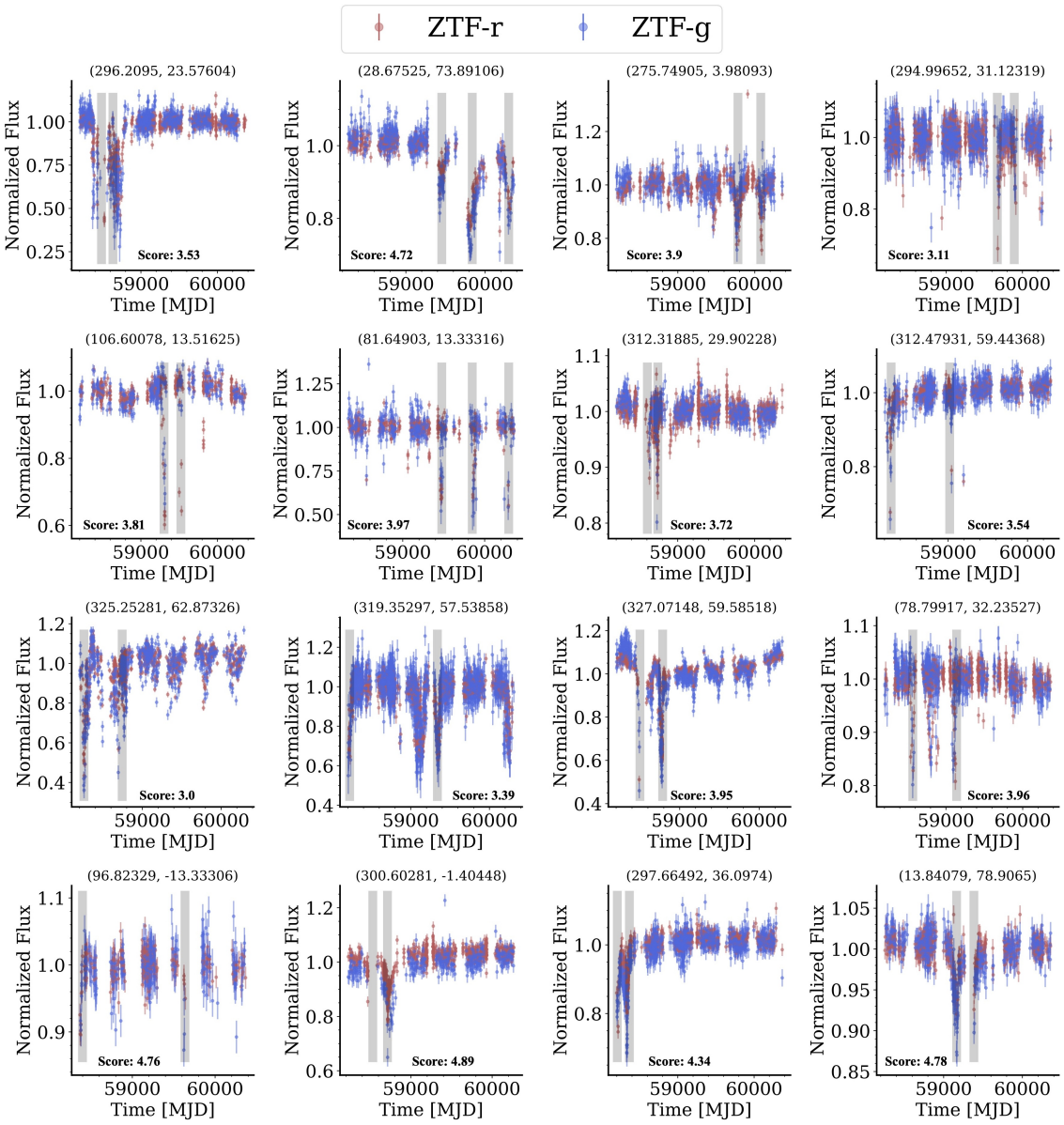


Figure 2.27: Normalized flux ZTF *gr* light curves identified with multiple dips. The black shaded line indicates the time of the photometric dip identified in this study.

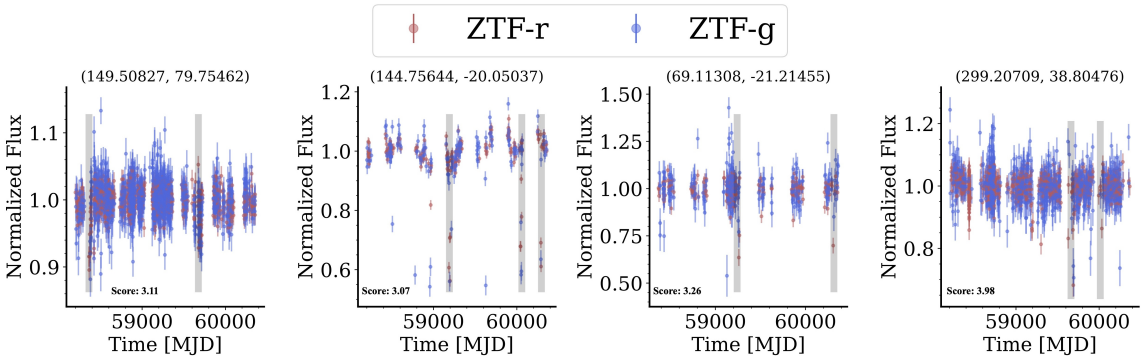


Figure 2.28: Continued, normalized flux ZTF *gr* light curves identified with multiple dips. The black shaded line indicates the time of the photometric dip identified in this study.

Appendix B

For direct comparison to our final stellar locus selection, in Figure 2.29 we present the Pan-STARRS1 color-color $(r-i)$ versus $(g-r)$ diagram compared to the work of Covey et al. (2007) and Table 2.2 with our color-color stellar locus values. Since the original color values of Covey et al. (2007) were reported in the SDSS filters, we applied the appropriate photometric corrections to convert them to the PS1 system (Tonry et al., 2012).

$(r-i)_{PS1}$	$(g-r)_{PS1}$
-0.03	0.10
0.07	0.25
0.14	0.39
0.21	0.53
0.30	0.68
0.39	0.84
0.48	0.99
0.56	1.11
0.64	1.16
0.72	1.18
0.81	1.18

Table 2.2: Pan-STARRS1 color-color locus presented in this work.

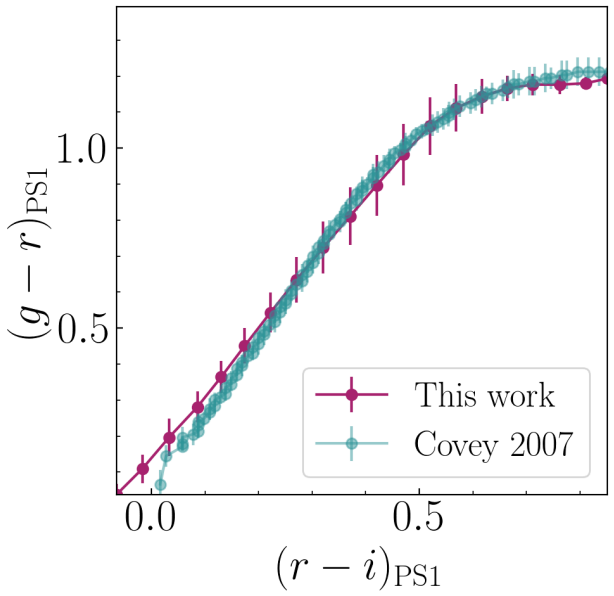


Figure 2.29: Comparison of the Pan-STARRS1 color-color diagram between this work and Covey et al. (2007).

Appendix C

We conduct a 1-arcsecond cone search in VizieR around every main-sequence dipper candidate in search of potential classification of contaminating sources. Table **??** presents all objects returned that have been potentially flagged to belong to another variable star classification (e.g., YSO, AGN, RR Lyrae, BYDRa) or belong to a star-forming and open cluster. For each identification, we provide a brief comment on the classification of the source. We note that these sources remained in the working sample, but we mark them here for cautious interpretation of true main-sequence dippers.

Aside 8.1: A brief aside

Something you'd like to talk about but not in the main text Lorem ipsum dolor sit amet, consectetuer adipiscing elit. Ut purus elit, vestibulum ut, placerat ac, adipiscing vitae, felis. Curabitur dictum gravida mauris. Nam arcu libero, nonummy eget, consectetuer id, vulputate a, magna. Donec vehicula augue eu neque. Pellentesque habitant morbi tristique senectus et netus et malesuada fames ac turpis egestas. Mauris ut leo. Cras viverra metus rhoncus sem. Nulla et lectus vestibulum urna fringilla ultrices. Phasellus eu tellus sit amet tortor gravida placerat. Integer sapien est, iaculis in, pretium quis, viverra ac, nunc. Praesent eget sem vel leo ultrices bibendum. Aenean faucibus. Morbi dolor nulla, malesuada eu, pulvinar at, mollis ac, nulla. Curabitur auctor semper nulla. Donec varius orci eget risus. Duis nibh mi, congue eu, accumsan eleifend, sagittis quis, diam. Duis eget orci sit amet orci dignissim rutrum.

RA (deg)	Dec (deg)	Reference	Comments
288.43875	+13.36945	(Gómez-Muñoz et al., 2023)	Possible planetary nebulae. Marked with Hα excess emission discussed in Section 5.7.
49.02592	+54.09026	(Wilson et al., 2023)	Flagged as potential class II YSO. However, the posterior probability of belonging to this class is very close to 0.
327.52655	+80.14685	(Gorbikov & Brosch, 2014)	Flagged as potential AGN, though Gaia astrometry indicates the source is stellar.
73.67696	+37.70348	(Kos, 2024; Wilson et al., 2023)	Flagged as potential class II YSO (posterior probability $\simeq$ 0). Possibly associated with the open cluster COIN-Gaia-15 with 12% membership probability.
303.76791	+46.45554	(Green et al., 2023)	Flagged as potential ellipsoidal binary candidate with a 3.07 day period; quality score is zero.
324.54651	+53.85428	(Chan et al., 2022)	Flagged as BYDra like variable with score 0.3.
7.68842	+60.64190	(van Groeningen et al., 2023)	Flagged as member of open cluster NGC 129 with 0.1 membership probability.
24.37885	+58.27367	(Vioque et al., 2020)	Flagged as Herbig Ae/Be star with 0.96 probability of belonging to another class.
25.53476	+63.66453	(Wilson et al., 2023)	Flagged as potential class II YSO; posterior probability $\simeq$ 0.

Table 2.3: Summary table of potential contaminant candidates (1/3).

RA (deg)	Dec (deg)	Reference	Comments
319.35297	+57.53858	(Sesar et al., 2017)	Flagged as potential RR Lyrae class with ∼0 RRab/RRc classification score.
321.69202	−01.25193	(Gavras et al., 2023; Watkins et al., 2009)	Flagged as BY Dra like variable and RR Lyrae with 'no valid period/score.
333.13293	+40.09462	(Watson et al., 2006)	Flagged as rotational variable in the Variable Star IndeX.
307.91980	+40.76595	(Gupta et al., 2021; Wilson et al., 2023)	Near the Cygnus OB2 complex (Subaru/HSC). Also flagged as potential class II YSO (posterior probability $\simeq$ 0).
306.64951	+31.67113	(Wilson et al., 2023)	Flagged as potential class II YSO; posterior probability $\simeq$ 0.
11.79259	+59.35175	(Wilson et al., 2023)	Flagged as potential class II YSO; posterior probability $\simeq$ 0.
75.61857	+41.33002	(Chan et al., 2022)	Flagged as BYDra like variable with score 0.2.
78.79917	+32.23527	(Wilson et al., 2023)	Flagged as potential class II YSO; posterior probability $\simeq$ 0.
3.19585	+19.50401	(Qian et al., 2019; Zhang et al., 2024)	Spectroscopic binary and variable star with 22 km s^{-1} RV amplitude; no validity score. Possible active star (reported S–index).

Table 2.4: Summary table of potential contaminant candidates (2/3).

RA (deg)	Dec (deg)	Reference	Comments
329.29440	+56.26047	(Kos, 2024)	Possibly associated with open cluster UBC 155 (16% membership probability).
49.64246	+60.55436	(Vioque et al., 2020)	Flagged as Herbig Ae/Be star with 0.97 probability of belonging to another class.
267.68390	−00.37390	(Watson et al., 2006)	Flagged as rotational variable in the Variable Star IndeX.
13.84079	+78.90650	(Johnson et al., 2023)	Reported counts from LOFAR.
350.72440	+49.54533	(Petrosky et al., 2021)	Listed in variable/periodic and contact-binary catalogues, but internal flags indicate it is neither EB nor variable.
43.15890	+72.34585	(Johnson et al., 2023)	Reported counts from LOFAR.
84.77379	−01.48112	(Dias et al., 2014)	Flagged with 89% probability of membership in the Collinder 70 open cluster.
69.11308	−21.21455	(Stringer et al., 2019)	Flagged as RR Lyrae with RRab probability 0.0001.
303.02484	+31.29017	(Wilson et al., 2023)	Flagged as potential class II YSO; posterior probability $\simeq 0$.

Table 2.5: Summary table of potential contaminant candidates (3/3).

Gaia DR3 ID	R.A	Dec	G_0 [12] (mag)	G_{BP} - G_{RP} [13] (mag)	Distance[14] (kpc)	t_{dip} [15] (MJD)	N_{Dips}
4319330107178019200	288.43875	13.36944	4.288	0.678	2.091	58643.299	1.0
3121854222422204544	93.59962	-0.25528	7.026	1.243	0.86	58787.517	1.0
446400591305341056	49.02593	54.09025	3.696	0.781	1.104	59055.467	1.0
2285460370033812864	327.52656	80.14685	5.313	1.01	1.274	59779.271	1.0
198430753251200128	73.67696	37.70347	4.931	0.838	1.084	58540.282	1.0
2082534881979041280	303.76791	46.45553	5.867	1.101	0.33	58252.489	1.0
2079894366138598656	294.41874	44.81552	4.957	0.79	4.301	59484.241	1.0
2174227726473890176	324.54651	53.85427	5.047	0.865	0.899	58799.222	1.0
428654920313727744	7.68843	60.64189	5.561	0.929	1.851	58333.34	1.0
508972801614364032	24.37886	58.27367	4.658	0.824	1.793	58877.125	1.0
512103523536262144	25.53477	63.66452	4.328	0.844	0.643	59065.39	1.0
2126217688671428864	290.79236	44.36126	4.734	0.796	0.987	58257.476	1.0
1989462803234296832	345.37488	52.66552	6.91	1.361	0.496	59816.387	1.0
4208785414254570368	295.93436	-6.18203	4.582	0.791	1.673	58318.334	1.0
4165810383809607808	267.36017	-7.41839	3.868	0.765	1.473	58291.272	1.0
166212073259272832	65.34766	30.73762	5.994	1.083	0.432	59922.367	1.0
2686018434626245888	321.69203	-1.25194	5.269	1.064	1.145	58326.377	1.0
2168271294020636800	311.1466	49.98304	4.31	0.806	1.581	58271.453	1.0
1956436050910998784	333.13294	40.09462	6.713	1.303	0.878	59126.323	1.0
2067746141339717120	307.91981	40.76595	3.941	0.701	1.295	58646.477	1.0
1862110906882967552	306.6495	31.67113	6.091	1.11	1.069	59525.134	1.0
2279847496317770240	339.21377	75.91337	5.282	0.911	2.673	58771.335	1.0
425286325927143936	11.79256	59.35174	4.606	0.775	1.43	59453.343	1.0
184965210441328896	75.62383	33.96783	4.972	0.89	1.414	59426.487	1.0
200936780769225088	75.61856	41.33001	6.059	1.016	0.832	59542.202	1.0
...	...	...	...	...	...	...	...
1132318104107576064	149.50826	79.7546	6.564	1.218	0.865	58364.507	2.0
5677433705699331328	144.75644	-20.05037	5.684	0.935	1.231	59198.439	2.0
4898717140928169344	69.11309	-21.21456	6.502	1.067	2.094	59260.149	2.0
2072562856964901760	299.20706	38.80473	5.698	1.002	2.231	59689.447	2.0

Table 2.6: Main sequence dipper candidates including their observed properties. This table will be provided in its entirety in machine-readable form in the online journal.

CHAPTER 3

DISKS ECLIPSES ACROSS STELLAR AGE

1 Gaia17bpp: A Giant Star with the Deepest and Longest Known Dimming Event 71
2 Introduction 71
3 Data 72
4 Primary Star 78
5 Dimming Event Properties 82
6 Discussion 84
7 Conclusion 90
8 Acknowledgments 92

1 Gaia17bpp: A Giant Star with the Deepest and Longest Known Dimming Event

The original has been accepted to the ApJ. I acknowledge the contributions from my collaborators, James Davenport, Eric Bellm, and Yankun (David) Wang.

2 Introduction

The long-term photometric monitoring of the sky is steadily increasing the discovery of remarkable dimming events on the timescale of decades. Amongst slowly evolving stellar variables, an emerging population of photometrically deep, long-duration, and long-period anomalous binary systems with the secondary star being enveloped by a large disk that calls for more attention (Stencel, 2016). At the turn of the century, the enigmatic star Epsilon Aurigae (ϵ-Aur), which exhibits a single flat-bottomed, $\sim$2 year long dimming event, challenged our understanding of binary stars (Carroll et al., 1991). Today, more than a few decades later, ϵ-Aur has been understood to be a low-mass F0 supergiant star surrounded by a young B5V-type star companion with an extended cool disk with an orbital period of 27 years. Both spectroscopic and direct interferometric imaging techniques have confirmed the presence of a geometrically thin and optically thick disk that is consistent with debris (Kloppenborg et al., 2010; Stencel et al., 2011). Open questions such as the origins and lifetime of the disk, occurrence rates, and formation channels of such systems remain unexplored. Gibson & Stencel (2018) conducted a theoretical study using MESA modules to explain the evolution of the ϵ-Aur binary system. Their study suggests the formation of the large debris disk found around the secondary star of ϵ-Aur was the product of accretion from two intermediate-mass stars, 9.85 $M_\odot$, and 4.5 $M_\odot$, with an initial orbital period of roughly 100 days, after the primary star had made its first ascent to the post-RGB/pre-AGB phase. As noted, however, their models could not replicate the large orbital period of ϵ-Aur which was likely due to poor constraints on the mass transfer profile.

Prior to this work, TYC 2505-672-1 (Lipunov et al., 2016) previously held the record with the longest duration dimming event and longest orbital period binary. The system consists of an M2-III giant that undergoes a 4.5 magnitude 3.5-year long deep eclipse every 69.1 years (Rodriguez et al., 2016). It is suggested that the companion star was a cool subdwarf-B (sdB) type star that will eventually become a low-mass pre-Helium white dwarf (Pre-He WD), enshrouded by an opaque disk. The origin of the disk, however, remains puzzling since accretion from the primary would be challenging to explain given its large semi-major axis separation (Rodriguez et al., 2016). Additionally, previous searches for Pre-He WD stars have been found in compact binary systems (Maxted et al., 2014; van Roestel et al., 2018), unlike a very long binary such as TYC 2505-672-1. More recently, reminiscent systems such as VVV-WIT-08 (Smith et al., 2021), a K7 giant star that showed a single smooth dimming event have also been thought to be occulted by an optically thick disk. Despite the limited understanding of the occulting disk in the majority of these dimming stars, a significant number of them exhibit similar characteristics. These include an evolved primary star, prolonged periods of single deep dimming events that last for years, large orbital periods,

and the absence of IR excess. Finally, other identified long-period binaries have also claimed the presence of an extended disk around the companion star, such as ASASSN-21co (Rowan et al., 2021) and Eta Gem (Torres & Sakano, 2022) that cause prolonged deep eclipses.

In this study, we report the serendipitous discovery of a new giant dimming star, Gaia17bpp/2MASS J19372316+175902, which now holds the record for the longest and deepest dimming event. We incorporate the use of multi-wavelength light curves and optical spectra of this star to understand the nature of the dimming mechanism. This paper is organized as follows. In Section §3 we discuss the data acquisition from all-sky surveys and spectroscopic follow-up efforts. Section 4 describes the modeling of the spectral energy distribution (SED) of the primary star using multi-band archival photometry. Similarly, in Section 5 we analyze the properties and shapes of the light curves from the optical to infrared wavelengths. We provide an interpretation of the dimming event, fit a monochromatic oblate disk model using IR light curves, and investigate the possible mechanism driving it in Section §6. Finally, in Section §6 we provide our conclusions.

3 Data

In the following section, we describe the data acquisition from multiple public all-sky surveys. All collated time-series photometric measurements have been combined to generate a mosaic light curve of Gaia17bpp spanning from the late 1950s to the present date.

3.1 Gaia

Gaia Photometric Science Alerts

Gaia17bpp was first saved as an alert through the Gaia photometric alert stream (Delgado et al., 2017), and was discovered through a subsequent search for deep and long (>5 years) stellar variability. Gaia has been scanning the night sky since 2014 and has been collecting photometric measurements in the Gaia G bandpass and releasing alerts through the Gaia Photometric Science Alerts (GPSA) described in Hodgkin et al. (2021a). We query the Gaia alert light curves through the Gaia Alert website portal[1] to collect all the available epochal Gaia G, BP, and RP detections. In Figure 3.1 we show the issued alert Gaia G light curve of Gaia17bpp.

We note that the current alert schema does not include photometric uncertainties, however, Hodgkin et al. (2021a) suggests an empirical means of estimating uncertainties as a function of source brightness. We also mined[2] the uncalibrated BP/RP flux spectra following the approach of Hodgkin et al. (2021a). Using the integrated BP/RP spectra as a reasonable estimate of the color evolution in the optical regime. The BP photometry in this case suffers from higher scatter because the baseline BP photometry is close to the limiting magnitude. To examine the difference between the estimated uncalibrated BP and RP photometry we crossmatched all photometric alerts that were also found in the Gaia Data Release 3 (Gaia Collaboration et al., 2022b) and compared the reported BP and RP magnitudes with the

[1] http://gsaweb.ast.cam.ac.uk/alerts/home
[2] https://github.com/AndyTza/GaiaAlertsPy

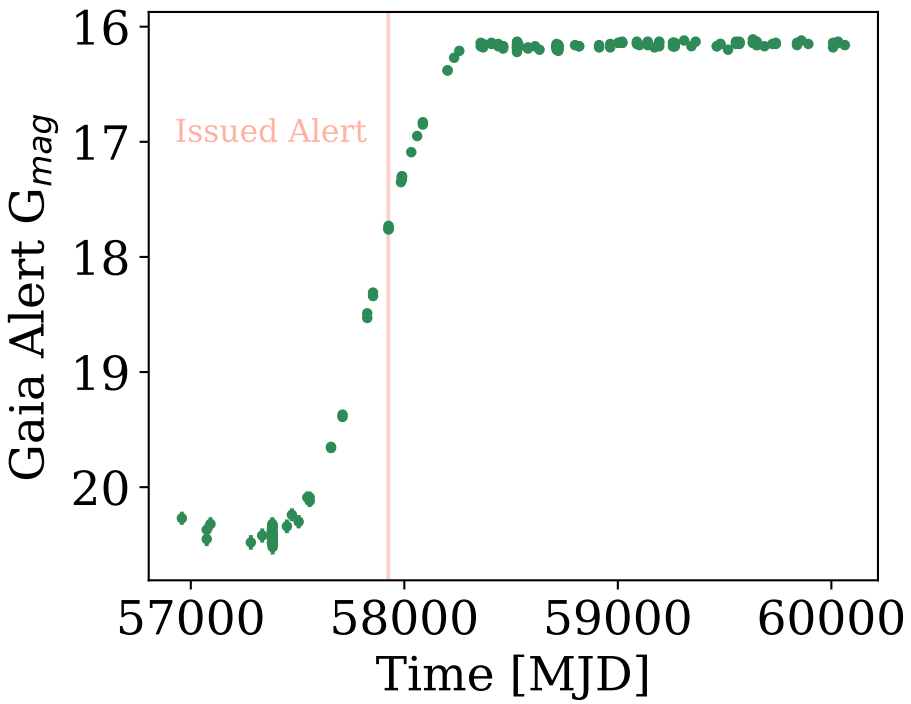


Figure 3.1: Gaia17bpp issued alert light curve in Gaia G. The red line indicates the issued alert epoch.

ones derived from this work. On average, we found a standard deviation of 1.5 mag per magnitude bin. For our reported BP/RP detections, we inflated the photometric errors to capture any excess uncertainty by 1.5 σ_G.

Gaia Data Releases

According to the full photometric history enabled through the GPSA, Gaia17bpp was already at its faintest phase and close to the detection threshold of Gaia when observations began. We identified the system in both Gaia DR2 and DR3 catalogs and investigate the astrometric solutions, specifically the parallax and proper motion vectors. In both data releases the parallax is negative. We suspect this is due to the photometric uncertainty at the bottom of the dimming event, leading to a negative parallax solution (Luri et al., 2018). To obtain distances we rely on the photo-geometric distances derived from the work of Bailer-Jones et al. (2021b) that compensates for negative parallax while enabling a strong prior from the available photometry and Galactic extinction at the line of sight. We adopt the median photo-geometric posterior distribution distance of $8.5^{+2.3}_{-1.6}$ kpc throughout all calculations in this study. In the presence of negative parallaxes, we caution that this estimated distance is mostly prior dominated. In Table 3.1 we highlight all the key parameters reported from Gaia DR3.

Enabled through the distance estimate and extrapolation of BP/RP magnitudes, we placed the location of Gaia17bpp on the observed Hertzsprung-Russell (HR) diagram at the present date is seen in Figure 3.2. We also attempted to track the evolution of Gaia17bpp throughout its dimming phase. We bin both the BP/RP and G band magnitudes by a 450-day running median to capture the overall color and absolute magnitude evolution. In general, we found consistency in the reported photometry with both the official Gaia data releases and the photometric science alerts. However, we noticed that the dimming event was predominantly bluer than the quiescent star. As noted by Riello et al. (2021), faint sources with red colors tend to have overestimated BP fluxes. To mitigate the effects of overestimating the BP flux, we only computed the BP/RP magnitudes based on the epochal spectra after 2016 when the source began re-brightening.

Survey Info	Parameters
Gaia ID	1824311891830344704
Coordinates (α_{J2016}, δ_{J2016})	19h37m23.16s, 17d59m2.90s
Parallax[3] (ω)	-0.18 ± 0.4 mas
Distance[4]	8462 $^{+2317}_{-1567}$ pc
Proper Motion[??] RA ($\mu_{\alpha\cos(\delta)}$)	-0.24 ± 0.4 mas yr^{-1}
Proper Motion[??] DEC (μ_{δ})	-3.04 ± 0.3 mas yr^{-1}

Table 3.1: Astrometric solutions based on the Gaia DR3 catalog for Gaia17bpp.

3.2 WISE

Subsequent investigation revealed that Gaia17bpp was also well monitored by the Wide-field Infrared Survey Explorer (WISE) (Mainzer et al., 2014; Wright et al., 2010b) and NEO-WISE (Mainzer et al., 2011) in the W_1-W_4 filters. To query the WISE and NEOWISE light curves, we use an open-source Python tool, `WISE Light Curves`[5] that automatically

[5]https://github.com/HC-Hwang/wise_light_curves

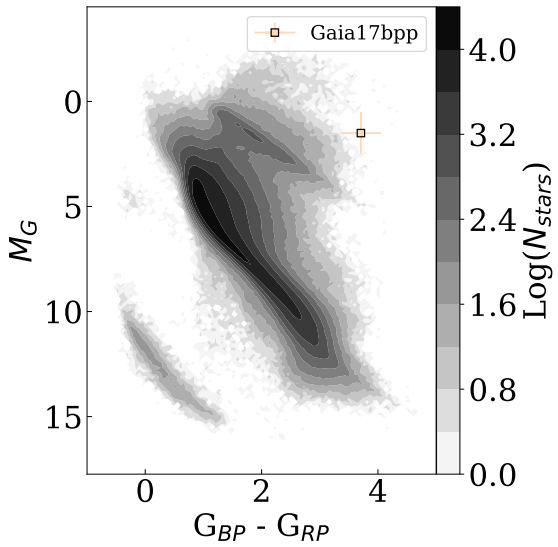


Figure 3.2: Color magnitude diagram (in gray) for the nearby Gaia DR3 sample (Gaia Collaboration et al., 2022b) shaded by the number of stars per bin. We over-plot the position of Gaia17bpp on the CMD from the most recent BP/RP fluxes and Gaia-G estimates using GPSA.

queries NASA/IPAC Infrared Science Archive to compile the epochal photometry from both surveys. We use a five-arcsecond cone search query and identify WISE J193723.16+175903 and confirm it is the identical source to Gaia17bpp. We also searched through the AKARI and Planck observations and found no excess flux within 1 deg^2 in the far-infrared.

3.3 MAST

We also queried the Barbara A. Mikulski Archive for Space Telescopes (MAST) data archive and found a few optical observations from the Panoramic Survey Telescope and Rapid Response System (PS1; **?**), two NUV images from the Galaxy Evolution Explorer (GALEX; Martin et al. (2005b)) in the All-Sky Imaging Survey (AIS), and more recently three Full-Frame Images from the Transiting Exoplanet Survey Satellite (TESS; Ricker et al. (2014)). We generated the PS1 light curves using the Space Telescope Science Institute database to query the PS1 Detection table fields[6] with a crossmatch cone radius of 3 arcseconds. The PS1 detection table contains single-epoch photometry from a single visit exposure that produces the PSF aperture photometry of detected sources. Both GALEX NUV raw count images were visually inspected; however, no coincident source at the location of the Gaia17bpp system was found. We also searched the GALEX GR6/GR7 sources and only found the nearest source to be 1.4 arcminutes away, making it unlikely this is our target. Based on the GALEX AIS 20.5 mag NUV limiting magnitude, we conclude that Gaia17bpp must be fainter.

[6]https://catalogs.mast.stsci.edu/panstarrs/

3.4 Archival Photometry

We obtained archival photometry using the Carlsberg Meridian Catalogue 15 (CMC15; Fabricius (1993)), Initial Gaia Source List (IGSL; Smart & Nicastro (2014)), USNO-B1 all-sky catalog (USNO-B; Monet et al. (2003)), Guide Star Catalog (GSC; Jenkner (1994)), Palomar Observatory Sky Survey (POSS; Reid et al. (1991)), INT Photometric H-Alpha Survey (IPHAS; Walton et al. (2004)), and Digital Access to a Sky Century at Harvard (DASCH; Grindlay (2017)). The DASCH photographic plates while having been scanned had not reported observed magnitudes and extractions at the location of the star. Instead, we ran a source extraction tool to perform aperture photometry at the location of Gaia17bpp using `SEP` (Barbary, 2018). For each 400x400 arcsecond scanned plate from DASCH, we cross-matched each 2σ source detection to the PS1 r-band catalog assuming a limiting magnitude of 16 mag. From each science image, we subtract out the background root mean square variation. After comparing, and extrapolating the zero-point calibration between the PS1 and DASCH images, we summed the fixed aperture at the location of Gaia17bpp to extrapolate a rough estimate of its magnitude and error[7].

Outside of the primary dimming event, Gaia17bpp was also detected in the Zwicky Transient Facility (ZTF) survey (Bellm et al., 2019c) in the *gri* broadband filters. In short, ZTF is a 47 square-degree time-domain survey utilizing the 48-inch Schmidt Palomar telescope (P48) located at the Palomar Observatory. ZTF performs a public component survey that covers the entire northern sky with a 2-day cadence in $g+r$ ($\approx$34% of P48 time) and a 1-day Galactic plane survey in $g+r$ ($\approx$6% of P48 time). A high cadence $\approx$2500 square degrees ($3g+3r$ per night) was conducted for collaboration time, including a 4-day $i-$band survey. On average, the survey covers $\sim$3750 square degrees per hour with a median limiting magnitude of r$\sim$20.6 mag, g$\sim$20.8 mag, and i$\sim$19.9 mag 5σ limiting magnitude in 30-second exposures (Dekany et al., 2020). For in-depth coverage of the scientific goals and survey strategy, we suggest to the reader review Bellm et al. (2019b) and Graham et al. (2019b). No other ZTF or GPSA has been issued within 20 arcseconds of Gaia17bpp. In Figure 3.3, we show the optical to IR mosaic light curve of Gaia17bpp.

3.5 Spectroscopy

Gaia17bpp was observed with the Apache Point Observatory (APO) ARC 3.5-meter telescope using a medium dispersion spectrograph KOSMOS (Stoll et al., 2010) on September 18, 2022. We used the red high slit configuration with wavelength coverage between 6150-9800 Å. Our on-sky time included one thirty-minute exposure with clear sky conditions. Our data reduction followed standard long-slit spectroscopy procedures and reduced the optical spectrum using the open-source Python package `PyKOSMOS` (Davenport, 2021). In Figure 3.4, we show the final reduced optical spectrum of Gaia17bpp without correcting for the telluric absorption features. In the same figure, we also include the NIR spectra of an M0 dwarf and giant, HD 19305 (M0V) and HD 213893 (M0IIIb) standards (Rayner et al., 2009). Upon inspecting the optical spectrum of Gaia17bpp, we do not find any immediate anomalous spectroscopic features. Generally, we identified several absorption lines such as a

[7]Given the distance, proper motion, and coordinates obtained from Gaia DR3 during the J2016.0 epoch, we estimate the change in position due to proper motion to be approximately 0.2 arcseconds.

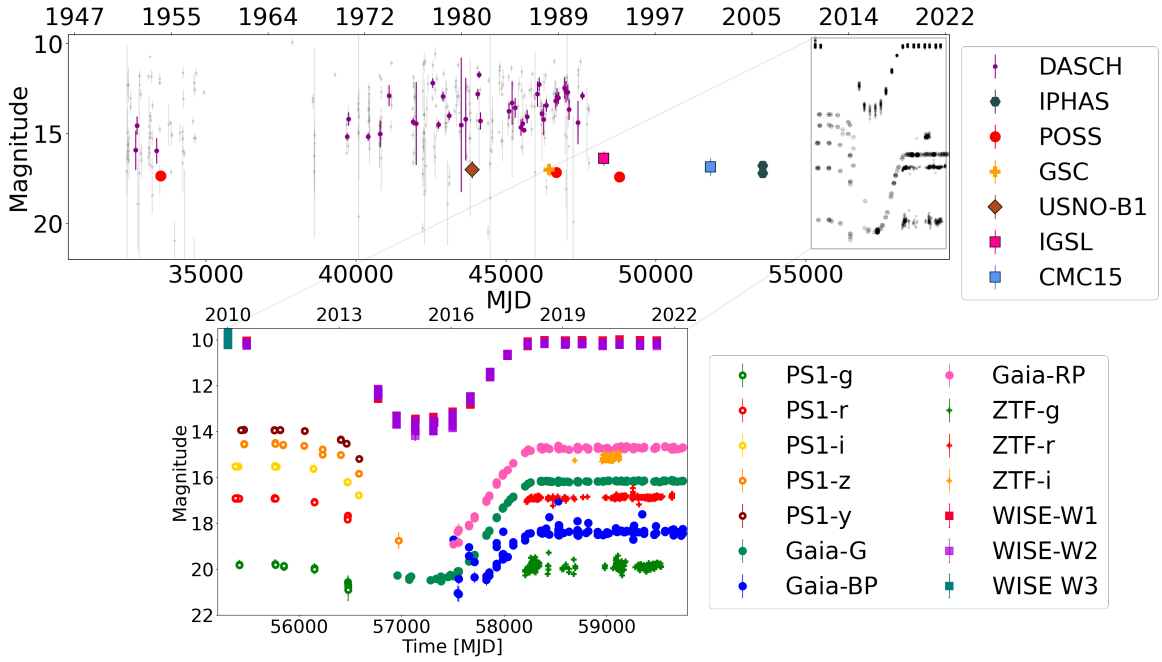


Figure 3.3: Historical optical-NIR light curve of Gaia17bpp. We correct the $PS1_r$ and $PS1_g$ to match the average magnitude baseline of the ZTF light curves. This data will be provided in its entirety in machine-readable form in the online journal.

prominent Ca II triplet at $\lambda\lambda$8498, 8542, and 8662 Å, and clear 7050Å TiO bands, including other molecular lines near $\lambda\lambda$8160Å. We did not identify other significant narrow emission lines that appear in the spectrum, except for a very weak H_α emission line. The absence of the Calcium Hydride (CaH_2) $\lambda\lambda$ 6382/6830Å, Na I doublet 8183/8195Å, and the weak K I 7665/7699Å lines indicate the presence of an evolved giant star (Allers et al., 2007; Stephenson, 1986). The identified spectroscopic features are generally consistent with an ordinary late-type cool K-M class type star. In Section 4 we discuss in depth how the interpretation of such absorption lines is consistent with the classification of an RGB star as the primary source. The collected spectrum is available for further inspection on the Transient Naming Server (TNS) under the source name AT2017exj[8].

3.6 Follow-up Photometry

On May 7, 2023, we performed follow-up photometry on Gaia17bpp with the APO 3.5-meter Astrophysical Research Consortium Telescope Imaging Camera (ARCTIC) (Huehnerhoff et al., 2016) using the SDSS-u filter. The seeing was approximately 1-arcsecond throughout the entire night. We note that the Moon was ∼91% full, with a large >80 deg separation from our target. We observed the Gaia17bpp for a total of 23, 3-minute images to eliminate sky brightness background and noise levels. We did not perform dithering. We reduced our data following standard calibration procedures. We assumed a photometric-zero-point offset for the SDSS-u filter of 24 mag. We used the Python open-source tool, `photutils` (Bradley

[8]https://www.wis-tns.org/object/2017exj

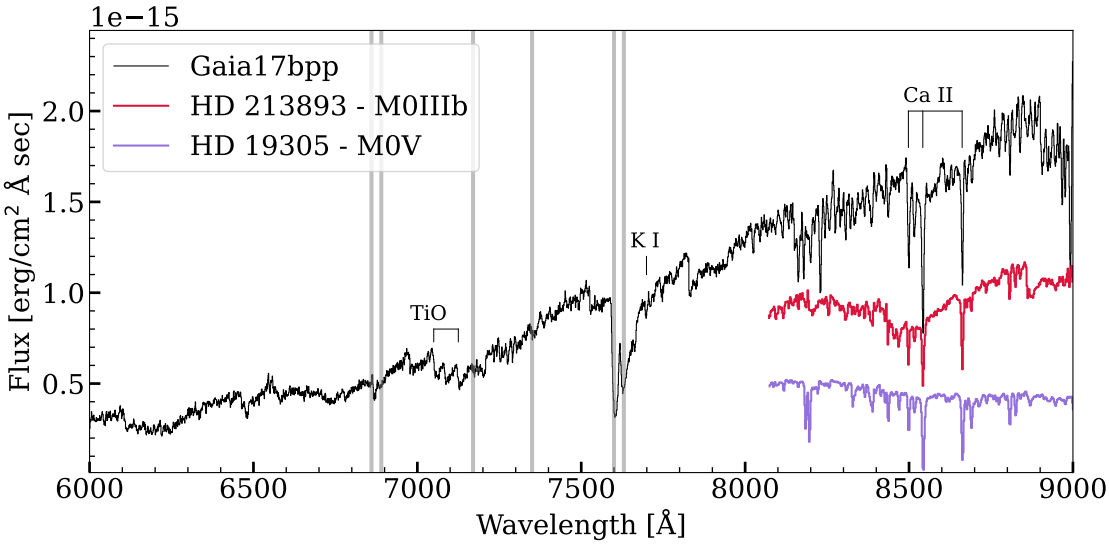


Figure 3.4: The optical spectrum of Gaia17bpp using the APO 3.5-meter KOSMOS spectrograph using the high-red grating. The uncorrected telluric lines have been marked with gray solid lines. We compare the Gaia17bpp spectrum to HD 19305 (M0V) and HD 213893 (M0IIIb) standards (Rayner et al., 2009).

et al., 2022), to perform the standard reduction of the SDSS-u band science images, including our calibration files. No source was detected within 10 arcseconds of the Gaia17bpp sky position. Based on the 5σ identified sources we found in our deep ARCTIC images, the distribution was roughly Gaussian with an average SDSS-u band magnitude of $\sim$22 mag.

4 Primary Star

4.1 Spectral Energy Distribution

We attempt to infer the physical parameters of the primary star. Given the rich multi-wavelength archival photometry, we perform a stellar SED modeling to constrain the properties of the primary star using open-source SED fitter `Ariadne` (Vines & Jenkins, 2022). `Ariadne` deploys a suite of stellar atmosphere model grids by performing a convolution of synthetic SED atmospheres and broadband photometry to constrain the effective temperature, metallicity, distance, radius, and extinction of a given SED. It performs a dynamic Bayesian multi-nested sampling algorithm through `dynesty` (Speagle, 2020), and amalgamates each stellar atmospheric model using a Bayesian Model Averaging (BMA) to finally estimate the best-fitted model parameters of a given primary star through a weighted average. In our case, we began by including all the observed broadband photometry outside the dimming event. In Table 4.1 we summarize the median observed magnitudes outside the primary dimming event from all epochs before 2013 or after 2018. For the fitting, we assumed a Fitzpatrick (1999b) extinction law with A_V=5.3 assuming a Galactic R_V=3.1 value. In Table 3.3 we show the priors and posterior distributions used for this analysis.

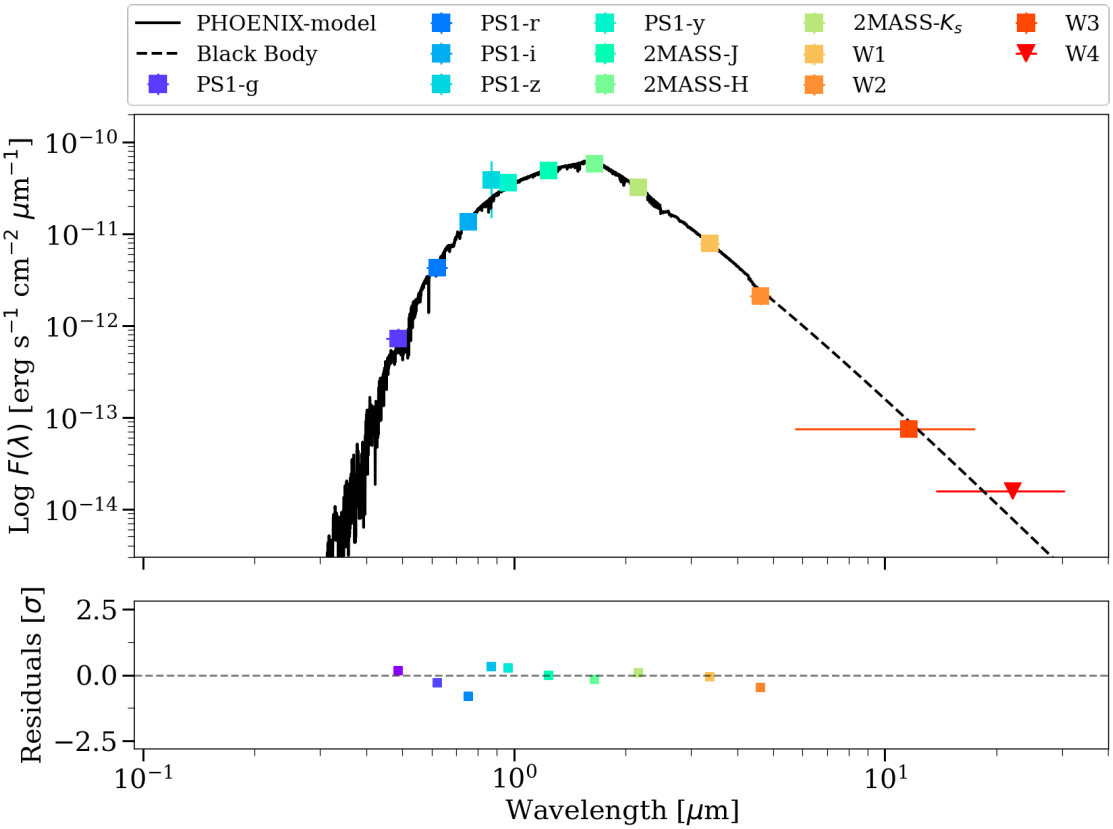


Figure 3.5: Spectral energy distribution fit (black synthetic PHOENIX spectrum) to the obtained broadband photometry outside the Gaia17bpp dimming event. We also include a simple black body fit to the photometry accounting for the effects of extinction at the line of sight. The bottom panel represents the residual levels from the PHOENIX model. We note that the SED fitting model does not extend to the W_3 detection and W_4 upper limit.

In Figure 3.5 we show the synthetic BMA PHOENIX atmospheric model that best fits our broadband photometry up to 4.6 μm. In our SED plot, we also include the W_3 detection and W_4 upper limit of the primary star; however, the SED fitter does not fit those detections. We extended the synthetic PHOENIX model continuum by fitting a black body function at the best-fitted temperature, radius, and distance (shown in dashed lines in Figure 3.5). The average fitted model shows convergence on a well-constrained posterior distribution seen in Figure 3.6, including their 25th, 50th, and 75th percentiles. The posterior distance distribution is in good agreement with the photo-geometric distance estimation. According to the physical estimates we derive from the SED fitting, we find the primary star to be consistent between a K5-III or M0-III giant star according to the classification regime, considering its effective temperature, radius, and surface gravity (Ceillier et al., 2017; Dumm & Schild, 1998; Dyck et al., 1996). The interpretation of a cool giant star is also consistent with the identified spectroscopic features discussed in Section 3.5. Using the maximum likelihood from the BMA, `Ariadne` also fits in the background MIST isochrones given the derived luminosity and temperature to estimate the mass. In Figure 3.7 we show both the posterior distribution of the resulting stellar mass, including the kernel density estimation (KDE). It is evident that the isochrone mass posterior distribution is bimodal with a higher probability density for a lower mass stellar model with a median of 1.56 $M_\odot$.

Survey/Band	Magnitude	Magnitude Error
2MASS-H	10.7420	0.0210
2MASS-J	12.0080	0.0220
2MASS-Ks	10.3080	0.0180
PS1-g	19.5110	0.0332
PS1-i	15.3795	0.0130
PS1-r	17.0549	0.0089
PS1-y	13.7903	0.0452
PS1-z	13.9440	0.1893
WISE-W1	10.0630	0.0240
WISE-W2	10.1690	0.0220
WISE-W3	9.9180	0.1469
WISE-W4	8.774[9]	0.1469

Table 3.2: Compiled broadband median photometry of Gaia17bpp outside the dimming events before December 2011 or after January 2019
. We assume that the intrinsic stellar SED is the same before or after the dimming event.

4.2 Primary Star Variability

Since the primary large amplitude dimming event, the Gaia17bpp system thus far has not exhibited any other large-scale variability beyond an overall 0.05 mag baseline scatter that

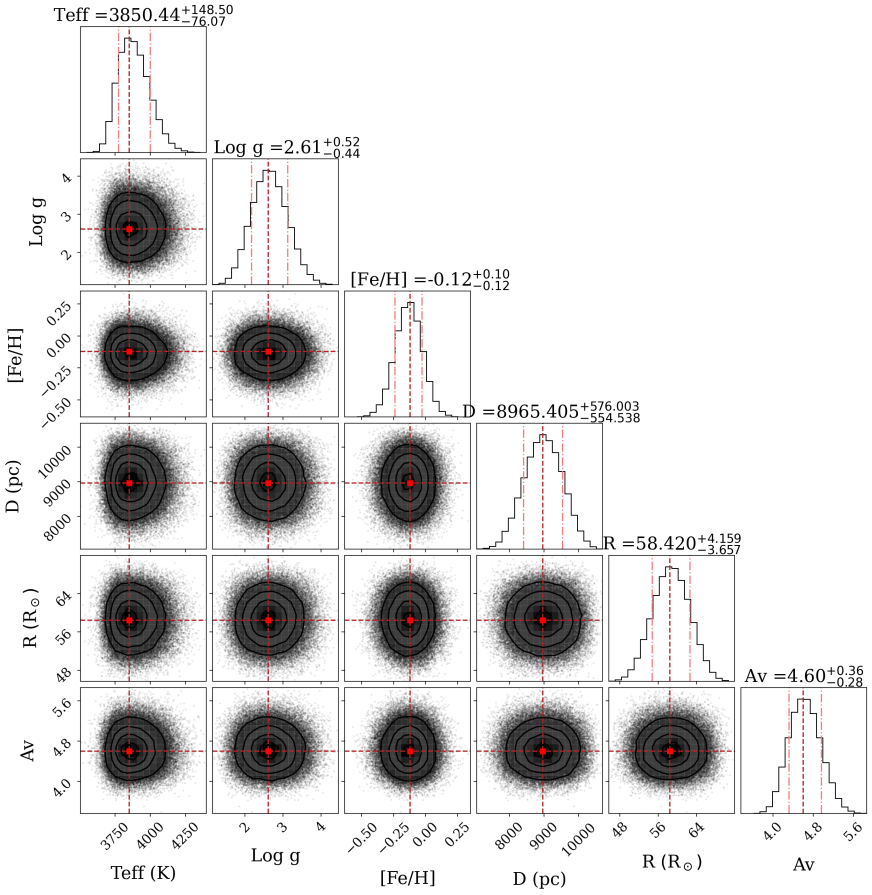


Figure 3.6: Corner plot of the posterior distribution from the nested Monte Carlo sampling using `Ariadne`. The dashed lines are the median and 2σ confidence interval of each distribution.

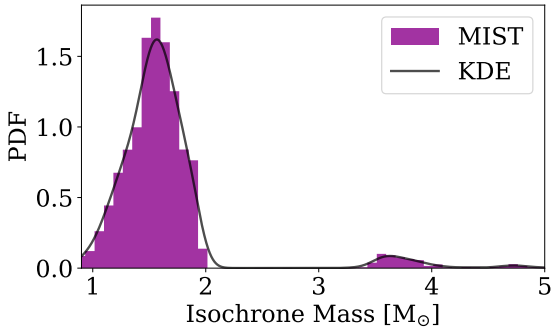


Figure 3.7: MIST isochrone mass posterior distribution histogram including a kernel density estimation (black line).

Parameter	Prior	Posterior
$T_{\rm eff}$	$\mathcal{U}(3000, 5000)$	3927^{+155}_{-108} K
log(g)	$\mathcal{U}(1, 5)$	$2.7^{+0.6}_{-0.5}$ cm sec^{-2}
[Fe/H]	$\mathcal{U}$(-1, 0.5)	$-0.1^{+0.1}_{-0.1}$ dex
$R_{\rm ad}$	$\mathcal{U}(5, 100)$	59.7^{+3}_{-5} $R_\odot$
$D_{\rm ist}$	$\mathcal{U}(7000, 10^4)$	9250^{+394}_{-770} pc
A_V	$\mathcal{U}(2, 5)$	$4.75^{+0.4}_{-0.3}$ mag

Table 3.3: The table contains the prior and posterior distributions from the primary star SED analysis. For the posterior distribution, we report the median and the 2σ posterior distribution range.

was calculated using the ZTF-g, ZTF-r, and Gaia G light curve at all observations after 2018. We searched the ZTF-g, ZTF-r, and Gaia G light curves for periodic or quasi-periodic variability outside the dimming event. We ran a single-band Lomb-Scargle Periodogram (LSP) (Lomb, 1976b; Scargle, 1982b) using `gatspy` (VanderPlas & Ivezić, 2015) using a two-component Fourier model. Across each photometric bandpass, we got inconsistent periods at maximum power, which is likely due to the difference in cadence between each filter and survey, despite the identification of periods exceeding 90 days in our LSP analysis, indicative of pulsating red giants in accordance with Kepler light curves (Ceillier et al., 2017). We calculated the significance of the peak through a bootstrap extrapolation and found that it fell below the 2σ threshold.

5 Dimming Event Properties

5.1 Light Curve Properties: Optical to IR

Given the remarkably long duration of the dimming event of Gaia17bpp, there are five photometric bandpasses that extensively covered the second half of the dimming event. The bottom panel in Figure 3.3 shows how stitching together detections from multiple surveys and photometric bandpasses reveals almost the entirety of the dimming event except for the ingress. Both WISE and NEO-WISE light curves did not show any evidence of large amplitude variability during both the occultation and dimming phases. Based on a 30-day median sliding window, we found that the light curve did not vary more than 0.2 magnitudes across both the W_1 and W_2 magnitudes. The W_1 and W_2 light curves returned back to their median baseline brightness after the dimming event. Similarly, the Gaia G light curve did not exhibit any structure during the dimming event. Due to the sparse coverage of all presented photometric measurements, we recognize that there might exist variability on shorter timescales that are not captured.

Perhaps the more puzzling property of the Gaia17bpp system is the variation in colors across different epochs. In Figure 3.8 we show the color evolution of the dimming event, including the non-dimming phase in three photometric bandpasses. In order to get the same epochs for the WISE and Gaia photometry, we binned the detection by a running median of 100 days. We first begin to note the constant color during the quiescent phase found

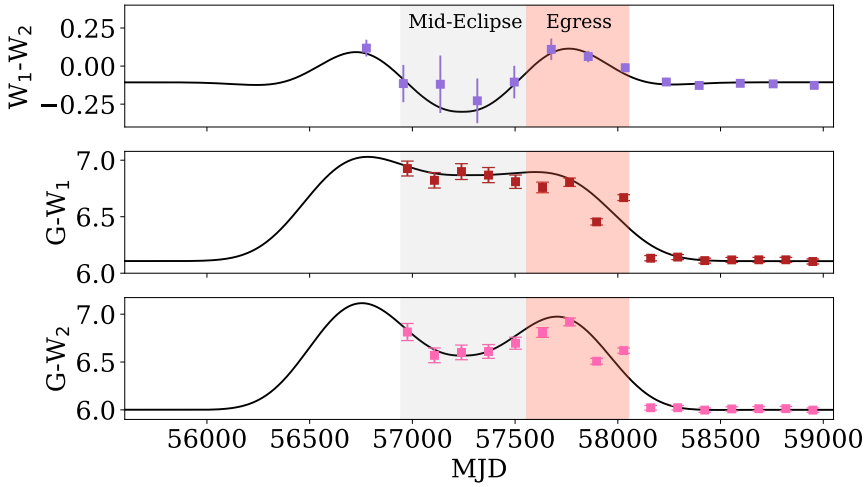


Figure 3.8: Color evolution of Gaia17bpp in the infrared and infrared-optical photometry. We highlight in gray the primary region of the dimming event and in red the egress of the dimming event. In each panel, the underlying solid black line model was produced from a generalized Gaussian distribution described in Section 5.

in any epoch beyond January 2019, this constant color profile is the inherent color of the primary star including Galactic foreground extinction. We do not observe any significant color variations within this phase. On the other hand, both the egress and bottom of the dimming event show substantial color variation. For example, in the top panel of Figure 3.8 we observe during the minimum of the dimming event, the (W_1-W_2) color was ∼0.2 mag different compared to the color of the primary star outside the dimming event. We suggest that the shorter wavelength W_1 (3.4 μm) magnitude was brighter compared to the longer wavelength W_2 (4.7 μm) magnitude, indicating the excess shorter wavelength flux with respect to the primary star (henceforth referred to as the blue-bump). Similarly, the Gaia-WISE colors also suggest a similar evolution and a small blue-bump at the minimum of the dimming event at different rates. The last two detections are also somewhat curious with a 200-day color 0.1 mag variation from blue to red, however, it is difficult to tell if these are spurious detections or related to the dimming mechanism.

Given the five unique photometric filters, we have that captured the egress of the dimming phase, we suspect that the shape of the light curves can possibly change from optical to infrared assuming that the obscuring process does not have an underlying grey spectrum. To test this hypothesis, we fit the overall properties of the light curve with a Generalized Gaussian Distribution (GGD):

$$\mathcal{A}\frac{\beta}{2\alpha\Gamma(\beta^{-1})}\, e^{-(|x-\mu|/\alpha)^{\beta}} \tag{3.1}$$

with light curve amplitude ($\mathcal{A}$), mean (μ) time, standard deviation (α) that controls the width of the distribution, and overall order of the GGD (β) overall shape of the GGD. The mathematical properties of the GGD are presented by Dytso et al. (2018); see also Cadirci et al. (2022). The power of the underlying GGD is the ability to control the flatness of the Gaussian peak, since we can visually tell that the bottom of the dimming event was

flat. To account for any unwanted correlated noise measurements, we simultaneously model the underlying correlated noise with a Gaussian Process (GP) with `George`[10] (Ambikasaran et al., 2015) including the mean model parameters via Markov chain Monte Carlo (MCMC). We use `Emcee` (Foreman-Mackey et al., 2013) that implements the Metropolis-Hastening algorithm used to constrain the posterior distribution. The correlated noise that might be present in the multi-band light curves was captured by a Matérn-3/2 covariance function. We simultaneously fit the GP hyperparameters, including the underlying model.

Overall, the GGD model provided a good fit for the Gaia-RP, Gaia G, W_1, and W_2 light curves as seen in Figure 3.10. Based on our GP analysis, we found clear deviations from the shape of the light curves across each bandpass. For example, in Figure 3.9 we show the posterior distributions for the model mean time, amplitude, standard deviation, and shape of the GGD profile for each light curve. According to the interquartile range of each distribution, the mean time, standard deviation, and amplitude show variations. Based on the wide distributions we obtained from the model mean epoch, all light curves had a minimum flux of around June 2016 (57200 MJD) within a margin of error of ∼400 days. We notice that the WISE light curves have a ∼150-day different mean time compared to the optical Gaia light curves. It is noticeable how the variance of the α posterior distribution shifts from the optical 550 to 450 in the infrared, suggesting that the optical light curves have a slightly longer duration. Thus, we find the light curve profile of the Gaia17bpp dimming event is modestly asymmetric. The modest asymmetric dimming profile likely highlights a weak wavelength dependence that reflects the intrinsic properties of the obscuring object. We note that the narrow range of posterior distribution, particularly for the less complete Gaia G and RP light curves, is reflected in our assumed light curve shape. We could not successfully place firm limits on the BP light curve since it suffers from a large scatter. In Figure 3.10 we display our GP GGD fits drawn from the posterior distribution for the RP, Gaia G, W_1, and W_2 light curves, including their residuals.

Given the poor photometric coverage at the minimum of the dimming event, we do not have enough multi-band photometry to perform any SED inference. We attempted to fit a simple black body model to the BP, G, RP, PS1-y, W_1, and W_2 detections and found that the temperature was consistent with the findings of the dimming phase at 3800 K. We only notice that the dimming detections are roughly equivalent to the non-dimming detections scaled down by some factor.

6 Discussion

6.1 Intrinsic Variability Scenarios

Month- to year-long dimming events have been identified from rare hydrogen-deficient carbon-rich stars, R Coronae Borealis (RcB) type variables that eject large carbon-dust clouds. RcB stars are known for their erratic and asymmetric dimming profiles and are dominated by mostly helium, nitrogen, and carbon enrichment in their atmospheres (De Marco et al., 2002). We found no He-I emission or P-Cygni profile in our optical spectrum. RcB stars are also known to exhibit mid-IR excess due to warm circumstellar dust shells found around

[10] https://george.readthedocs.io/

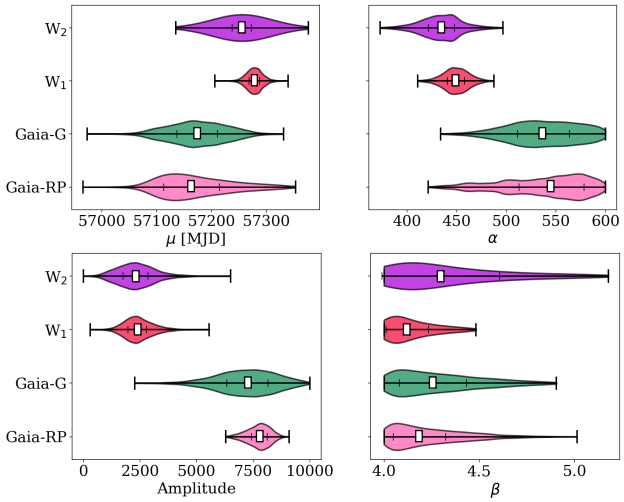


Figure 3.9: Violin plot displaying the posterior distribution of the generalized Gaussian distribution fitted for each photometric bandpass. The shape of each violin represents the KDE of the distribution, with the vertical black lines and white rectangles indicating the interquartile range. Solid lines at the violin end represent the minimum and maximum values of the KDE.

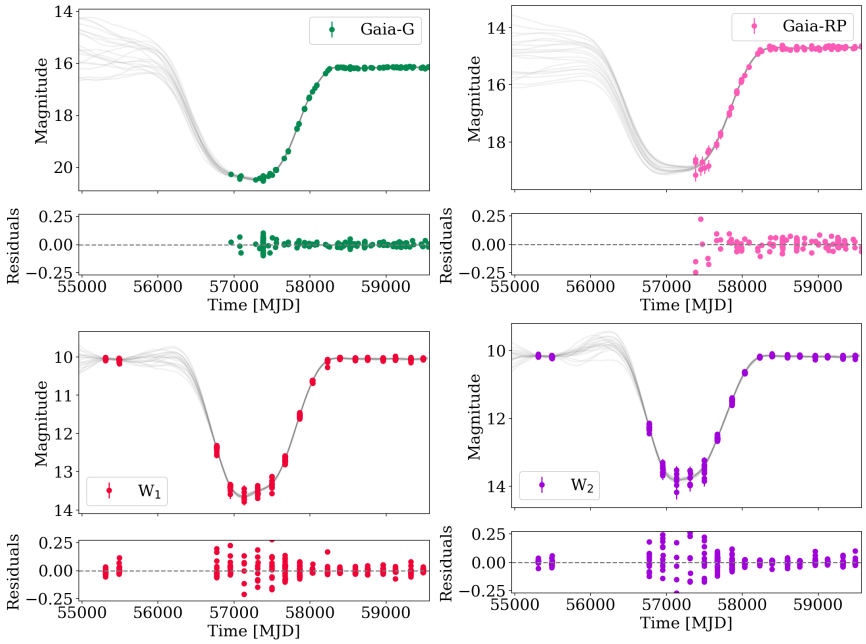


Figure 3.10: Gaussian Process fits (grey lines) drawn from the posterior distribution for the Gaia G, Gaia RP, W_1, and W_2 light curves, including their residuals at the bottom of each panel.

them (Tisserand, 2012). No carbon absorption features or other spectroscopic RcB signatures were found in our optical spectrum. Considering the stellar SED of Gaia17bpp, we also do not find any evidence of mid-IR excess. We examined the WISE color-color magnitude diagram of the primary star to see if the colors were consistent with known RcB stars. We compared the $(W_1\text{-}W_2)_0$, $(W_3\text{-}W_4)_0$ with values -0.17 and 1.1 respectively, and found that the observed color is 0.5 mag away from where typical RcB stars have been found in the WISE catalog (Tisserand et al., 2020). Given the additional absence of any other erratic variability and the non-asymmetric light curve of Gaia17bpp, we find it unlikely that it is an RcB candidate.

Red supergiants (RSG) are also known to exhibit large amplitude dimming events that can last up to a few months to a year (Dupree et al., 2022; Massey et al., 2007). One particular case study is the great dimming event of Betelgeuse which exhibited a deep 2-month-long dimming event. Initial interpretations noticed the temperature of Betelgeuse had cooled down to 3600 K, and suggested surface convection effects caused the dimming event. Levesque & Massey (2020) discussed that a large and cool convection cell on Betelgeuse would have caused strong TiO bands with a substantially lower temperature; instead, the leading hypothesis is an episodic mass loss event with large grain circumstellar dust. Our current analysis does not favor an RSG classification for Gaia17bpp given its modest radius and low-mass estimates based on the SED. Similarly, the duration of the dimming event we observe is not compatible with the timescales currently reported in the literature on dimming RSG stars (Kiss et al., 2006). We find it unlikely that the Gaia17bpp dimming mechanism was caused by the ejection of a dust cloud around RSG stars.

6.2 Extrinsic Variability Scenarios

Our current available data do not provide evidence that Gaia17bpp is a compact X-ray binary or an energetic cataclysmic variable (CV). We searched through known X-ray catalogs (ROSAT 2RXS, XMMDR10, XMMSL2, Chandra CSC2, Swift2SXPS) and found no sources at the location of Gaia17bpp except for a 2σ upper-limit from Swift/XRT count rate at 0.36 counts per second. We derived an X-ray limiting luminosity of approximately 10^{35} erg sec^{-1} at the distance of the source[11]. Given the relatively shallow upper X-ray flux limit at this line of sight, it is possible that Gaia17bpp is an active X-ray source but has been missed due to the lack of deeper limits. Other common telltale signs of accretion are usually seen in Hα emission from an ionized disk (Williams, 1980). As seen in Figure 3.4, we do not see any narrow Hα or other emission lines of ongoing accretion. Given the lack of erratic photometric variability, no X-ray detections, and no evidence of narrow emission lines in the optical spectrum at the time, we do not believe the dimming of Gaia17bpp results from the activity in an accretion disk.

Young stellar objects (YSO) are systematically known to display deep and complex dimming events on timescales of months to years called dipper events (Cody & Hillenbrand, 2018a). In most cases, YSO disks are also luminous X-ray and radio sources due to the

[11]To calculate the limiting X-ray luminosity, we utilized the NASA HEASARC WebPIMMS calculator. For our calculation, we assumed an H I column density at the line of sight to be 6.9 cm^{-2}, assuming a median distance of 8462 parsecs. We assumed no intrinsic HI column density.

strong magnetic fields and high temperatures from ongoing accretion (Feigelson & Montmerle, 1999). Our archival data does not support a YSO scenario, given the lack of infrared excess and the lack of bright nearby radio or X-ray sources. Since the typical timescales of YSO disks are a few Myr, we do not expect to find such a young companion near an evolved giant star. Finally, the sky position and estimated distance of Gaia17bpp are not near any known star-forming regions.

6.3 Occulting Disk Model

As discussed in Sections 6.1 and 6.2, there is no currently known intrinsic or extrinsic dimming mechanism outside the M giant that can cause stars to smoothly dim for prolonged periods. We now turn our attention to the most likely cause of the dimming event, which would be driven by the occultation by a disk that explains the dimming event of Gaia17bpp.

The smooth and asymmetric dimming event of Gaia17bpp can be plausibly explained by the transit of an oblate disk similar to that of ϵ-Aur analog systems. For example, Rappaport et al. (2019) showed that EPIC 204376071, a young M-type star, was obscured by an oblate tilted dusty disk. To compute the transiting models, they used a modified version of `pyPplusS` (Rein & Ofir, 2019) that computes light curves for oblate spherical exoplanets that possess rings and can account for both uniform and limb-darkened scenarios, which are performed using the Polygon-Segments algorithm. Rappaport et al. (2019) expanded this tool by adding a full opacity layer to the rings to simulate the transit of an oblate disk.

Parameter	Prior	Posterior
R_{disk} $[R_*]$	$\mathcal{U}(0.1, 10)$	$6.5^{+4.0}_{-2.8}$
b	$\mathcal{U}(0, 10)$	$2.6^{+4.9}_{-2.6}$
i $[rad]$	$\mathcal{U}(0, \pi)$	$1.0^{+0.3}_{-0.7}$
ϕ $[rad]$	$\mathcal{U}(0, \pi)$	$3.1^{+0.1}_{-0.2}$
v $[km\ sec^{-1}]$	$\mathcal{U}(10^{-4}, 10)$	$0.005^{+0.002}_{-0.001}$
dx	$\mathcal{U}(0, 200)$	$114.0^{+79.5}_{-63.8}$

Table 3.4: The table contains the prior and posterior distributions from the oblate disk modeling. For the posterior distribution, we report the median and the 1σ range.

We attempted to apply this suite of models to the W_1 light curve of Gaia17bpp since it contains detections from all phases of the event. One of the key modifications we made to the existing code was to also include in the fitted light curve the limb-darkening coefficient. Given the priors we obtained from our SED analysis, we only consider the c_2 coefficient of the quadratic limb-darkening equation since the first linear term is very small[12]. For the purpose of this study, we only fit a model of an oblate solid disk model with seven parameters: disk radius in radii of the primary star (R_{disk}), impact parameter (b), orbital inclination (i), the tilt angle of the disk (ϕ), transverse speed of the disk across the host star (v), time shift (dx), and finally the quadratic polynomial limb-darkening term (c_2). We

[12]To calculate a preliminary limb-darkening coefficient, we used the Exoplanet Characterization Toolkit calculator (https://exoctk.stsci.edu/limb_darkening).

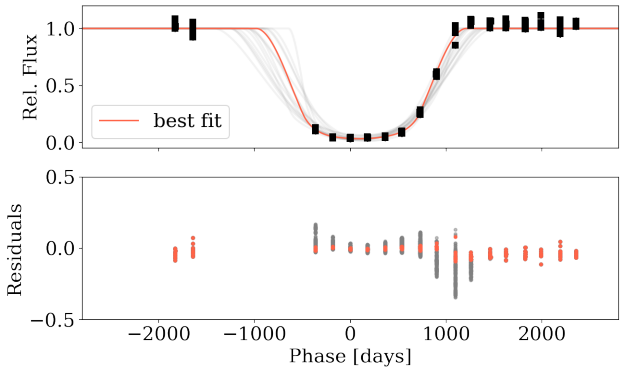


Figure 3.11: Gaia17bpp WISE-1 light curve fitted by an oblate solid disk model (top) and model residuals (bottom). In pink, we show the maximum likelihood fit to the data. The gray points represent random draws from the posterior distribution.

explored a variety of different model parameters that could produce a 7-year-long dimming event. We found that the models that could produce such long events needed to have low transverse velocities, which likely indicates the large semimajor axis between the occulter and primary star. We proceeded to perform an MCMC implementation using a standard Gaussian likelihood function. In the limitations of poor constraints on the geometry of the system, we assumed broad uniform priors for all parameters. In Figure 3.11, we show the model fit against the data. While the disk light curve model performs overall a reasonably fit to the data, we do find some weakly correlated noise within the residuals (bottom panel of Figure 3.11). Considering the limited constraints at our disposal and the prior orbital configuration of this system, it remains very challenging to constrain based on the current data. Nonetheless, we found that the semi-major axis of the disk is roughly 1.4 AU, and the angle between the semi-major axis and the direction of motion across the sky is inclined by ∼178 degrees. It is thus possible that we are seeing the disk obscuring the star edge-on since we also find the impact parameter to be small (b∼0). The marginalized posterior distribution also suggests that the transverse velocity is low, approximately at 0.005 km sec^{-1}. In Table 3.4, we summarize the marginalized posterior distribution from our analysis. We attempted to repeat the same model with the exception of introducing an additional ring to the oblate occulter with some tunable opacity term. We found that such a two-layer oblate occulter was not capable of fitting the overall shape of the light curve due to the steep transition between a solid disk and another additional optically thin layer. Based on the performance of our single oblate transiting model, we have reasonable evidence to suggest that the occulting object of Gaia17bpp must have been an extended object such as an oblate disk. However, in order to establish more robust constraints on the geometry of the disk, additional multi-band light curve modeling will be needed.

We have reasonable data to challenge the unlikely scenario of a circumbinary precessing disk, such as the case of KH 15D-like analogs (Windemuth & Herbst, 2014; Zhu et al., 2022). For example, almost all known KH 15D-like analogs have been found to have characteristic shallower infrared light curves, including a clear excess in infrared. Additionally, given the collected photometry, we were unable to find any short-period signals indicating the presence of the companion. One similarity between Gaia17bpp and KH 15D-like analogs is

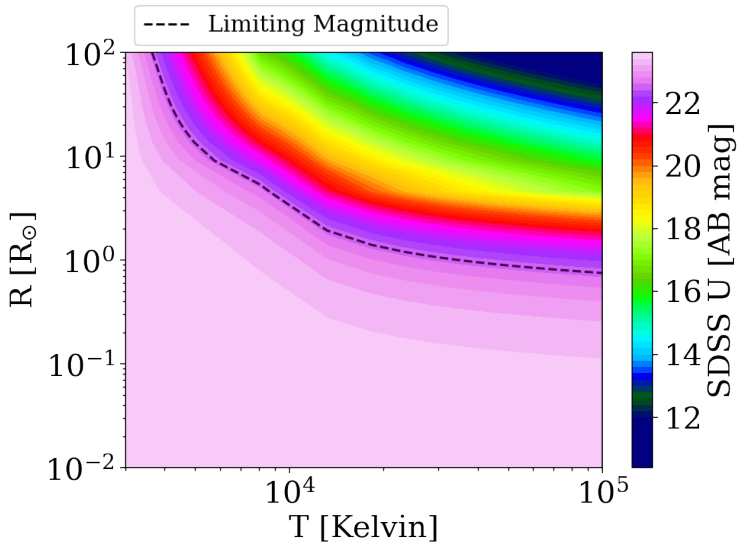


Figure 3.12: Grid of blackbody mixture model including the radius and effective temperatures of the secondary star, color coded by the integrated SDSS-u AB magnitude. The dashed line represents our limiting SDSS-u band magnitude. We assume the primary star has a fixed radius of $58R_\odot$, an effective temperature of 3850 K, and a median distance of 8965 pc.

the blue-bump feature in the infrared light curves. Based on the archival data alone, we are unable to identify the mechanism behind the blue bump observed during the minimum of the Gaia17bpp dimming event. One possible scenario is the presence of another hot source contributing to the observed color at the bottom of the dimming event. A second scenario is the effect of Mie forward-scattering due to the dust grain size that is comparable to the wavelength (Silvia & Agol, 2008b). It is thus indicated that the characteristic grain size of the Gaia17bpp occulting disk is likely larger than the average foreground interstellar medium (Arulanantham et al., 2016). Compared to other possible candidates of the same nature, for example, ϵ-Aur example (Carroll et al. (1991) see Figure 5 therein) that has clear amplitude variations during the maximum eclipse, Gaia17bpp shows overall smaller variability, which might shed light on the geometry and optical depth of the occulter. Gaia17bpp and ϵ-Aur also show similarities in asymmetries in their light curve properties throughout different bandpasses, with ϵ-Aur having an ingress dimming and somewhat steeper egress brightening phase (Stencel, 2012). Given our findings on the modestly asymmetric dimming event across the multi-band light curves of Gaia17bpp, we hypothesize that a weak wavelength dependence might be connected to the overall properties of the occulting disk (Parthasarathy & Frueh, 1986). It has been found that debris disks may lack infrared emission due to the non-radial distribution of mass, compared to typical protoplanetary disks (Hughes et al., 2018b). Stencel et al. (2011) attempted to find evidence for an infrared excess or silicate features in ϵ-Aur, however, the SED was found to be smooth and lacked classic dust features. It is suggested that large particles in a debris disk in ϵ-Aur could account for the observed SED. Both cases of ϵ-Aur and TYC 2505-672-1 have evidence to suggest the scenario of a debris disk around the secondary star. Thus, this would also be in line with a lack of infrared

excess that we notice with the Gaia17bpp system. Given the limitations of the archival data presented here, future far-IR studies with more sensitivity should investigate whether the presence of a cold optically thick disk exists beyond the wavelength ranges explored in this work.

Given Gaia's superb micro-arcsecond resolution, if a luminous companion existed, it would likely be detected by Gaia. For instance, assuming a 1.5 $M_{\odot}$ and a minimum orbital period of 66 years, we estimate that the minimum angular separation is 516 μas, which is within the resolving capabilities of Gaia. We searched a 0.1 deg^2 overlapping area with Gaia17bpp through both Gaia DR2 and DR3 catalogs to look for any detected sources that might be associated with this system. We identified two faint sources (Gaia DR3 1636148068921376768 with G_{mag}=21.1, and Gaia DR3 1636148068921376768 with G_{mag}=20.5) within this cone search; however, they lacked astrometric solutions or had large parallax measurements. While we are unable to confirm the association of these sources with Gaia17bpp, future studies should examine more closely their possible association. On the other hand, the non-detection of the secondary star was not a surprise. First, we are limited to shallow NUV detection due to the high line-of-sight extinction and distance of Gaia17bpp. Second, if the secondary is surrounded by an extended disk, then it is possible the companion star is hiding within, such as the ϵ-Aur B5V stellar companion (Stencel, 2012). We constructed a simple toy model of a blackbody mixture model that incorporates the blackbody emission flux from the primary, and a hypothetical secondary at the same distance, including the effects of Galactic attenuation. In Figure 3.12, we vary the temperature and radius of the hypothetical secondary star and integrate the blackbody mixture model to estimate the approximate SDSS-u AB magnitude. We include in Figure 3.12 the derived SDSS-u ∼22 mag from our images as a dashed line. Based on our limiting magnitude, we cannot exclude the presence of a main sequence, white dwarf, or neutron star companion based on the observations alone. Further deep observations in the NUV and FUV will be required.

In Figure 3.13 we compare the relative photometric depth of Gaia17bpp with other giant dimming stars obscured by occulting disks, sorted from the shortest to the longest duration dimming events. It is evident that the Gaia17bpp system has by far the longest and deepest dimming event found amongst these candidates. It is possible that the variation in light curve properties we see here is due to the geometric configurations of such disk companions. Based on the archival photometry alone, it is unclear if Gaia17bpp is periodic. Based on the archival detections from DASCH and other surveys, we find it likely that no other major dimming event has occurred. Given the detections we have made from DASCH and POSS, we can assume a lower limit to the orbital period of at least 66 years. This would be in agreement with our occulting disk model, which would suggest a very long orbital period given the very low transverse velocity.

7 Conclusion

In conclusion, we report the serendipitous discovery of Gaia17bpp/2MASS J19372316+1759029, an anomalous binary star that exhibited a single, ∼7-year long, and 4.5 magnitudes deep dimming event. Using a collated data set of multi-band light curves across several surveys

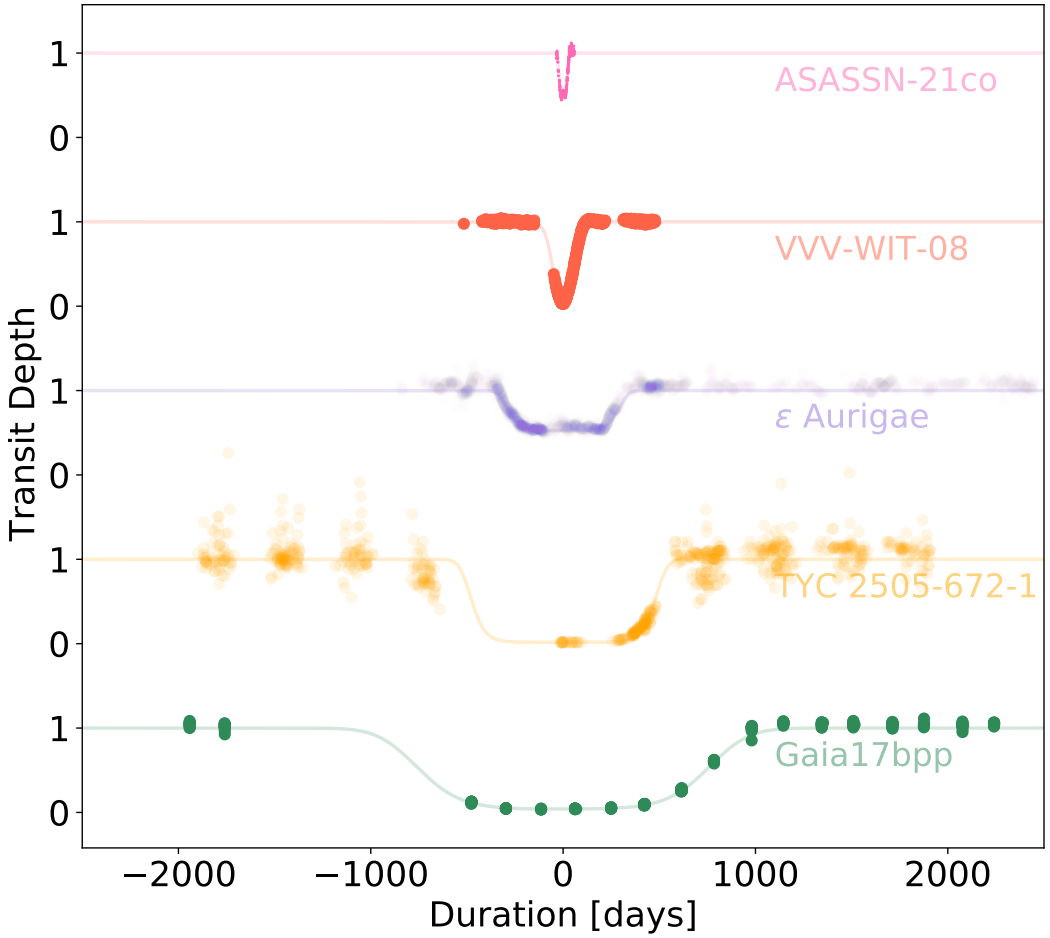


Figure 3.13: Normalized transit light curves of ϵ-Aur-analog systems ordered by event duration. Gaia17bpp (W_1bandpass) exhibits the longest and deepest duration event. We sort each dimming event from the shortest (top) to the longest (bottom) in the following order: ASASSN-21co (Rowan et al., 2021), VVV-WIT-08 (Smith et al., 2021), ϵ Aurigae (see Kloppenborg et al. (2012) and references therein), TYC 2505-672-1 (Lipunov et al., 2016), and Gaia17bpp.

and wavelength regimes, we find that this unique system closely resembles the variability seen from evolved giant stars transited by companion stars with opaque disks. We constrain the primary star of Gaia17bpp through a Bayesian amalgamation of stellar SED models. We conclude that the primary star is likely a $58R_{\odot}$ M0-III giant star, favoring a low-mass primary star that is consistent with the radius and mass profile of an ordinary giant M giant star. The long and complex nature of the dimming event is not fully understood. We find evidence that the WISE IR light curves are shallower, asymmetric, and have slightly different shapes from their optical counterparts. The color evolution of the dimming event is also perplexing in both optical and IR colors, which is not fully understood. We suspect that the main culprit of the dimming event is linked to an emerging population of rare binary systems with a companion enshrouded in a debris disk, such as the case of ϵ-Aur. Finally, We performed a simple tilted-disk eclipse model of the W_1 infrared light curve. We found that the disk would need to be inclined by 178 deg, and slow-moving with an approximate radius of 1.4 AU. Based on the currently available data, we cannot identify a secondary companion star.

Slow and photometrically deep dimming stellar systems will become even more relevant in the near future. The forthcoming Vera C. Rubin Observatory Legacy Survey of Space and Time (LSST; Ivezić et al. (2019)) promises a survey of long duration and unprecedented photometric depth. LSST will contain both a long-time baseline and unprecedented photometric depth in *ugrizy* that will lead to the discovery of many more such extraordinary eclipsing systems.

8 Acknowledgments

We thank Christina Hedges and Tobin Wainer for their useful conversation regarding the TESS photometry in crowded Galactic fields. We also thank Robert Stencel for their useful comments concerning Epsilon Aurigae, and the anonymous referee for their constructive comments on the manuscript. Based on data from the CMC15 Data Access Service at CAB (CSIC-INTA). This project was partially funded by the Department of Astronomy Jacobsen Fund at the University of Washington. This publication makes use of data products from the Wide-field Infrared Survey Explorer and NASA/IPAC Infrared Science Archive, which is a joint project of the University of California, Los Angeles, and the Jet Propulsion Laboratory/California Institute of Technology, funded by the National Aeronautics and Space Administration. Some of the data presented in this paper were obtained from the Mikulski Archive for Space Telescopes (MAST) at the Space Telescope Science Institute. The specific observations analyzed can be accessed via [https://doi.org/10.17909/ptkv-m411]https://doi.org/10.17909/ptkv-m411. STScI is operated by the Association of Universities for Research in Astronomy, Inc., under NASA contract NAS5–26555. Support to MAST for these data is provided by the NASA Office of Space Science via grant NAG5–7584 and by other grants and contracts. This research made use of Photutils, an Astropy package for detection and photometry of astronomical sources (Bradley et al., 2022).

CHAPTER 4

A CATASTROPHIC PLANETESIMAL COLLISION CANDIDATE

1 Preface 94
2 Introduction 94
3 Data 95
4 Properties 99
5 Discussion 103
6 Conclusion 106
7 Acknowledgments 107
1 Cluster Membership Probability 109
1 Future Work 111
2 Surveys and Data of the Future 114

1 Preface

The following work has been accepted for publication in the *The Astrophysical Journal Letters* (ApJL) series.

2 Introduction

Giant impacts represent some of the most fundamental events in late-stage planetary formation. Canonical planet formation theories predict that terrestrial planets reach their final mass assembly through collisions between up to Mars-sized planetesimals, typically during the first ∼100 Myr of the system evolution (Wyatt & Jackson, 2016a, and references therein). Giant impact collisions are expected to be a common occurrence during the terrestrial planet formation era (Canup, 2004), with collision-generated debris disks persisting for millions of years and producing detectable infrared (IR) excess signatures (Wyatt, 2008b). These collisions are thought to be a primary driver of warm debris disks and occur 10% around young stars (Genda et al., 2015; Jackson & Wyatt, 2012b). Numerical simulations indicate that most Earth-like planets experience several giant impact collision events within 2 Gyr, with the vast majority occurring in the first 200 Myr (Quintana et al., 2016b). However, these simulations are computationally intensive, and a new generation of machine learning-accelerated simulations is being developed to explore wider ranges of impact velocities and masses (Lammers et al., 2024).

Time-domain monitoring is now surfacing plausible giant-impact aftermaths among young stars. Intensive photometric monitoring of extreme debris disks (EEDs) reveals week-to-month-long mid-IR and optical modulations that are consistent with optically thick post-impact clumps that shear around the orbits and then collisionally grind down (Kenworthy et al., 2023b; Moór et al., 2022; Rieke et al., 2021a; Su et al., 2022b, 2019). Within favorable viewing geometries and impact conditions, excess IR photometric variability is directly connected to the reprocessing of heat and dissipation of freshly generated debris (Meng et al., 2014; Rieke et al., 2021a; Su et al., 2022b), while the irregular optical variability arises due to the occultation of dusty sheared clumps (Jackson et al., 2014). Optical monitoring of young main-sequence stars has also revealed complex irregular dips with timescales spanning days to years, which have often been attributed to the impact collisions of planetary embryos, though with little presence of IR excess (Boyajian et al., 2016b; de Wit et al., 2013; JoHantgen et al., 2025; Tzanidakis et al., 2025; Zakamska et al., 2025b). The highly variable nature of impact collisions contradicts the scenario of steady-state cascades, and instead points to violent collisions among large bodies in the inner AU.

In this study, we present the discovery of Gaia-GIC-1, a low-luminosity infrared transient with simultaneous optical dimming, resulting from what we believe to be the collision of large planetesimals. This is the first such system discovered with the Gaia Alerts, and one of a very small number of such giant impact candidates known. Section 3 presents the details of the discovery and follow-up photometric and spectroscopic data. In Section 4, we lay out the light curve properties of the discovered system. In Section 5, we provide a discussion on the mass and properties of the occulting dust clump. We summarize our conclusions in Section 6 and outline future observations that could further illuminate the nature of this and

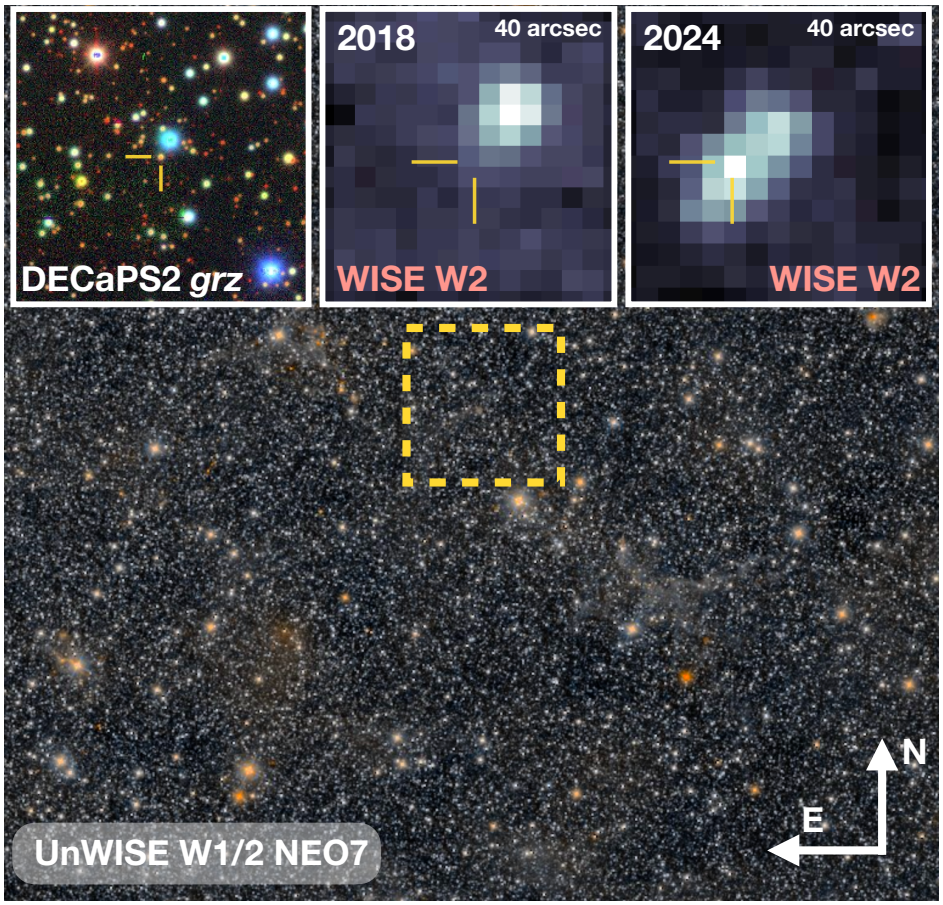


Figure 4.1: Multi–wavelength view of Gaia-GIC-1. **Top-left:** DECaPS2 three-color ($g\,r\,z$) mosaic, 40 arcsec ×40 arcsec, with the identified star marked by yellow cross-hairs. **Top-middle** and **top-right:** WISE/NEOWISE $W2$ (4.6 μm) cut-outs of identical size from 2018 and 2024, respectively, showing an increase in mid-IR brightening and a subtle centroid shift relative to the neighboring field. **Bottom:** unWISE $W1/W2$ NEO7 coadd. The dashed yellow box indicates a 20′x20′ region around Gaia-GIC-1.

similar systems.

3 Data

3.1 Optical Light Curves

Gaia20ehk (AT 2020tdg; Hodgkin et al. 2020) was first identified by the *Gaia* Photometric Science Alerts (GPSA) (Hodgkin et al., 2021b). We retrieved the GPSA G-band light curve with `GaiaAlertsPy`[1] (Tzanidakis et al., 2023). Archival i-band detections were gathered from SkyMapper DR4 (Onken et al., 2024) and DECam Plane Survey (Schlafly et al., 2018) (DECAPS). Additional follow-up i-band proprietary photometry was obtained on behalf of the

[1] `github.com/AndyTza/GaiaAlertsPy`

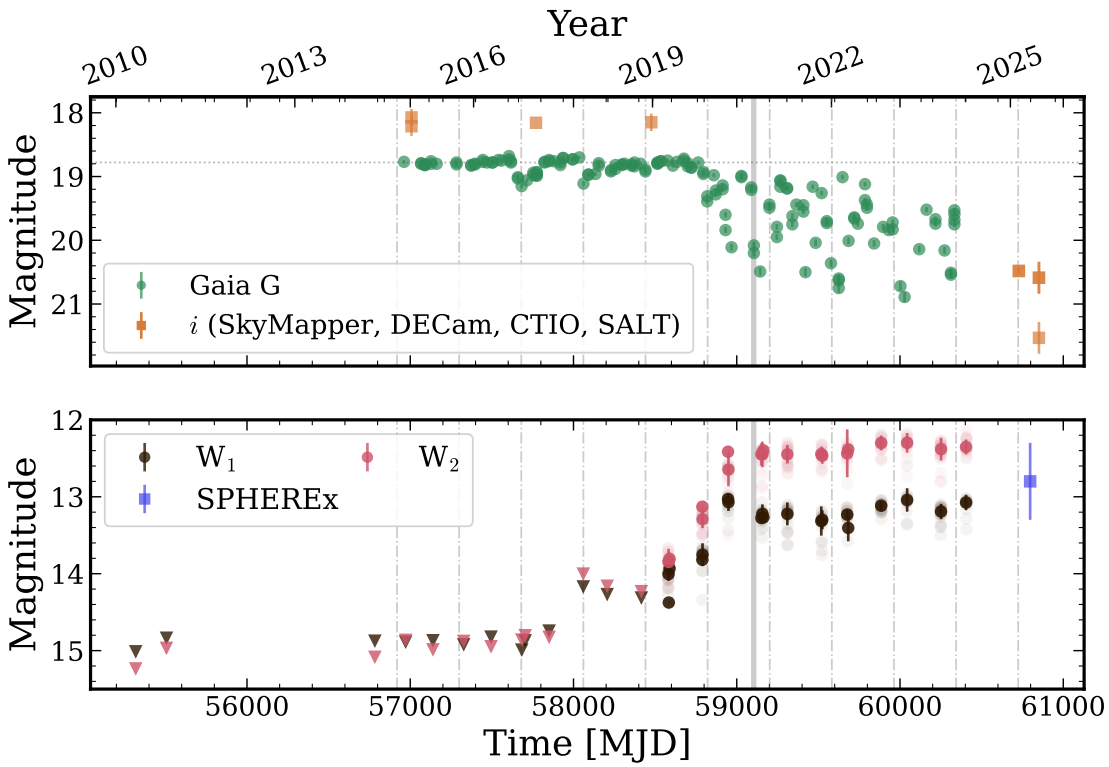


Figure 4.2: Compiled optical and infrared light curve of Gaia-GIC-1. (**Top**) Optical Gaia-G and i band light curves. The dashed horizontal line is the median Gaia-G magnitude in quiescence. (**Bottom**) WISE photometry in the W_1 and W_2, where upside-down triangles indicate the 3-σ upper limits. The dashed vertical gray lines mark a 380.5-day interval, and the highlighted solid gray line is the epoch of the Gaia alert. The data are available as a machine-readable table.

Microlensing Telescope Network (KMTNet; Kim et al. (2016)) from the Cerro-Tololo Inter-American Observatory (CTIO) and the South African Astronomical Observatory (SAAO) sites. One i-band detection was also provided through the SALTICAM target acquisition during spectroscopic follow-up, discussed in Section 3.3. Standard aperture photometry was performed on the obtained images using `photutils`[2]. We present an image of the sky location mosaic of Gaia-GIC-1 in Figure 4.1 identified by several surveys. The collated optical light curve is shown in the top panel of Figure 4.2.

3.2 Infrared Light Curve

Initial epochal infrared data were obtained using WISE unTIMELY (Meisner et al., 2023b), which contained epochs of data up until December 2020 that include up to year 7 of NEOWISE data. To obtain WISE data after 2020, we used the NASA IPAC Infrared Science Archive (IRSA) to download the WISE single epoch images in the W_1 and W_2 bandpasses of all WISE scans between 2021 and 2024 (WISE Team, 2020). We ran forced photome-

[2] photutils.readthedocs.io/

try on the Gaia sky position of Gaia-GIC-1 with a general 2D Gaussian PSF model from `photutils`. We converted our PSF flux to Vega magnitudes using zero-point offsets (Wright et al., 2010c). Overall, we find that our derived forced PSF photometry measurements are consistent with the magnitude measurements made using the unTIMELY light curve. Before the onset of the IR outburst, we are unable to draw robust detections of Gaia-GIC-1 in the W_1 and W_2, respectively, due to its faintness and proximity to a nearby source. We applied a customized image subtraction pipeline based on the ZOGY algorithm (De et al., 2020; Zackay et al., 2016) on the unWISE images. The resulting difference images yielded no detections above a 5σ threshold prior to MJD 58,500 in either the W_1 or W_2 bands. We therefore treat all WISE photometry before MJD 58,500 as upper limits in our subsequent analysis, demonstrated in Figure 4.2. We searched through the archival Infrared Astronomical Satellite (IRAS) images and did not find any corresponding source at the location of Gaia-GIC-1, except for one source ~ 0.5 deg away, which is unlikely to be associated with Gaia-GIC-1. The most recent detection between 1-4.5 μm was made by the SPHEREx mission (Doré et al., 2018). Flux measurements were obtained via the IRSA SPHEREx spectrophotometry tool. We convolved the linearly interpolated SPHEREx spectrum with the NEOWISE W_1 and W_2 bandpasses using `pyphot` (Fouesneau, 2025) and averaged the resulting Vega magnitudes. We note that photometry for this source with SPHEREx is challenging due to the large pixel-scale size of the SPHEREx detector (6.2 arcseconds), and with the nearest stellar source 8.2 arcseconds away. While the SPHEREx detection makes it clear that Gaia-GIC-1 remains IR bright, additional follow-up photometry is needed to monitor its brightness in the optical and infrared.

3.3 Spectroscopy

Optical spectroscopy of Gaia-GIC-1 was obtained using the Goodman High Throughput Spectrograph on the 4.1-meter Southern Astrophysical Research (SOAR) telescope. The initial spectrum was acquired on 2024 December 19 as part of the SOAR2024B-026 program. Observations were conducted using the Red Camera with the 400 lines/mm grating (centered at approximately 600 nm), providing a spectral resolution of $R \approx 2000$. The SOAR reductions were done using `PypeIt` (Prochaska et al., 2020). Additional spectroscopic observations were obtained with the Robert Stobie Spectrograph (RSS) on the Southern African Large Telescope (SALT) on 2025 February 22 through a Director's Discretionary Time. Observations utilized the Pg0900 grating with a 1-arcsecond slit in "Faint" gain and "slow" readout modes, yielding a spectral resolution of $R \approx 1700$-2300. Two consecutive 20-minute exposures were acquired to allow for cosmic ray rejection. One acquisition image was taken with the SALTCAM finder in the i-band. Spectroscopic reductions were performed using the RSS reduction pipeline[3], which applies bad pixel replacement, cosmic ray cleaning, CCD gap filling, wavelength calibration, auto gain correction, and flat fielding.

Both optical spectra of Gaia-GIC-1 have a low signal-to-noise ratio (SNR), and are thus difficult to extrapolate any meaningful constraints from either the primary star or any occulting material, likely due to the ongoing large dimming variability Gaia-GIC-1 is experiencing. We fit and divide out the local continuum using a line-free window around the Hα line within

[3]https://astronomers.salt.ac.za/software/rss-pipeline/

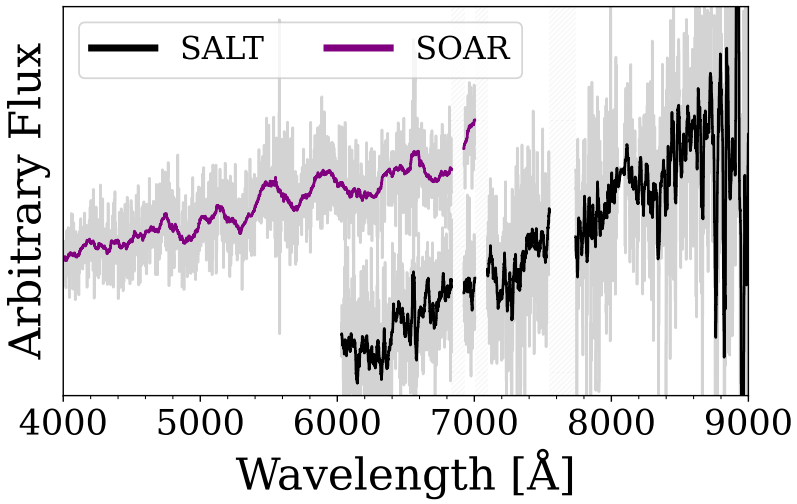


Figure 4.3: Optical spectra of Gaia-GIC-1 obtained with SOAR (purple) and SALT (black) telescopes. Gray lines show the unbinned spectra, while the colored lines show binned versions for clarity. Flux is given in arbitrary units.

±10 Å, and integrate the continuum-normalized spectrum to measure the equivalent-width (EW) and estimate the 1σ EW uncertainty by propagating the scatter from the normalized continuum. Both SALT and SOAR did not meet our 5σ threshold criterion, and we thus report the upper limits of the $|\mathrm{EW}_{H_\alpha}| < 10.3$Å and $|\mathrm{EW}_{H_\alpha}| < 3$Å for SALT and SOAR, respectively. In the SALT spectrum, we identified weak features of the Ca II infrared triplet lines $\lambda\lambda$8498, 8542, and 8662 Å, which would be consistent with photospheric absorption features seen in FGK dwarfs (Chmielewski, 2000).

3.4 Spectral Energy Distribution

We constructed the broadband spectral energy distribution (SED) using available archival data of the star before the onset of the IR brightening event to avoid any contamination from excess IR emission. Our SED compilation incorporates photometric measurements from Gaia BP/G/RP photometry (Gaia Collaboration et al., 2023) and 2MASS HJK_s bands (Skrutskie et al., 2006) presented in Table 4.1. To perform the SED fitting, we used the Modules for Experiments in Stellar Astrophysics (MESA Paxton et al., 2011, 2013, 2015, 2018, 2019) Isochrones & Stellar Tracks using the `isochrones` package (Morton, 2015) to generate synthetic photometry while simultaneously fitting for fundamental stellar parameters, distance, and extinction presented in Figure 4.4 using `MultiNest` (Feroz et al., 2009). We adopt broad uniform priors for all stellar parameters, uniform 16-84th percentile photogeometric distance from Bailer-Jones et al. (2021c), and uniform extinction values from 1-4 mag based on the E(B-V) values reported by Schlegel et al. (1998). Within 30 arc-minutes of Gaia-GIC-1, we identified two open clusters, FSR 1347 and FSR 1352 (Hunt & Reffert, 2024). Though Gaia-GIC-1 is not flagged as a member of either cluster, both clusters have derived isochronal ages between 6-16 Myr, extinctions A_V 3-3.9 mag, and distances 3.29 - 3.38 kpc, consistent within the posterior distribution margin derived for Gaia-GIC-1 from Bailer-Jones et al. (2021c).

The astrometric properties of Gaia-GIC-1 are broadly consistent with the FSR 1347/1352 region, with marginal evidence suggesting a possible cluster membership association with FSR 1352 (see Appendix 1).

To determine whether the available photometry constrains the stellar age, we performed two SED fits using different age priors. First, motivated by the potential association with FSR 1347/1352, we adopted a narrow uniform age prior $\log_{10}(t/\mathrm{yr}) \in [6.8, 7.5]$ based on the clusters' ages, while maintaining our broad distance and A_V priors. Next, we ran a second iteration with a broad age prior $\log_{10}(t/\mathrm{yr}) \in [6.8, 9.5]$ under the scenario that Gaia-GIC-1 is a field star and test if the posterior distribution favors a young age solution. In our broad age prior model, the posterior distribution peaks with a $\log_{10}(t/\mathrm{yr}) \sim 9^{+9.2}_{-8.1}$, while the narrow age model $\log_{10}(t/\mathrm{yr}) \sim 7.1^{+7.2}_{-6.8}$. Comparing our SED fits, we measured a Bayes factor of ~ 1, indicating no preference for either model. While the stellar age cannot be reliably constrained using the available photometry and MIST isochrones alone, the derived stellar parameters remained consistent between both fits. From our fit presented in Figure 4.4, we derive a stellar effective temperature of $T_{\mathrm{eff}} = 6478.8^{+206}_{-292}$ K, metallicity of $[\mathrm{Fe/H}] = -0.2^{+0.5}_{-0.4}$ dex, and extinction of $A_V = 3.8^{+0.1}_{-0.2}$ mag. From this fit, we assume a radius of $R_\star = 1.7^{+0.3}_{-0.2}\ R_\odot$, mass of $M_\star = 1.3^{+0.2}_{-0.2}\ M_\odot$, distance $d = 3551^{+699}_{-396}$ pc, surface gravity $\log g = 4.1^{+0.1}_{-0.1}$ cgs ([10.5281/zenodo.17982426]https://doi.org/10.5281/zenodo.17982426). Based on the SED posteriors, we interpret Gaia-GIC-1 as a mid-F5 star.

Survey/Band	Magnitude	Magnitude Error
2MASS-H	15.45	0.02
2MASS-J	16.19	0.09
2MASS-Ks[4]	15.41	0.21
Gaia DR2 - BP	19.68	0.06
Gaia DR2 - G	18.79	0.002
Gaia DR2 - RP	17.71	0.02

Table 4.1: Compiled broadband median photometry of Gaia-GIC-1 outside the dimming events before December 2011 or after January 2019. We assume that the intrinsic stellar SED is unchanged before or after the dimming event.

4 Properties

4.1 Light Curve Properties

From the beginning of the *Gaia* coverage until approximately MJD $\lesssim$ 58 300 (roughly 2014–2017), the source remained in a quiescent state at $G \approx 18.8$ mag. At least three distinct optical dips are present in Figure 4.2 between epochs MJD $\sim$ 57 000 and MJD $\sim$ 58 800 with average depth of $\sim$0.4 mag (25% reduction in flux) and average timescale of 200 days, though we note that curiously the third dip at epoch $\sim$58500 was not as deep as the previous dips. While sparse, archival i-band data from DECaPS and SkyMapper DR4 captured one epoch during the first optical dimming event. Notably, during the first dimming event, the Gaia-G

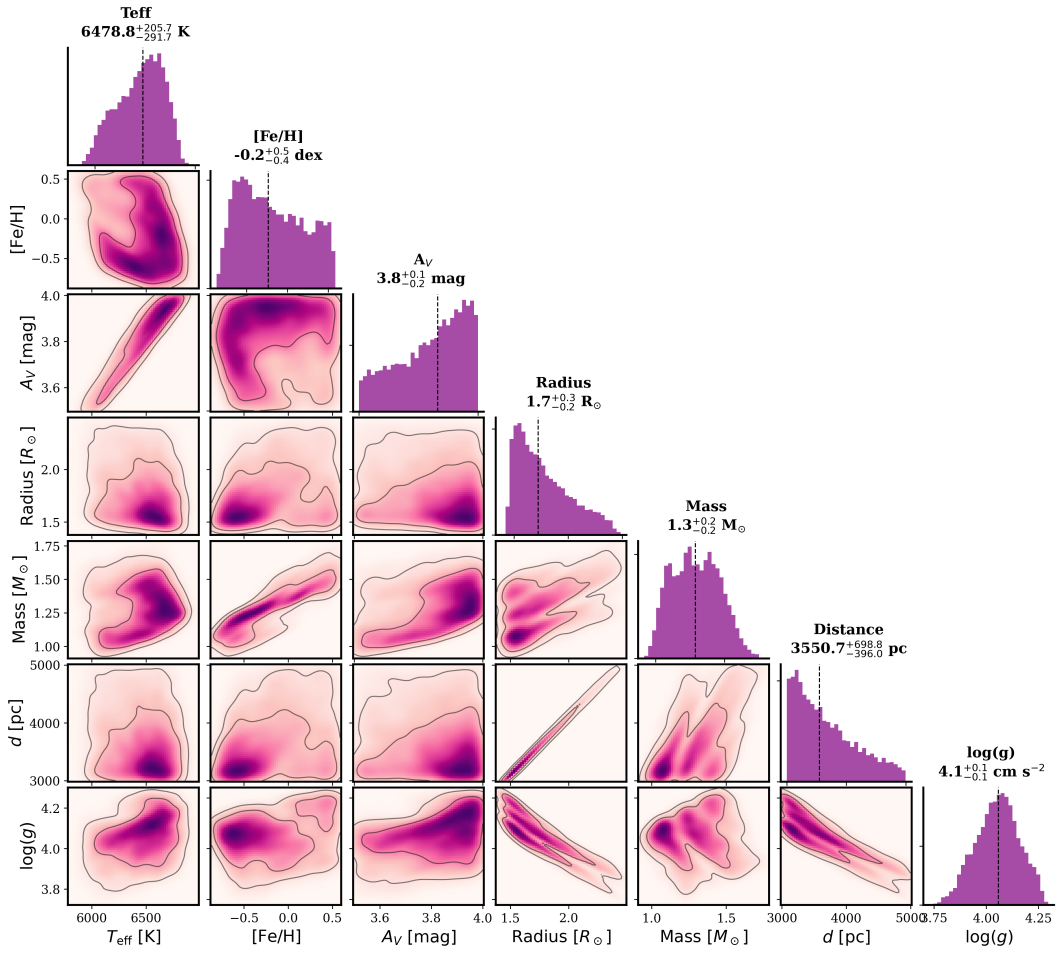


Figure 4.4: Corner plot showing posterior distributions from MIST fitting to pre-eclipse photometry of Gaia-GIC-1. Diagonal panels show marginalized posteriors for Teff, [Fe/H], A_V, radius, mass, distance, and log g. The off-diagonal panels show parameter correlations with 68% and 95% confidence contours.

band dropped by 0.4 mag, while the i-band remained nearly constant, producing a Δ(G-i)$\sim$0.8 mag, which could hint that the obscuring material may be wavelength-dependent. Starting near MJD $\sim$ 58 700, the system underwent rapid fading and variability that has been ongoing for at least 4 years, reaching $G \approx 20.3$ mag just before the automated GPSA alert trigger. The average fading rate during this interval is ~ 0.4 mag yr^{-1}. Following the alert epoch (MJD $\gtrsim$ 59 000; late 2020 onward), the star has remained faint in optical wavelengths, fluctuating between $G \approx 19.8$ and at least > 20.8 mag. Unlike the earlier monotonic behavior, the post-alert light curve is dominated by irregular variations, with no sign of a sustained re-brightening trend across the current Gaia baseline; however, higher-cadence optical monitoring is required to confirm.

The optical evolution is strikingly anti-correlated with the IR behavior displayed in the bottom panel of Figure 4.2, where W_1 and W_2 brighten while the Gaia-G magnitude fades. However, the IR flux has exhibited a characteristic plateau since 2019. The recent SPHEREx detection has also confirmed that Gaia-GIC-1 is currently bright in the IR. Optical dimming coupled with infrared brightening typically indicates newly formed circumstellar dust obscuring reprocessed thermal IR emission. To measure the dust temperature, we fit a modified blackbody to the epochal WISE photometry after subtracting the stellar contribution from the stellar parameters derived in Section 3.4. We use the following modified blackbody:

$$S_\lambda \propto \left(\frac{\lambda_0}{\lambda}\right)^\beta B_\lambda(T_d), \tag{4.1}$$

where λ_0 is the wavelength at which the optical depth is unity, and β is the spectral emissivity index. Since far-IR observations of Gaia-GIC-1 are currently unavailable to measure the emissivity index directly, we adopt a β value of 0.9 based on the grain-size distribution index in debris disks undergoing collisional cascades (Steele et al., 2016), and set λ_0=100μm. We simultaneously constrain the dust temperature and radius using MCMC. Figure **??** shows the blackbody fits (top) and dust temperature evolution (bottom). We measure the median posterior distribution dust temperature, which has plateaued at T_{dust}=900$\pm$24 K with a characteristic radius of 0.2$\pm$0.04 AU.

4.2 Periodicity

We computed the Lomb-Scargle Periodogram (**??**) on the Gaia-G light curve, before and after the onset of the near-IR excess, separated at the epoch of 2020-09-12, shown in Figure 4.7. We find a significant periodic signal at the 380.5-day interval above the 1% False Alarm Probability (FAP) interval, which diminishes during the IR bright phase, and is consistent with the optical Gaia-G light curve in the bottom panel of Figure 4.7. The FAP intervals were measured using 1,000 bootstrap samples with replacement on the flux values while keeping the observed times. Using our estimated stellar mass of 1.3 $M_\odot$ and the measured 380.5-day orbital period, we infer that the dusty material is at a semi-major axis of 1.1 AU. At MJD $\sim$ 58 790 with the onset of the IR-excess feature, the Gaia-G light curve shows more erratic variability, with no clear signs of periodicity. To test this further, we computed the quasi-periodicity metric (Q) (Cody & Hillenbrand, 2018b; Cody et al., 2014a) based on the top 5 highest peaks in the post-IR periodogram in Figure 4.7 and in all tested periods, we

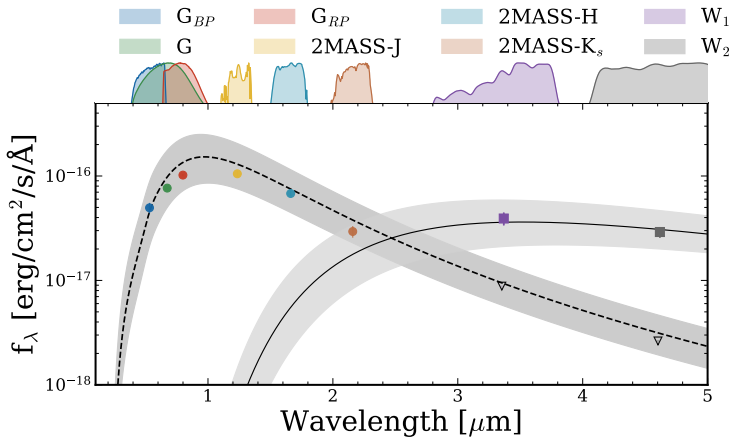


Figure 4.5: Spectral energy distribution of Gaia-GIC-1 spanning optical to mid-infrared wavelengths. The black dashed line shows the stellar photosphere model derived from MIST isochrone fitting, with the light gray shaded region indicating the associated uncertainty, and the upside-down triangles denote the 3σ upper limits. The solid black line represents a modified blackbody fit to the infrared excess emission after subtracting the photospheric contribution.

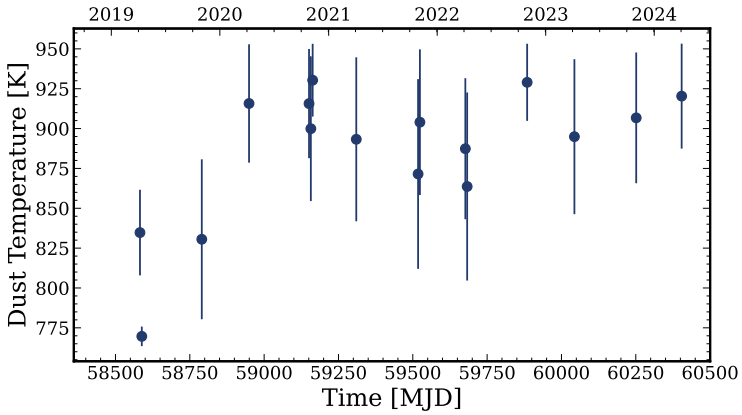


Figure 4.6: Spectral energy distribution of Gaia-GIC-1 spanning optical to mid-infrared wavelengths. The black dashed line shows the stellar photosphere model derived from MIST isochrone fitting, with the light gray shaded region indicating the associated uncertainty, and the upside-down triangles denote the 3σ upper limits. The solid black line represents a modified blackbody fit to the infrared excess emission after subtracting the photospheric contribution.

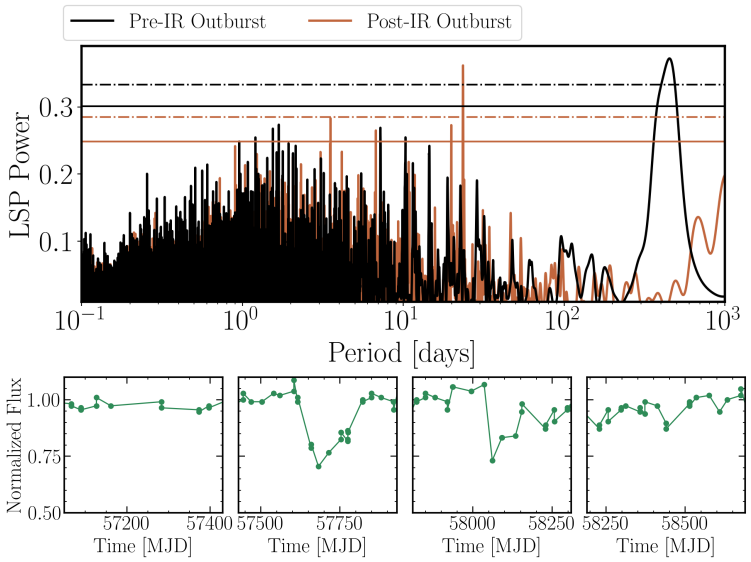


Figure 4.7: Top panel displays the Lomb-Scargle Periodogram of the optical Gaia light curve of Gaia-GIC-1. The dashed and solid lines, bottom to top, are the 5% and 1% False Alarm Probability levels. The bottom panel displays the normalized flux light curve of Gaia-GIC-1 at a 380.5-day interval.

found high Q>0.8 values, indicating that the source is likely experiencing aperiodic behavior during the IR-bright phase.

5 Discussion

5.1 Planetary Collision Impact Scenario

Our current interpretation of the available data is that Gaia-GIC-1 resembles a transiting planetary collision afterglow. There are only a handful of known stellar variables associated with anti-correlated near-IR and optical properties, a typical signature of newly generated circumstellar dust. In such instances, the freshly produced dust grains from the collisional debris absorb and scatter in the optical wavelengths, while re-radiating thermally in the infrared (Wyatt & Jackson, 2016a). The temporal evolution of photometric evolution in Gaia-GIC-1 suggests we may be witnessing the dynamic clearing and geometric evolution of impact-generated debris and the host star. Gaia-GIC-1 most clearly resembles the light curve properties of ASASSN-21qj (Kenworthy et al., 2023b; Marshall et al., 2023b), with both systems exhibiting a striking transition from optical quiescent to irregular optical variability accompanied by the brightening in the near-IR. However, we note there are several distinguishing factors of this system. For instance, Gaia-GIC-1 shows three quasi-periodic optical dips before the onset of the irregular variability, which provide a strong constraint on the period of the transiting material to an equivalent semi-major axis of ∼1.1 AU. Such dusty occultation before the onset of the near-IR excess has been observed before, such as the case of HD 161991 (Su et al., 2022b), and other analog systems (Moór et al., 2022). However,

some alternative theories suggest that such complex variables could also be consistent with the breakup of exocometary bodies (Marshall et al., 2023b). The large-amplitude and sudden increase in the near-IR flux points to a sudden large generation of a warm circumstellar disk in the inner region.

Although the MIST age posteriors do not provide strong constraints on the stellar age, Gaia-GIC-1 displays several indicators that suggest a young age with the current available archival data. We examined the 2MASS color-color locus of Gaia-GIC-1 using its $(H - K_s)$ and $(H - J)$ colors. The target lies within 1σ of both the weak-line T-Tauri star (WTTS) and main-sequence loci, while appearing inconsistent with the classical T-Tauri star (CTTS) locus (Gras-Velázquez & Ray, 2005; Meyer et al., 1997). While the 2MASS colors alone cannot definitively distinguish a WTTS or main-sequence classification, disfavoring a CTTS classification suggests an age of $>$ 10Myr. Our tentative WTTS classification would be consistent with the ages of candidate host clusters FSR 1352/1347, which are generally above 10 Myr and are compatible with our $\mathrm{EW}_{H\alpha}$ limits. Population-level statistics of protoplanetary disks suggest that the disk fraction among low-mass young stars drops to a few percent by >10 Myr in the 3.4-4.6 μm wavelength (Ribas et al., 2015). Given the tentative constraints and clues on the stellar age, a planetary collision would be anticipated at this phase (Wyatt & Jackson, 2016a). At the present faint and highly irregular optical variability state, follow-up observations make it challenging to constrain any age diagnostic (i.e., joint constraint with SED and gyrochronological (Angus et al., 2019) or Li I 6708 Å abundance (Jeffries et al., 2023). Such constraints would likely only become feasible if the star returns to its quiescent brightness.

To quantify the debris mass produced by the proposed collision, we estimate the total dust mass based on the IR excess flux. From section 4, we adopt an average dust temperature of 900 Kelvin, and a total cross-sectional emitting area of 0.13 AU^2. Assuming the emission is due to small dust grains generated in a collisional cascade, with bulk density 3 g cm^{-3} and a grain size distribution of 1 cm - 1 μm, we estimate the total emitting mass to be on the order of $5{\times}10^{21}$ kg. Our derived mass estimate is also consistent with the W_2 excess flux, which yields a similar cross-section of 0.08 AU^2. We caution that this must be a conservative minimum mass estimate since our distance error is on the order of $\sim$1 kpc, and the near-IR is probing the heated material within only a few AU (Dullemond & Monnier, 2010). Our estimated dust mass is on the mass scale of a small icy moon, such as that of Enceladus (Rappaport et al., 2007), which likely indicates that the initial colliding bodies should be considerably larger, though this could be estimated more precisely through collisional simulations (Kenworthy et al., 2023b).

The observed transit properties of Gaia-GIC-1 appear to deviate from an edge-on circular orbit. In Figure 4.8, we show the anticipated clump radius assuming an edge-on circular orbit capable of producing the observed optical dips. The initial Gaia-G dips have depths of 25% with characteristic durations of 200 days. At the constrained semi-major axis of 1.1 AU, this duration would imply a transiting dust cloud radius of $5 \times 10^2\ R_\odot$, requiring a substantially larger emitting cross-sectional area than the derived 0.13 AU^2. Conversely, if we adopt the measured cross-sectional area of 0.13 AU^2 at 1.1 AU, the implied transit duration would be only 26 days, which would be inconsistent with observations. We note that the degeneracy between semi-major axis, transit duration, and emitting area likely arises from an elongated dust structure, further supported by the highly asymmetric dimming profiles in the Gaia-G

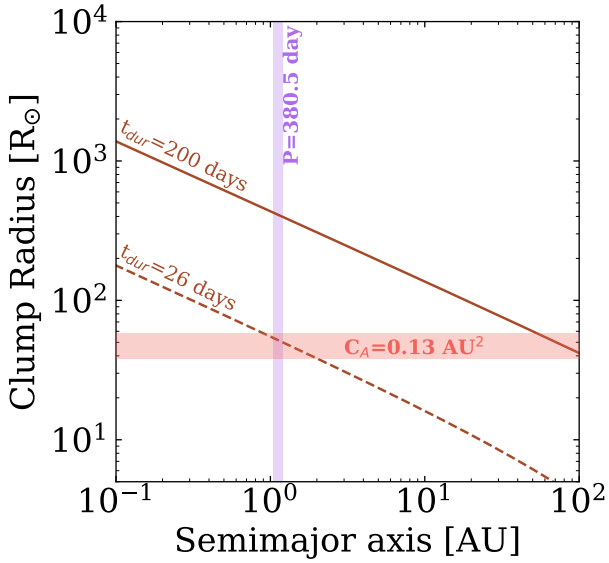


Figure 4.8: Radius of an occulting clump as a function of semi-major axis. Brown lines show the clump size required to match the observed transit durations (solid: 200 d; dashed: 26 d) for a circular, central transit around a $1.3 M_\odot$, $1.7\ R_\odot$ star. The horizontal pink line indicates the equivalent clump size implied by a total occulting cross-section of 0.13 AU^2. The vertical purple band shows the semi-major axis corresponding to an orbital period of 380.5 days, corresponding to a ∼1.1 AU orbit.

photometry. We constrain the transverse velocity of the occulting material by measuring flux slopes during ingress and egress, assuming the occultations are caused by a sharp dust edge (Kennedy et al., 2017). We measure the steepest flux gradient with a transverse velocity of 3.0 ± 0.4 km s^{-1}, which is substantially lower than the anticipated ∼30 km s^{-1} Keplerian velocity at 1.1 AU for a circular orbit. One scenario this could be consistent with is the debris being on a highly eccentric orbit, where the orbital velocity material is minimized near the apoapsis. Such orbital geometry could explain both the extended transit durations and the complex quasi-periodic behavior observed in Gaia-GIC-1. Alternatively, the extended transit durations and asymmetric dip profiles could arise from a gradual distribution of optical depth within the dust cloud itself, rather than being dominated by the physical velocity of the debris, which would be more consistent with the observed dimming profiles. Qualitatively, this scenario suggests an evolving, shearing debris field in which impact ejecta with high velocity dispersion will contribute to a range of semi-major axes a, as predicted by simulations (Kenyon & Bromley, 2005; Wyatt & Jackson, 2016a).

5.2 Alternative Scenarios

Tidally disrupted bodies, including gas giants (Li et al., 2010; Oberst et al., 2017), planets (Rappaport et al., 2012b; Vanderburg et al., 2015b), and exocomets (Rappaport et al., 2018c), can reach separations with their host stars that can facilitate either ongoing tidal stripping and Roche lobe overflow, or complete breakup near the Roche limit, by producing strongly asymmetric dusty transits (e.g., Hon et al. (2025)). We explore whether the Gaia-

GIC-1 light curve is consistent with tidal disruption of a planetesimal generating warm debris; however, the current available data suggest this scenario is unlikely. At the given constrained mass and radius of the primary star, the Roche limit for a comet-like body ($\rho \sim 0.5\,\mathrm{g\,cm^{-3}}$) is ∼0.01 AU, while an Earth-like planet ($\rho \sim 5.5\,\mathrm{g\,cm^{-3}}$) would have an even smaller Roche limit of ∼0.004AU. In the scenario of circularly orbiting dusty material resulting from the disruption of a comet-like body, if the material is near the Roche limit, this would be inconsistent with the initial periodic occultations measured to be at ∼1.1 AU semi-major axis. Similarly, assuming the occulting cross-sectional area of 0.13 AU^2 and stellar radius, the velocity at the Roche limit ∼352 km sec^{-1} would imply a transit duration of ∼2 days, which is in stark contrast with the individual 200 day transits we find prior to the onset of the IR-excess nor the estimated 3 km sec^{-1} minimum velocity estimated via the steepest flux gradient. For a highly eccentric orbit (e=0.9) at the Roche limit, a comet-like body would have periapsis and apoapsis velocities of ∼5,000 km sec^{-1} and ∼85 km sec^{-1}, respectively. The resulting transiting timescales would be severely undersampled by the 21-day average Gaia cadence, making this scenario difficult to constrain. Thus, it remains plausible that if the material is near the Roche limit on highly elliptical orbits, and would require higher photometric monitoring to test more concretely.

Alternative pathways to produce near-IR excess have also been previously proposed, including gravitational stirring of a dense planetesimal belt by an unseen planet or low-mass companion, and delayed orbital instabilities can trigger collisions, yielding episodic dust production (Clement et al., 2020; Rieke et al., 2021b). We did not find any archival data to suggest that Gaia-GIC-1 is a wide binary system that could drive such orbital instabilities. For example, we examined the Gaia RUWE score to be ∼1, and the nearby stellar source (Gaia DR3 5593847977064283520) is unlikely to be associated with Gaia-GIC-1, as they are 8.3 arcseconds apart and have a large physical separation.

Canonical T-Tauri stellar variables have also been found to have irregular variability in the optical and near-IR (Cody et al., 2014c). Though typically, these sources are known to have typical signatures or IR excess due to the presence of a circumstellar disk, signatures of their youth in an optical spectrum, such as signs of ongoing extreme accretion events through the presence of Hα emission (Hillenbrand et al., 2025). Our spectroscopic Hα EW upper limits would also suggest the unlikely scenario of dealing with a CTT star, though, within our detection limits, a more mature WTT star is plausible with typical $\mathrm{EW}_{H_\alpha} < 10$Å (Barentsen et al., 2011). Given our tentative optical spectrum, we rule out the scenario of a typical Class I/II YSO variability, since we did not find any such emission lines. Systematic searches for dipper variables among both young stellar objects (Hillenbrand et al., 2022b) and main-sequence stars (Tzanidakis et al., 2025) have revealed diverse dimming phenomenologies. However, the combination of periodic and asymmetric optical dips, anti-correlated near-IR brightening, and lack of persistent IR excess in Gaia-GIC-1 distinguishes it from typical dipper populations, which generally lack significant IR variability and excess.

6 Conclusion

We report the discovery of Gaia-GIC-1 (Gaia20ehk), an ongoing optical dimming and low-luminosity infrared stellar transient, which we hypothesize to be undergoing planetesimal

collision afterglow seen by Gaia. Based on the constructed archival SED of the source before the irregular dimming events, we constrain the star to be a young F5-type star. Optical follow-up spectroscopy reveals a nearly featureless spectrum, which is likely due to the low SNR and high stellar variability obscured by dust, though we note that no prominent features of stellar accretion were found. Analysis of the Gaia-G optical light curve reveals a quasi-periodic optical dip with ∼25% flux amplitude and timescale of 200 days with a period of ∼380.5 days, implying an orbital semi-major axis of 1.1 AU. Based on the available photometry, we derive a conservative dust mass of 4×10^{20} kg, and dust temperature of 900 Kelvin, and suggest that the newly generated circumstellar material is likely from the collision of two planetesimals. Continued optical and near-IR photometry is strongly encouraged, as recent photometric optical-to-near-IR photometric detections show the stellar source to still exhibit strong variability.

Continued infrared monitoring of Gaia-GIC-1 with the exceptional sensitivity and broad wavelength coverage of *JWST* is essential for disentangling the origin of its mid-IR excess and tracing the thermal evolution of any post-impact debris. Multi-epoch MIRI photometry and low-resolution spectroscopy can pin down the temperature–luminosity decay curve of the warm dust, distinguishing a rapidly cooling impact afterglow from passively heated circumstellar material, and possibly resolve key solid-state features such as the 9–12μm silicate features that could be even more compelling evidence for a giant impact scenario (e.g., Su et al. (2025)). Integrating time-resolved *JWST* observations with existing optical and NEOWISE light curves will allow construction of a self-consistent model of the collision geometry, debris mass, and clearing timescales. Thanks to the Gaia Photometric Science Alerts, we have likely found the first planetesimal impact seen by Gaia and other space-based observatories due to its all-sky photometric coverage over the last decade. Subsequent discoveries can also be driven by the Vera C. Rubin Observatory's Legacy Survey of Space and Time (LSST) (Ivezić et al., 2019).

7 Acknowledgments

The authors thank the anonymous referee for their helpful comments and suggestions that improved the quality of this work. AT acknowledges useful conversations with Eric Gaidos, Lynne Hillenbrand, and Nick Tusay for understanding the origins of the following system. We thank Chung-Uk Lee for obtaining follow-up photometry and Kishalay De for helping us with the unWISE image differencing analysis. The authors acknowledge support from the Institute for Data Intensive Research in Astrophysics & Cosmology (DiRAC) in the Department of Astronomy at the University of Washington. The DiRAC Institute is supported through generous gifts from the Charles and Lisa Simonyi Fund for Arts and Sciences and the Washington Research Foundation. The authors would also like to acknowledge the generous support from Breakthrough Listen. The Breakthrough Prize Foundation funds the Breakthrough Initiatives, which manage Breakthrough Listen. This publication makes use of data products from the Wide-field Infrared Survey Explorer and NASA/IPAC Infrared Science Archive, which is a joint project of the University of California, Los Angeles, and the Jet Propulsion Laboratory/California Institute of Technology, funded by the National Aeronautics and Space Administration. This publication makes use of data products from the

Spectro-Photometer for the History of the Universe, Epoch of Reionization and Ices Explorer (SPHEREx), which is a joint project of the Jet Propulsion Laboratory and the California Institute of Technology, and is funded by the National Aeronautics and Space Administration. This research has made use of publicly available data (https://kmtnet.kasi.re.kr/ulens/) from the KMTNet system operated by the Korea Astronomy and Space Science Institute (KASI) at three host sites of CTIO in Chile, SAAO in South Africa, and SSO in Australia. Data transfer from the host site to KASI was supported by the Korea Research Environment Open NETwork (KREONET).

1 Cluster Membership Probability

We performed a Gaussian Mixture Model (GMM) analysis to assess the cluster membership probability of Gaia-GIC-1 of two identified open clusters within <30-arcminutes. We constructed a training set consisting of flagged members of FSR 1347 and FSR 1352 from Gaia DR3 (Hunt & Reffert, 2024), along with field stars within the same sky footprint. We initialized our GMM on K=3 clusters, and trained it on the three-dimensional astrometry available from Gaia DR3, including parallax and the proper motions ($\mu_\alpha \cos(\delta)$, μ_δ, ω). To account for measurement uncertainties, we employed a Monte Carlo approach, drawing 1000 realizations from the astrometric parameters for Gaia-GIC-1 distributions centered on the measured values with widths of 2σ of the reported Gaia DR3 uncertainties. For each realization, we computed the posterior probability of membership of each component. We found a median membership probability of P(FSR 1352)=0.6, compared to P(Field)=0.38 and P(FSR 1347)≈0, suggesting marginal evidence that Gaia-GIC-1 might be a member of FSR 1352, though we caution that this should be done more concretely if radial velocities are obtained for Gaia-GIC-1 and both clusters. We present our diagnostic plots in Figure .9.

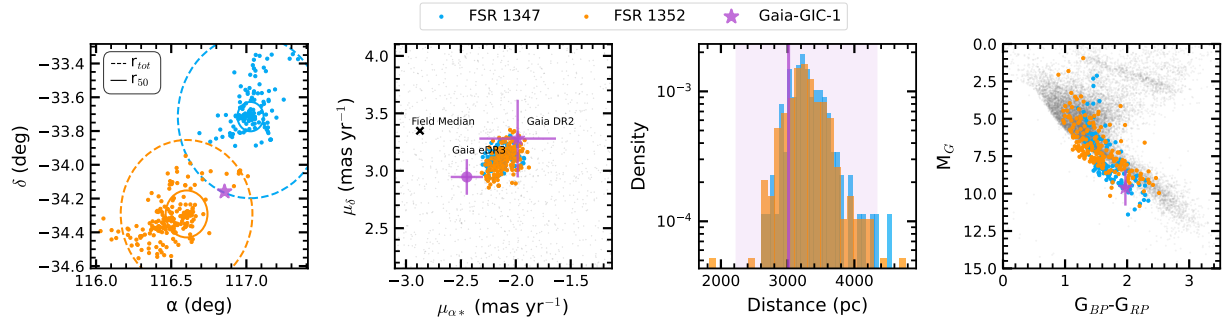


Figure .9: Astrometric and photometric properties of FSR 1347, FSR 1352, and Gaia-GIC-1 (magenta star). (**Left**): Sky distribution of the two open clusters, where the solid lines represent the 50% cluster membership and dashed lines the total cluster radius (Hunt & Reffert, 2024). (**Center Left**) Proper motions of the identified clusters, including the reported 2D proper motions, are reported in both Gaia DR2 and Gaia DR3. For reference, we also include the field median marked. (**Center Right**) Probability distribution of the reported cluster member distances and Gaia-GIC-1 from Bailer-Jones et al. (2021c). (**Right**) Extinction-corrected Gaia DR3 color-magnitude diagram including the open cluster members and the position of Gaia-GIC-1.

CHAPTER A

CONCLUSION

The turning of the circle,
which rises and falls,
times high, times low,
and times we enter the depths

– *Vikentios Kornaros, Ερωτόκριτος*

In the preceding chapters, I presented three new classes of rare stellar variables driven by circumstellar dust: (i) main-sequence dipper stars, identified through the first large-scale systematic search; (ii) Gaia17bpp, a record-setting disk occultation producing a ∼7-year transit around an evolved star, and (iii) Gaia-GIC-1, a giant impact planetesimal candidate. Each discovered system represents a physically distinct regime of circumstellar dust across circumstellar environments and age, while all three classes share a common observational signature: prolonged and complex dimming events that have only become recoverable at scale through the advent of time-domain sky surveys. In many cases presented in this thesis, these rare stellar occultations are uncovered through archival searches, long after the underlying astrophysics has unfolded. For example, in Chapter 3, I presented the discovery of Gaia17bpp – classified as an ultra-long eclipsing binary enshrouded by a large disk– which was recovered through a large collation of archival data. By the time the system was identified and characterized, the transit was already over. The rich astrophysics behind, for instance, the Gaia17bpp occultation reveals that the geometry, nature of the companion, and dynamics of the system have to be solely reconstructed based on the archival data alone. While the archival mode of discovery is powerful, it also has its limits: understanding the full physics of these systems requires discovery in real-time, with the follow-up infrastructure to respond across wavelength domains before the dust evolves or fades. The broader goal motivating this work is to build large enough populations of rare circumstellar dust-driven variables where eventually distribution on properties such as timescales and amplitudes across many wavelengths can be fully mapped. Such parameter space will ultimately allow us to distinguish between formation mechanisms, constrain occurrence rates, and connect these rare events to the broader context of stellar and planetary evolution.

1 Future Work

Throughout the duration of my Ph.D. at the University of Washington, many of the systematic searches carried out in this dissertation, together with valuable discussion and follow-up efforts with wonderful collaborators, led to the identification of several new and rare dippers driven by the themes discussed thus far. The following presented systems reinforce the broader picture that circumstellar dimming phenomena are both diverse and still far from fully mapped. Below, I highlight one particular interesting example that represents a promising avenue for future investigations.

1.1 Gaia-GIC-2: Planet Collision with Enhanced Accretion?

In 2021, the Gaia Photometric Science Alerts (Hodgkin et al., 2021a) pipeline reported Gaia21ajl (Hodgkin et al., 2021c), a large-amplitude optical dimming event from an otherwise quiescent star ($r \sim 13.5$ mag). Subsequent photometric monitoring from ground- and space-based optical time-domain surveys following the 2021 Gaia alert reveals that Gaia21ajl undergoes irregular dimming events reaching $r = 15.3$ mag on timescales of weeks, with a stochastic evolving dip morphology. Photometry from the NEOWISE unTIMELY (Meisner et al., 2023a; Su et al., 2022a; Tzanidakis & Davenport, 2026) W_1 and W_2 bandpasses has revealed, since early 2021, that the source has undergone a slow and steady ∼20 mJy IR outburst coincident with the onset of the irregular optical dips. Figure A.1 presents the collated light curve of Gaia21ajl. The onset of irregular optical dimming variability anti-correlated with low-luminosity IR outbursts has been proposed to be due to freshly generated debris likely resulting from the recent afterglow of a giant impact between two planetesimals (Kenworthy et al., 2023a). Current investigation of Gaia21ajl's properties has confirmed it to be a known member of the open cluster UBC 159 (see Figure A.2, left) with a stellar age of ≈ 14 Myr (Otto et al., 2026; Perren et al., 2023). If a true member, then at its current stellar age, it would be precisely the epoch when terrestrial planet formation and giant impact activity are predicted (Quintana et al., 2016c). At the current constrained age, accretion from a residual protoplanetary disk may still be present (Donati et al., 2024), raising the critical question of whether the observed photometric variability traces impact-generated debris alone, or whether it also reflects an *enhanced accretion episode* driven by a recent collision or represents a new class of rare YSO. We measured the Hα pseudo-equivalent width (pEW) from the low-resolution Gaia XP spectrum ($R \sim 50$), nominally placing Gaia21ajl near or above the expected accretion detection threshold for a 14 Myr star (Figure A.2, right). Converting the pEW to mass accretion rate $\dot{M}_{\rm acc}$ via the empirical $L_{\rm H\alpha}$–$L_{\rm acc}$ relation (e.g., Delfini et al., 2025; Shridharan et al., 2022) yields an accretion rate that either exceeds the typical mass accretion rates by an order of magnitude, or is average within its stellar age (Caratti o Garatti et al., 2012). However, it is suggested that Gaia's XP resolution of genuine accretion emission features is difficult to resolve (Creevey et al., 2023). This degeneracy cannot be broken without medium-resolution optical spectroscopy. Beyond Hα, the proposed wavelength coverage will also be able to identify, if any, fast-moving post-collision circumstellar dust or gas in the inner system analogous to exocometary absorption detections in young debris disk systems (e.g., Kiefer et al., 2014). Without prompt follow-up, transient circumstellar features can disperse on timescales of months under radiative depletion, leaving Gaia21ajl

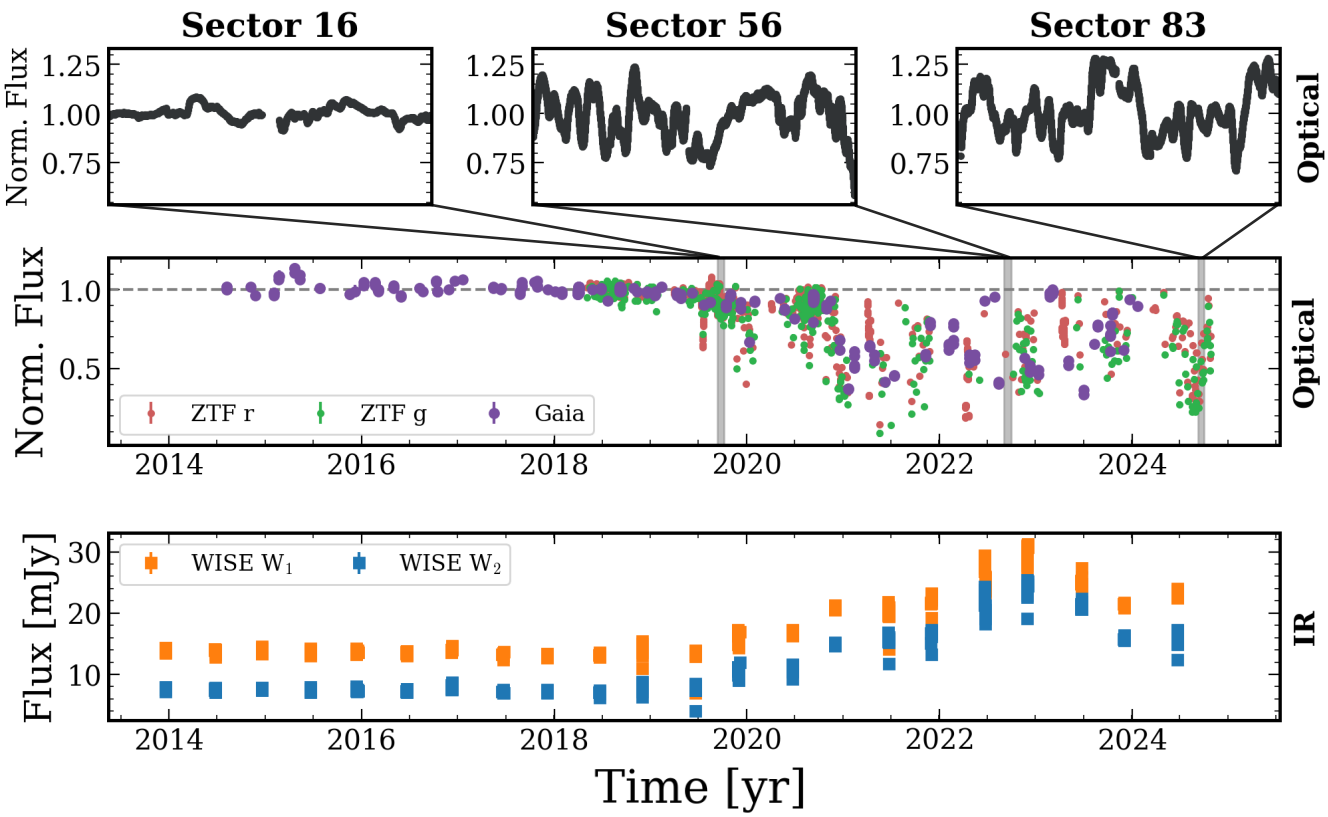


Figure A.1: Top Transiting Exoplanet Survey Satellite (TESS) 2-minute cadence photometry. **Middle**: Compiled ground-based photometry from Gaia-G (via Gaia Alerts) and the Zwicky Transient Facility (ZTF) survey. Highlighted in gray are the observed TESS sector times. **Bottom** compiled 10-year W_1 (3.3μm) and W_2(4.6μm) unWISE photometry showing a quiescent source undergoing a ∼20 mJy outburst during the irregular variability window seen by Gaia, TESS, and ZTF.

spectroscopically featureless at optical wavelengths and rendering the collision hypothesis untestable. Gaia21ajl therefore presents a rare opportunity to spectroscopically confirm a giant impact candidate, and to determine directly whether a planetary collision can drive a heightened accretion response.

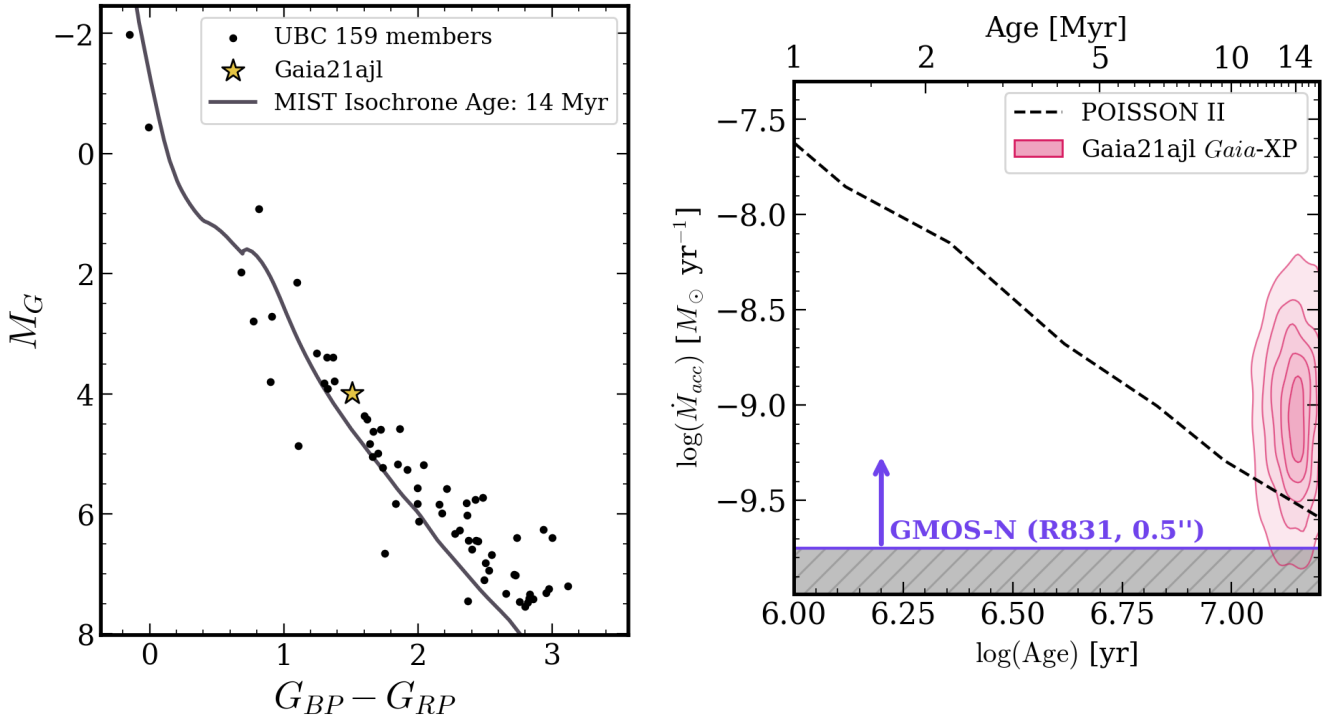


Figure A.2: (Left) Gaia DR3 color-magnitude diagram showing confirmed members of the open cluster UBC 159 (black points) overplotted with the MIST isochrone (Dotter, 2016) at 14 Myr (gray line). Gaia21ajl (gold star) lies squarely on the cluster main-sequence. **(Right)** Mass accretion rate ($\dot{M}_{\rm acc}$) as a function of stellar age. The red contours show the preliminary $\dot{M}_{\rm acc}$ estimate for Gaia21ajl derived from the Gaia XP pEW measurement, and the dashed black line shows the nominal POISSON-II accretion timescale model. The horizontal purple line marks the GMOS-N (R831, 0.5") detection threshold; any accretion signal above this limit will aid in constraining the mass accretion rate more confidently.

2 Surveys and Data of the Future

2.1 The Rubin Observatory as A Real-Time Discovery Engine

The Legacy Survey of Space and Time (LSST) on the Vera C. Rubin Observatory will fill out an enormous and highly complementary phase space for studying billions of variable stars over its 10-year-long Southern sky survey. On average, each star will have ∼100 total epochs of data per year across 6 broadband filters (*ugrizy*) with an average $\sim 1\%$ photometric accuracy (Ivezić et al., 2019), down to $\lesssim$24 mag. In the context of stellar variables, LSST will undoubtedly be a discovery engine capable of discovering in real-time sources that are undergoing dramatic flux changes, such as dips. Each night, the LSST real-time Prompt Processing pipelines are expected to deliver $\sim 10^7$ public alerts to the community via image differencing, with alert packets issued within 60 seconds of shutter closure following each visit (Findeisen et al., 2026; Graham et al., 2024). It is worth noting that no individual science user will subscribe to the LSST alert stream directly. Instead, the full alert stream will be served by community alert brokers: ALeRCE, AMPEL, ANTARES, Babamul, Fink, Lasair, and Pitt-Google (Bellm et al., 2020; NSF-DOE Vera C. Rubin Observatory, 2026a), which cross-match, filter, and photometrically classify incoming alerts such that users can identify and trigger follow-up on sources of interest. Because most alert brokers' classification schemes have been trained and validated on explosive transients (Förster et al., 2021; Sánchez-Sáez et al., 2021), recovering slow, aperiodic dimming events discussed in this dissertation will require custom-built alert filters specifically aimed at discovering events with sustained negative flux excursions unlike typical variable stars. However, a residual concern for the longest-duration events is that difference imaging measures change relative to a co-added static-sky template, which is typically constructed during the annual Data Releases (NSF-DOE Vera C. Rubin Observatory, 2026b). An occultation persisting for years or a slowly varying stellar source, such as Gaia17bpp and its analogues, may therefore have part of its dimmed state absorbed into the newly generated template images, and thus risk the possibility of no alert distribution for some of these rare gems. Recovering some of these systems may therefore require querying the Prompt Product Database and annual data-release light curves directly, to introduce new strategies to discover such unique systems.

The LSST will place dimming events driven by circumstellar dust into a much broader population context. Its long temporal baseline and across six broadband filters will make it possible to measure the demographics, color behavior, and diversity of the discussed rare stellar variables at scale (Hu et al., 2026; Martínez-Galarza et al., 2021). In many of the rare dipper classes explored in this thesis, the light curves follow a common photometric pattern: a bright, quiescent baseline followed by a sudden drop in flux. Complementary surveys that are sensitive to sources brighter than < 16 mag can define the photometric baseline to quiescent stars. Then, when a dusty circumstellar occultation drives the source to fainter magnitudes, LSST can deliver precise *ugrizy* photometry through the dips, in a regime that is currently inaccessible to most other surveys. Figure A.3 demonstrates this in the case of a hypothetical long-timescale dipper event. While the source may be saturated in the LSST footprint during quiescence, LSST becomes highly informative once the system fades. During its dimming phase, LSST can constrain the dip duration and color evolution, which in turn can be used to infer the characteristic timescales of the variability and the properties of the occulting

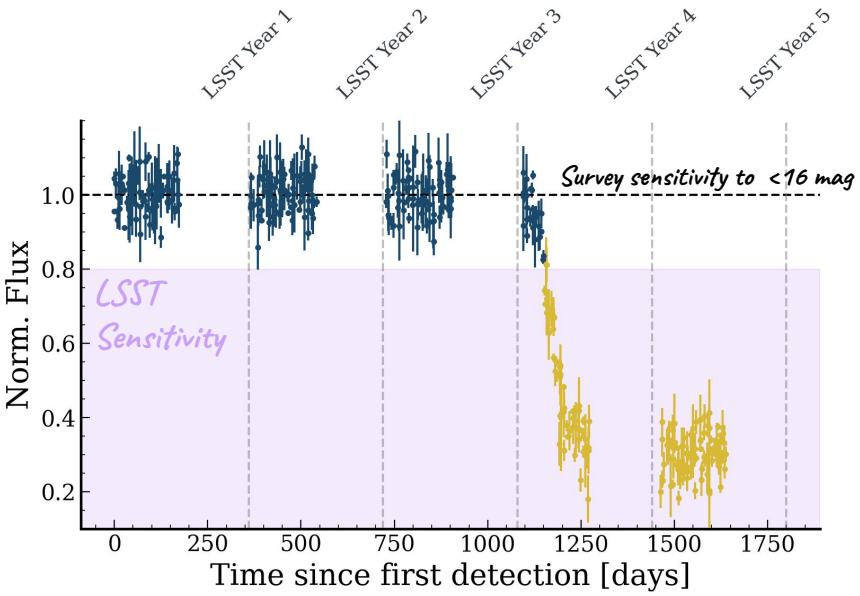


Figure A.3: Conceptual light curve of a long-timescale circumstellar dimming event, showing how complementary survey regimes constrain different phases of the variability. In the bright and quiescent state, the source lives above the effective Rubin/LSST sensitivity window due to saturation, while other shallower wide-field surveys can establish the pre-dimming photometric baseline. After the onset of a deep complex fading event (not that different from what has been explored in this thesis), the source enters a brightness regime where Rubin can deliver precision *ugrizy* photometric monitoring.

dust. Rubin alert products are also planned to include pre-computed time-series variability features (Bellm, 2021) that will provide real-time light curve morphological features at scale. Access to real-time light curve features will serve as vital statistics that will be used to parse through the vast landscape of the incoming alerts, and will also be used to search for certain photometric behaviors. One immediate application is noted in exploring the Rubin alerts that are analogs to, for example, Gaia-GIC-1. Notably, the state-changing features going from a quiescent to periodic to irregular photometric variability are something the LSST alert features will be capable of measuring; however, yet to be confirmed. For example, it has been demonstrated that in both the alert-based infrastructure and the Wide Fast Deep (WFD) survey cadence, periodic sources, such as RR Lyrae and eclipsing binaries, will be routinely discovered at high completeness (Tzanidakis & Bellm, 2025) by using the Rubin alerts. One hypothetical parameter space to be searched for Gaia-GIC-1 analogs can include searching for state-changing stellar sources that transition between periodic and irregular variability. In practice, such signals can be easily recovered by the distributed LSST alerts. Whether these systems are found in real-time or only later in the archive depends on decisions made now. Which filters get written, which features get computed, and how well can we can we understand the contextual variability of ordinary variable stars, in contrast to those experiencing enigmatic variability by circumstellar dust. These are not limits of the survey. They are choices about what we look for, and the systems presented in this dissertation show what is worth looking for in the coming years.

BIBLIOGRAPHY

Abrahams, E. S., Bloom, J. S., Szkody, P., Rix, H.-W., & Mowlavi, N. 2022, ApJ, 938, 46, doi: 10.3847/1538-4357/ac87ab

Aguirre, C., Pichara, K., & Becker, I. 2019, MNRAS, 482, 5078, doi: 10.1093/mnras/sty2836

Alexander, R. D., & Armitage, P. J. 2006, ApJ, 639, L83, doi: 10.1086/503030

Allard, F., Homeier, D., & Freytag, B. 2012, Philosophical Transactions of the Royal Society of London Series A, 370, 2765, doi: 10.1098/rsta.2011.0269

Allers, K. N., Jaffe, D. T., Luhman, K. L., et al. 2007, ApJ, 657, 511, doi: 10.1086/510845

Ambikasaran, S., Foreman-Mackey, D., Greengard, L., Hogg, D. W., & O'Neil, M. 2015, IEEE Transactions on Pattern Analysis and Machine Intelligence, 38, 252, doi: 10.1109/TPAMI.2015.2448083

Anders, F., Khalatyan, A., Queiroz, A. B. A., et al. 2022, A&A, 658, A91, doi: 10.1051/0004-6361/202142369

Andrae, R., Fouesneau, M., Creevey, O., et al. 2018, A&A, 616, A8, doi: 10.1051/0004-6361/201732516

Andrews, S. M. 2020, ARA&A, 58, 483, doi: 10.1146/annurev-astro-031220-010302

Andrews, S. M., Huang, J., Pérez, L. M., et al. 2018, ApJ, 869, L41, doi: 10.3847/2041-8213/aaf741

Angus, R., Foreman-Mackey, D., & Johnson, J. A. 2016, ApJ, 818, 109, doi: 10.3847/0004-637X/818/2/109

Angus, R., Morton, T. D., Foreman-Mackey, D., et al. 2019, AJ, 158, 173, doi: 10.3847/1538-3881/ab3c53

Ansdell, M., Gaidos, E., Rappaport, S. A., et al. 2016, ApJ, 816, 69, doi: 10.3847/0004-637X/816/2/69

Armitage, P. J. 2011, ARA&A, 49, 195, doi: 10.1146/annurev-astro-081710-102521

Arulanantham, N. A., Herbst, W., Cody, A. M., et al. 2016, AJ, 151, 90, doi: 10.3847/0004-6256/151/4/90

Asphaug, E. 2014, Annual Review of Earth and Planetary Sciences, 42, 551

Auvergne, M., Bodin, P., Boisnard, L., et al. 2009, A&A, 506, 411, doi: 10.1051/0004-6361/200810860

Bailer-Jones, C. A. L., Rybizki, J., Fouesneau, M., Demleitner, M., & Andrae, R. 2021a, AJ, 161, 147, doi: 10.3847/1538-3881/abd806

—. 2021b, AJ, 161, 147, doi: 10.3847/1538-3881/abd806

—. 2021c, AJ, 161, 147, doi: 10.3847/1538-3881/abd806

Ballesteros, F. J., Arnalte-Mur, P., Fernandez-Soto, A., & Martínez, V. J. 2018, MNRAS, 473, L21, doi: 10.1093/mnrasl/slx105

Barbary, K. 2018, SEP: Source Extraction and Photometry, Astrophysics Source Code Library, record ascl:1811.004. http://ascl.net/1811.004

Barentsen, G., Vink, J. S., Drew, J. E., et al. 2011, MNRAS, 415, 103, doi: 10.1111/j.1365-2966.2011.18674.x

Barentsen, G., Farnhill, H. J., Drew, J. E., et al. 2014, MNRAS, 444, 3230, doi: 10.1093/mnras/stu1651

Becker, S. A. 1987, in Stellar Pulsation, ed. A. N. Cox, W. M. Sparks, & S. G. Starrfield, Vol. 274, 16, doi: 10.1007/3-540-17668-3_166

Bellm, E. C. 2021, Review of Timeseries Features, Data Management Technical Note DMTN-118, Vera C. Rubin Observatory

Bellm, E. C., Kulkarni, S. R., Graham, M. J., et al. 2019a, PASP, 131, 018002, doi: 10.1088/1538-3873/aaecbe

—. 2019b, PASP, 131, 018002. https://arxiv.org/abs/1902.01932

—. 2019c, PASP, 131, 018002, doi: 10.1088/1538-3873/aaecbe

Bellm, E. C., Blum, R. D., Graham, M. L., et al. 2020, LDM-612: Plans and Policies for LSST Alert Distribution, Tech. rep., NSF-DOE Vera C. Rubin Observatory, doi: 10.71929/RUBIN/2998139

Belokurov, V., Penoyre, Z., Oh, S., et al. 2020, MNRAS, 496, 1922, doi: 10.1093/mnras/staa1522

Benavente, P., Protopapas, P., & Pichara, K. 2017, ApJ, 845, 147, doi: 10.3847/1538-4357/aa7f2d

Bloom, J. S., & Richards, J. W. 2012, in Advances in Machine Learning and Data Mining for Astronomy, ed. M. J. Way, J. D. Scargle, K. M. Ali, & A. N. Srivastava, 89–112, doi: 10.48550/arXiv.1104.3142

Bodman, E. H. L., & Quillen, A. 2016, ApJ, 819, L34, doi: 10.3847/2041-8205/819/2/L34

Bodman, E. H. L., Quillen, A. C., Ansdell, M., et al. 2017, MNRAS, 470, 202, doi: 10.1093/mnras/stx1034

Borucki, W. J., Koch, D., Basri, G., et al. 2010, Science, 327, 977, doi: 10.1126/science.1185402

Bouma, L. G., Hillenbrand, L. A., Howard, A. W., et al. 2024, ApJ, 976, 234, doi: 10.3847/1538-4357/ad855f

Bouvier, J., Grankin, K., Ellerbroek, L. E., Bouy, H., & Barrado, D. 2013, A&A, 557, A77, doi: 10.1051/0004-6361/201321389

Bouvier, J., Chelli, A., Allain, S., et al. 1999, A&A, 349, 619

Bouvier, J., Grankin, K. N., Alencar, S. H. P., et al. 2003, A&A, 409, 169, doi: 10.1051/0004-6361:20030938

Boyajian, T. S., LaCourse, D. M., Rappaport, S. A., et al. 2016a, MNRAS, 457, 3988, doi: 10.1093/mnras/stw218

—. 2016b, MNRAS, 457, 3988, doi: 10.1093/mnras/stw218

—. 2016c, MNRAS, 457, 3988

Boyajian, T. S., Alonso, R., Ammerman, A., et al. 2018, ApJ, 853, L8

Bradley, L., Sipőcz, B., Robitaille, T., et al. 2022, astropy/photutils: 1.5.0, 1.5.0, Zenodo, doi: 10.5281/zenodo.6825092

Breuval, L., Huang, C., & Riess, A. 2025, in American Astronomical Society Meeting Abstracts, Vol. 246, 246th Meeting of the American Astronomical Society, 132.02

Brown, A. G. A., de Geus, E. J., & de Zeeuw, P. T. 1994, A&A, 289, 101, doi: 10.48550/arXiv.astro-ph/9403051

Cadirci, M. S., Evans, D., Leonenko, N., & Makogin, V. 2022, Computational Statistics Data Analysis, 173, 107502, doi: https://doi.org/10.1016/j.csda.2022.107502

Campbell, H. C., Marsh, T. R., Fraser, M., et al. 2015, MNRAS, 452, 1060, doi: 10.1093/mnras/stv1224

Cantat-Gaudin, T., Anders, F., Castro-Ginard, A., et al. 2020, A&A, 640, A1, doi: 10.1051/0004-6361/202038192

Canup, R. M. 2004, ARA&A, 42, 441, doi: 10.1146/annurev.astro.41.082201.113457

Capistrant, B. K., Soares-Furtado, M., Vanderburg, A., et al. 2022, ApJS, 263, 14, doi: 10.3847/1538-4365/ac9125

Caplar, N., Beebe, W., Branton, D., et al. 2025, arXiv e-prints, arXiv:2501.02103, doi: 10.48550/arXiv.2501.02103

Caratti o Garatti, A., Garcia Lopez, R., Antoniucci, S., et al. 2012, A&A, 538, A64, doi: 10.1051/0004-6361/201117781

Carroll, S. M., Guinan, E. F., McCook, G. P., & Donahue, R. A. 1991, ApJ, 367, 278, doi: 10.1086/169626

Catelan, M. 2023, in Memorie della Societa Astronomica Italiana, Vol. 94, 56, doi: 10.36116/MEMSAIT_94N4.2023.56

Ceillier, T., Tayar, J., Mathur, S., et al. 2017, A&A, 605, A111, doi: 10.1051/0004-6361/201629884

Chambers, J. E. 2001, 152, 205

Chambers, K. C., Magnier, E. A., Metcalfe, N., et al. 2016, arXiv e-prints, arXiv:1612.05560. https://arxiv.org/abs/1612.05560

Chan, H.-S., Villar, V. A., Cheung, S.-H., et al. 2022, ApJ, 932, 118, doi: 10.3847/1538-4357/ac69d4

Chen, X., Wang, S., Deng, L., et al. 2020, ApJS, 249, 18, doi: 10.3847/1538-4365/ab9cae

Chmielewski, Y. 2000, A&A, 353, 666

Ciardi, D. R., von Braun, K., Bryden, G., et al. 2011, AJ, 141, 108, doi: 10.1088/0004-6256/141/4/108

Clausen, D., Wade, R. A., Kopparapu, R. K., & O'Shaughnessy, R. 2012, ApJ, 746, 186, doi: 10.1088/0004-637X/746/2/186

Clement, M. S., Kaib, N. A., & Chambers, J. E. 2020, , 1, 18, doi: 10.3847/PSJ/ab91aa

Cody, A. M., & Hillenbrand, L. A. 2018a, AJ, 156, 71, doi: 10.3847/1538-3881/aacead

—. 2018b, AJ, 156, 71, doi: 10.3847/1538-3881/aacead

Cody, A. M., Stauffer, J., Baglin, A., et al. 2014a, AJ, 147, 82, doi: 10.1088/0004-6256/147/4/82

—. 2014b, AJ, 147, 82, doi: 10.1088/0004-6256/147/4/82

—. 2014c, AJ, 147, 82, doi: 10.1088/0004-6256/147/4/82

Corradi, R. L. M., Mikolajewska, J., & Mahoney, T. J., eds. 2003, Astronomical Society of the Pacific Conference Series, Vol. 303, Symbiotic Stars Probing Stellar Evolution

Corradi, R. L. M., Rodríguez-Flores, E. R., Mampaso, A., et al. 2008, A&A, 480, 409, doi: 10.1051/0004-6361:20078989

Coughlin, M. W., Burdge, K., Duev, D. A., et al. 2021, MNRAS, 505, 2954, doi: 10.1093/mnras/stab1502

Covey, K. R., Ivezić, Ž., Schlegel, D., et al. 2007, AJ, 134, 2398, doi: 10.1086/522052

Creevey, O. L., Sordo, R., Pailler, F., et al. 2023, A&A, 674, A26, doi: 10.1051/0004-6361/202243688

Davenport, J. 2021, PyKOSMOS: A Python-Based Spectral Reduction Suite for KOSMOS at APO, Zenodo, doi: 10.5281/zenodo.5120786

Davenport, J. R. A., & Dorn-Wallenstein, T. Z. 2019, Research Notes of the American Astronomical Society, 3, 54, doi: 10.3847/2515-5172/ab11c9

Davenport, J. R. A., Ivezić, Ž., Becker, A. C., et al. 2014, MNRAS, 440, 3430, doi: 10.1093/mnras/stu466

Davenport, J. R. A., Covey, K. R., Clarke, R. W., et al. 2018, ApJ, 853, 130, doi: 10.3847/1538-4357/aaa413

De, K., Hankins, M. J., Kasliwal, M. M., et al. 2020, PASP, 132, 025001, doi: 10.1088/1538-3873/ab6069

De Marco, O., Clayton, G. C., Herwig, F., et al. 2002, AJ, 123, 3387, doi: 10.1086/340569

De Paolis, F., Ingrosso, G., & Qadir, A. 1995, Ap&SS, 234, 57, doi: 10.1007/BF00627282

de Wit, W. J., Grinin, V. P., Potravnov, I. S., et al. 2013, A&A, 553, L1, doi: 10.1051/0004-6361/201220715

Debosscher, J., Sarro, L. M., Aerts, C., et al. 2007, A&A, 475, 1159, doi: 10.1051/0004-6361:20077638

Deharveng, L., Zavagno, A., Anderson, L. D., et al. 2012, A&A, 546, A74, doi: 10.1051/0004-6361/201219131

Dekany, R., Smith, R. M., Riddle, R., et al. 2020, PASP, 132, 038001, doi: 10.1088/1538-3873/ab4ca2

Delfini, L., Vioque, M., Ribas, Á., & Hodgkin, S. 2025, A&A, 699, A145, doi: 10.1051/0004-6361/202453539

Delgado, A., Harrison, D., Hodgkin, S., et al. 2017, Transient Name Server Discovery Report, 2017-690, 1

—. 2019, Transient Name Server Discovery Report, 2019-246, 1

Dias, W. S., Monteiro, H., Caetano, T. C., et al. 2014, A&A, 564, A79, doi: 10.1051/0004-6361/201323226

Djorgovski, S. G., Mahabal, A. A., Drake, A. J., et al. 2012, in IAU Symposium, Vol. 285, New Horizons in Time Domain Astronomy, ed. E. Griffin, R. Hanisch, & R. Seaman, 141–146, doi: 10.1017/S1743921312000488

Donati, J.-F., Cristofari, P. I., Lehmann, L. T., et al. 2024, MNRAS, 531, 3256, doi: 10.1093/mnras/stae1227

Doré, O., Werner, M. W., Ashby, M. L. N., et al. 2018, arXiv e-prints, arXiv:1805.05489, doi: 10.48550/arXiv.1805.05489

Dotter, A. 2016, ApJS, 222, 8, doi: 10.3847/0067-0049/222/1/8

Draine, B. T. 2003, ARA&A, 41, 241, doi: 10.1146/annurev.astro.41.011802.094840

Drake, A. J. 2023, ZTF Science Data System Explanations: Zubercal, http://atua.caltech.edu/ZTF/Zubercal.html

Drake, A. J., & Cook, K. H. 2003, ApJ, 589, 281, doi: 10.1086/374640

Drake, A. J., Djorgovski, S. G., Mahabal, A., et al. 2012, in IAU Symposium, Vol. 285, New Horizons in Time Domain Astronomy, ed. E. Griffin, R. Hanisch, & R. Seaman, 306–308, doi: 10.1017/S1743921312000889

Drew, J. E., Greimel, R., Irwin, M. J., et al. 2005, MNRAS, 362, 753, doi: 10.1111/j.1365-2966.2005.09330.x

Duchêne, G., & Kraus, A. 2013, ARA&A, 51, 269, doi: 10.1146/annurev-astro-081710-102602

Dullemond, C., & Monnier, J. 2010, Annual Review of Astronomy and Astrophysics, 48, 205, doi: https://doi.org/10.1146/annurev-astro-081309-130932

Dumm, T., & Schild, H. 1998, New A, 3, 137, doi: 10.1016/S1384-1076(98)00003-7

Dupree, A. K., Strassmeier, K. G., Calderwood, T., et al. 2022, ApJ, 936, 18, doi: 10.3847/1538-4357/ac7853

Dyck, H. M., Benson, J. A., van Belle, G. T., & Ridgway, S. T. 1996, AJ, 111, 1705, doi: 10.1086/117910

Dytso, A., Bustin, R., Poor, H. V., & Shamai, S. 2018, Journal of Statistical Distributions and Applications, 5, 6, doi: 10.1186/s40488-018-0088-5

Elias, F., Alfaro, E. J., & Cabrera-Caño, J. 2009, MNRAS, 397, 2, doi: 10.1111/j.1365-2966.2009.14465.x

Espaillat, C., Muzerolle, J., Hernández, J., et al. 2008, ApJ, 689, L145, doi: 10.1086/595869

Eyer, L., & Mowlavi, N. 2008, in Journal of Physics Conference Series, Vol. 118, Journal of Physics Conference Series (IOP), 012010, doi: 10.1088/1742-6596/118/1/012010

Fabricius, C. 1993, Bulletin d'Information du Centre de Donnees Stellaires, 42, 5

Fazio, G. G., Hora, J. L., Allen, L. E., et al. 2004, ApJS, 154, 10, doi: 10.1086/422843

Feigelson, E. D., & Montmerle, T. 1999, ARA&A, 37, 363, doi: 10.1146/annurev.astro.37.1.363

Fernie, J. D. 1969, PASP, 81, 707, doi: 10.1086/128847

Feroz, F., Hobson, M. P., & Bridges, M. 2009, MNRAS, 398, 1601, doi: 10.1111/j.1365-2966.2009.14548.x

Fetherolf, T., Pepper, J., Simpson, E., et al. 2023, ApJS, 268, 4, doi: 10.3847/1538-4365/acdee5

Findeisen, K., Lim, K.-T., Speck, D., et al. 2026, arXiv e-prints, arXiv:2603.19541, doi: 10.48550/arXiv.2603.19541

Fischer, W. J., Hillenbrand, L. A., Herczeg, G. J., et al. 2023, in Astronomical Society of the Pacific Conference Series, Vol. 534, Protostars and Planets VII, ed. S. Inutsuka, Y. Aikawa, T. Muto, K. Tomida, & M. Tamura, 355, doi: 10.48550/arXiv.2203.11257

Fitton, S., Tofflemire, B. M., & Kraus, A. L. 2022, Research Notes of the American Astronomical Society, 6, 18, doi: 10.3847/2515-5172/ac4bb7

Fitzpatrick, E. L. 1999a, PASP, 111, 63, doi: 10.1086/316293

—. 1999b, PASP, 111, 63, doi: 10.1086/316293

Fitzpatrick, E. L., & Massa, D. 1990, ApJS, 72, 163, doi: 10.1086/191413

Foreman-Mackey, D., Hogg, D. W., Lang, D., & Goodman, J. 2013, PASP, 125, 306, doi: 10.1086/670067

Forés-Toribio, R., JoHantgen, B., Kochanek, C. S., et al. 2025, arXiv e-prints, arXiv:2507.03080, doi: 10.48550/arXiv.2507.03080

Förster, F., Cabrera-Vives, G., Castillo-Navarrete, E., et al. 2021, AJ, 161, 242, doi: 10.3847/1538-3881/abe9bc

Fouesneau, M. 2025, pyphot, pyphot_v1.6.0, Zenodo, doi: 10.5281/zenodo.14712174

Fujiwara, H., Ishihara, D., Onaka, T., et al. 2013, A&A, 550, A45

Gabriel, T. S. J., & Cambioni, S. 2023, Annual Review of Earth and Planetary Sciences, 51, 671

Gagné, J., Mamajek, E. E., Malo, L., et al. 2018, ApJ, 856, 23, doi: 10.3847/1538-4357/aaae09

Gaia Collaboration, Eyer, L., Rimoldini, L., et al. 2019a, A&A, 623, A110, doi: 10.1051/0004-6361/201833304

—. 2019b, A&A, 623, A110, doi: 10.1051/0004-6361/201833304

Gaia Collaboration, Brown, A. G. A., Vallenari, A., et al. 2021a, A&A, 649, A1, doi: 10.1051/0004-6361/202039657

Gaia Collaboration, Smart, R. L., Sarro, L. M., et al. 2021b, A&A, 649, A6, doi: 10.1051/0004-6361/202039498

Gaia Collaboration, Vallenari, A., Brown, A. G. A., et al. 2022a, arXiv e-prints, arXiv:2208.00211, doi: 10.48550/arXiv.2208.00211

—. 2022b, arXiv e-prints, arXiv:2208.00211, doi: 10.48550/arXiv.2208.00211

—. 2023, A&A, 674, A1, doi: 10.1051/0004-6361/202243940

Galli, P. A. B., Bertout, C., Teixeira, R., & Ducourant, C. 2015, A&A, 580, A26, doi: 10.1051/0004-6361/201525804

Gavras, P., Rimoldini, L., Nienartowicz, K., et al. 2023, A&A, 674, A22, doi: 10.1051/0004-6361/202244367

Genda, H., & Abe, Y. 2005, Nature, 433, 842

Genda, H., Kobayashi, H., & Kokubo, E. 2015, ApJ, 810, 136, doi: 10.1088/0004-637X/810/2/136

Gerhard, O., & Silk, J. 1996, ApJ, 472, 34, doi: 10.1086/178039

Ghez, A. M., Neugebauer, G., & Matthews, K. 1993, AJ, 106, 2005, doi: 10.1086/116782

Gibson, J. L., & Stencel, R. E. 2018, MNRAS, 476, 5026, doi: 10.1093/mnras/sty639

Gilbert, G. J. 2022, AJ, 163, 111, doi: 10.3847/1538-3881/ac45f4

Giles, D. K., & Walkowicz, L. 2020, MNRAS, 499, 524, doi: 10.1093/mnras/staa2736

Giles, H. A. C., Collier Cameron, A., & Haywood, R. D. 2017, MNRAS, 472, 1618, doi: 10.1093/mnras/stx1931

Gómez-Muñoz, M. A., Bianchi, L., & Manchado, A. 2023, ApJS, 266, 34, doi: 10.3847/1538-4365/acca77

Gorbikov, E., & Brosch, N. 2014, MNRAS, 443, 725, doi: 10.1093/mnras/stu1183

Graham, M. J., Kulkarni, S. R., Bellm, E. C., et al. 2019a, PASP, 131, 078001, doi: 10.1088/1538-3873/ab006c

—. 2019b, PASP, 131, 078001, doi: 10.1088/1538-3873/ab006c

Graham, M. L., Bellm, E. C., Guy, L. P., et al. 2024, DMTN-102: LSST Alerts: Key Numbers, Tech. rep., NSF-DOE Vera C. Rubin Observatory, doi: 10.71929/RUBIN/2997858

Gras-Velázquez, À., & Ray, T. P. 2005, A&A, 443, 541, doi: 10.1051/0004-6361:20042397

Green, M. J., Maoz, D., Mazeh, T., et al. 2023, MNRAS, 522, 29, doi: 10.1093/mnras/stad915

Grindlay, J. 2017, in Astrophysics and Space Science Proceedings, Vol. 50, The Science of Time 2016, ed. E. F. Arias, L. Combrinck, P. Gabor, C. Hohenkerk, & P. K. Seidelmann, 203, doi: 10.1007/978-3-319-59909-0_26

Grindlay, J., Tang, S., Los, E., & Servillat, M. 2012, in IAU Symposium, Vol. 285, New Horizons in Time Domain Astronomy, ed. E. Griffin, R. Hanisch, & R. Seaman, 29–34, doi: 10.1017/S1743921312000166

Grinin, V. P., Potravnov, I. S., & Musaev, F. A. 2010, A&A, 524, A8, doi: 10.1051/0004-6361/201014889

Gromadzki, M., Mikołajewska, J., & Soszyński, I. 2013, Acta Astron., 63, 405, doi: 10.48550/arXiv.1312.6063

Gupta, S., Jose, J., More, S., et al. 2021, MNRAS, 508, 3388, doi: 10.1093/mnras/stab2751

Han, Z., Podsiadlowski, P., Maxted, P. F. L., Marsh, T. R., & Ivanova, N. 2002, in Astronomical Society of the Pacific Conference Series, Vol. 279, Exotic Stars as Challenges to Evolution, ed. C. A. Tout & W. van Hamme, 285

Hartmann, L., Herczeg, G., & Calvet, N. 2016, ARA&A, 54, 135, doi: 10.1146/annurev-astro-081915-023347

Hartmann, L., Hewett, R., & Calvet, N. 1994, ApJ, 426, 669, doi: 10.1086/174104

Hedges, C., Hodgkin, S., & Kennedy, G. 2018, MNRAS, 476, 2968, doi: 10.1093/mnras/sty328

Hillenbrand, L. A., Carvalho, A. S., Stern, D., et al. 2025, ApJ, 988, 77, doi: 10.3847/1538-4357/ade14d

Hillenbrand, L. A., Kiker, T. J., Gee, M., et al. 2022a, AJ, 163, 263, doi: 10.3847/1538-3881/ac62d8

—. 2022b, AJ, 163, 263, doi: 10.3847/1538-3881/ac62d8

Hodapp, K. W., Gaidos, E., Kenworthy, M. A., et al. 2024, AJ, 167, 85, doi: 10.3847/1538-3881/ad1931

Hodgkin, S. T., Breedt, E., Delgado, A., et al. 2020, Transient Name Server Discovery Report, 2020-2792, 1

Hodgkin, S. T., Harrison, D. L., Breedt, E., et al. 2021a, A&A, 652, A76, doi: 10.1051/0004-6361/202140735

—. 2021b, A&A, 652, A76, doi: 10.1051/0004-6361/202140735

Hodgkin, S. T., Breedt, E., Delgado, A., et al. 2021c, Transient Name Server Discovery Report, 2021-226, 1

Hoffleit, D. 1972, , 1, 3

Hon, M., Rappaport, S., Shporer, A., et al. 2025, ApJ, 984, L3, doi: 10.3847/2041-8213/adbf21

Hu, Z., Zhu, W., Wang, S., & Xuesong Wang, S. 2026, arXiv e-prints, arXiv:2601.16828, doi: 10.48550/arXiv.2601.16828

Huang, S.-S. 1964, An interpretation of epsilon Aurigae: Opaque gaseous disk rotating around secondary component as model of eclipsing binary star Epsilon Aurigae, Technical Memorandum NASA-TM-X-51719, NASA Goddard Space Flight Center, Greenbelt, MD, United States. https://ntrs.nasa.gov/api/citations/19650012586/downloads/19650012586.pdf

Huehnerhoff, J., Ketzeback, W., Bradley, A., et al. 2016, in Society of Photo-Optical Instrumentation Engineers (SPIE) Conference Series, Vol. 9908, Ground-based and Airborne Instrumentation for Astronomy VI, ed. C. J. Evans, L. Simard, & H. Takami, 99085H, doi: 10.1117/12.2234214

Hughes, A. M., Duchêne, G., & Matthews, B. C. 2018a, ARA&A, 56, 541

—. 2018b, ARA&A, 56, 541, doi: 10.1146/annurev-astro-081817-052035

Hunt, E. L., & Reffert, S. 2024, A&A, 686, A42, doi: 10.1051/0004-6361/202348662

Hurt, S. A., & MacGregor, M. A. 2023, ApJ, 954, 10, doi: 10.3847/1538-4357/accf9d

Hwang, H.-C., Ting, Y.-S., Cheng, S., & Speagle, J. S. 2024, MNRAS, 528, 4272, doi: 10.1093/mnras/stae297

Ingleby, L., Calvet, N., Hernández, J., et al. 2014, ApJ, 790, 47, doi: 10.1088/0004-637X/790/1/47

IRSA. 2022, Time Series Tool, IPAC, doi: 10.26131/IRSA538

Ishida, E. E. O., Kornilov, M. V., Malanchev, K. L., et al. 2021, A&A, 650, A195, doi: 10.1051/0004-6361/202037709

Ivezić, Ž., Kahn, S. M., Tyson, J. A., et al. 2019, ApJ, 873, 111, doi: 10.3847/1538-4357/ab042c

Jackson, A. P., & Wyatt, M. C. 2012a, MNRAS, 425, 657

—. 2012b, MNRAS, 425, 657

Jackson, A. P., Wyatt, M. C., Bonsor, A., & Veras, D. 2014, MNRAS, 440, 3757, doi: 10.1093/mnras/stu476

Jeffries, R. D., Jackson, R. J., Wright, N. J., et al. 2023, MNRAS, 523, 802, doi: 10.1093/mnras/stad1293

Jenkner, H. 1994, Ap&SS, 217, 31, doi: 10.1007/BF00990019

JoHantgen, B., Rowan, D. M., Forés-Toribio, R., et al. 2025, arXiv e-prints, arXiv:2507.19594, doi: 10.48550/arXiv.2507.19594

Johnson, O. A., Gajjar, V., Keane, E. F., et al. 2023, AJ, 166, 193, doi: 10.3847/1538-3881/acf9f5

Joy, A. H. 1945, ApJ, 102, 168, doi: 10.1086/144749

Karambelkar, V. R., Kasliwal, M. M., Tisserand, P., et al. 2021, ApJ, 910, 132, doi: 10.3847/1538-4357/abe5aa

Karr, J. L., & Martin, P. G. 2003, ApJ, 595, 880, doi: 10.1086/376895

Kennedy, G. M., Kenworthy, M. A., Pepper, J., et al. 2017, Royal Society Open Science, 4, 160652, doi: 10.1098/rsos.160652

Kenworthy, M., Lock, S., Kennedy, G., et al. 2023a, Nature, 622, 251, doi: 10.1038/s41586-023-06573-9

—. 2023b, Nature, 622, 251

Kenworthy, M. A., & Mamajek, E. E. 2015a, ApJ, 800, 126, doi: 10.1088/0004-637X/800/2/126

—. 2015b, ApJ, 800, 126

Kenworthy, M. A., Lacour, S., Kraus, A., et al. 2015, MNRAS, 446, 411, doi: 10.1093/mnras/stu2067

Kenworthy, M. A., Klaassen, P. D., Min, M., et al. 2020, A&A, 633, A115, doi: 10.1051/0004-6361/201936141

Kenyon, S. J., & Bromley, B. C. 2005, AJ, 130, 269, doi: 10.1086/430461

Kerins, E., Binney, J., & Silk, J. 2002, MNRAS, 332, L29, doi: 10.1046/j.1365-8711.2002.05463.x

Kharchenko, N. V., Piskunov, A. E., Röser, S., Schilbach, E., & Scholz, R.-D. 2005, A&A, 440, 403, doi: 10.1051/0004-6361:20052740

Kiefer, F., Lecavelier des Etangs, A., Augereau, J. C., et al. 2014, A&A, 561, L10

Kiefer, F., Lecavelier des Étangs, A., Vidal-Madjar, A., et al. 2017, A&A, 608, A132, doi: 10.1051/0004-6361/201731306

Kim, S.-L., Lee, C.-U., Park, B.-G., et al. 2016, Journal of Korean Astronomical Society, 49, 37, doi: 10.5303/JKAS.2016.49.1.37

Kiss, L. L., Szabó, G. M., & Bedding, T. R. 2006, MNRAS, 372, 1721, doi: 10.1111/j.1365-2966.2006.10973.x

Klaassen, P., Kenworthy, M. A., Mamajek, E. E., et al. 2025, Research Notes of the American Astronomical Society, 9, 326, doi: 10.3847/2515-5172/ae2680

Kley, W., & Nelson, R. P. 2012, ARA&A, 50, 211, doi: 10.1146/annurev-astro-081811-125523

Kloppenborg, B., Stencel, R., Monnier, J. D., et al. 2010, Nature, 464, 870, doi: 10.1038/nature08968

Kloppenborg, B. K., Hopkins, J. L., & Stencel, R. E. 2012, , 40, 647, doi: 10.48550/arXiv.1303.6871

Kochanek, C. S., Shappee, B. J., Stanek, K. Z., et al. 2017a, PASP, 129, 104502, doi: 10.1088/1538-3873/aa80d9

—. 2017b, PASP, 129, 104502, doi: 10.1088/1538-3873/aa80d9

Koenig, X. P., & Leisawitz, D. T. 2014, ApJ, 791, 131, doi: 10.1088/0004-637X/791/2/131

Koenigl, A. 1991, ApJ, 370, L39, doi: 10.1086/185972

Kollmeier, J. A., Zasowski, G., Rix, H.-W., et al. 2017, arXiv e-prints, arXiv:1711.03234, doi: 10.48550/arXiv.1711.03234

Kos, J. 2024, A&A, 691, A28, doi: 10.1051/0004-6361/202449828

Kraus, A. L., & Hillenbrand, L. A. 2008, ApJ, 686, L111, doi: 10.1086/593012

LaCourse, D. 2016, The NASA K2 Mission has yet to observe an analog of Tabby's Star, Zenodo

Lammers, C., Cranmer, M., Hadden, S., et al. 2024, ApJ, 975, 228, doi: 10.3847/1538-4357/ad7fe5

Law, N. M., Kulkarni, S. R., Dekany, R. G., et al. 2009, PASP, 121, 1395, doi: 10.1086/648598

Lawrence, A. 2001, MNRAS, 323, 147, doi: 10.1046/j.1365-8711.2001.04116.x

Leavitt, H. S., & Pickering, E. C. 1912, Harvard College Observatory Circular, 173, 1

Levesque, E. M., & Massey, P. 2020, ApJ, 891, L37, doi: 10.3847/2041-8213/ab7935

Li, S.-L., Miller, N., Lin, D. N. C., & Fortney, J. J. 2010, Nature, 463, 1054, doi: 10.1038/nature08715

Lipunov, V., Gorbovskoy, E., Afanasiev, V., et al. 2016, A&A, 588, A90, doi: 10.1051/0004-6361/201526528

Lock, S. J., & Stewart, S. T. 2019, Science Advances, 5, eaav3746, doi: 10.1126/sciadv.aav3746

Lomb, N. R. 1976a, Ap&SS, 39, 447, doi: 10.1007/BF00648343

—. 1976b, Ap&SS, 39, 447, doi: 10.1007/BF00648343

Longarini, C., Lodato, G., Toci, C., & Aly, H. 2021, MNRAS, 503, 4930, doi: 10.1093/mnras/stab843

LSST Science Collaboration, Abell, P. A., Allison, J., et al. 2009, arXiv e-prints, arXiv:0912.0201, doi: 10.48550/arXiv.0912.0201

Ludendorff, H. 1903, Astronomische Nachrichten, 164, 81, doi: 10.1002/asna.19031640602

Luri, X., Brown, A. G. A., Sarro, L. M., et al. 2018, A&A, 616, A9, doi: 10.1051/0004-6361/201832964

Mackenzie, C., Pichara, K., & Protopapas, P. 2016, ApJ, 820, 138, doi: 10.3847/0004-637X/820/2/138

Mahabal, A. A., Djorgovski, S. G., Drake, A. J., et al. 2011, Bulletin of the Astronomical Society of India, 39, 387, doi: 10.48550/arXiv.1111.0313

Mainzer, A., Bauer, J., Grav, T., et al. 2011, ApJ, 731, 53, doi: 10.1088/0004-637X/731/1/53

Mainzer, A., Bauer, J., Cutri, R. M., et al. 2014, ApJ, 792, 30, doi: 10.1088/0004-637X/792/1/30

Makarov, V. V., & Goldin, A. 2016, ApJ, 833, 78, doi: 10.3847/1538-4357/833/1/78

Malanchev, K., Kornilov, M. V., Pruzhinskaya, M. V., et al. 2023, PASP, 135, 024503, doi: 10.1088/1538-3873/acb292

Malanchev, K. L., Pruzhinskaya, M. V., Korolev, V. S., et al. 2021, MNRAS, 502, 5147, doi: 10.1093/mnras/stab316

Mamajek, E. E. 2009, in American Institute of Physics Conference Series, Vol. 1158, Exoplanets and Disks: Their Formation and Diversity, ed. T. Usuda, M. Tamura, & M. Ishii (AIP), 3–10, doi: 10.1063/1.3215910

Mamajek, E. E., Quillen, A. C., Pecaut, M. J., et al. 2012, AJ, 143, 72, doi: 10.1088/0004-6256/143/3/72

Mannings, V., Boss, A. P., & Russell, S. S., eds. 2000, Protostars and Planets IV

Marengo, M., Hulsebus, A., & Willis, S. 2015, ApJ, 814, L15, doi: 10.1088/2041-8205/814/1/L15

Marshall, J. P., Ertel, S., Kemper, F., et al. 2023a, ApJ, 954, 140, doi: 10.3847/1538-4357/ace629

—. 2023b, ApJ, 954, 140, doi: 10.3847/1538-4357/ace629

Martin, D. C., Fanson, J., Schiminovich, D., et al. 2005a, ApJ, 619, L1, doi: 10.1086/426387

—. 2005b, ApJ, 619, L1, doi: 10.1086/426387

Martinez, M. A. S., Stone, N. C., & Metzger, B. D. 2019, MNRAS, 489, 5119, doi: 10.1093/mnras/stz2464

Martínez-Galarza, J. R., Bianco, F. B., Crake, D., et al. 2021, MNRAS, 508, 5734, doi: 10.1093/mnras/stab2588

Masci, F. J., Laher, R. R., Rusholme, B., et al. 2019, PASP, 131, 018003, doi: 10.1088/1538-3873/aae8ac

Massey, P., Levesque, E. M., Olsen, K. A. G., Plez, B., & Skiff, B. A. 2007, ApJ, 660, 301, doi: 10.1086/513182

Maxted, P. F. L., Bloemen, S., Heber, U., et al. 2014, MNRAS, 437, 1681, doi: 10.1093/mnras/stt2007

Mayama, S., Akiyama, E., Panić, O., et al. 2018, ApJ, 868, L3, doi: 10.3847/2041-8213/aae88b

McGinnis, P. T., Alencar, S. H. P., Guimarães, M. M., et al. 2015, A&A, 577, A11, doi: 10.1051/0004-6361/201425475

Meheut, H., Casse, F., Varniere, P., & Tagger, M. 2010, A&A, 516, A31, doi: 10.1051/0004-6361/201014000

Meisner, A. M., Caselden, D., Schlafly, E. F., & Kiwy, F. 2023a, AJ, 165, 36, doi: 10.3847/1538-3881/aca2ab

—. 2023b, AJ, 165, 36, doi: 10.3847/1538-3881/aca2ab

Melis, C., Olofsson, J., Song, I., et al. 2021, ApJ, 923, 90, doi: 10.3847/1538-4357/ac2603

Meng, H. Y. A., Su, K. Y. L., Rieke, G. H., et al. 2014, Science, 345, 1032, doi: 10.1126/science.1255153

Meng, Z., Quillen, A. C., Bell, C. P. M., et al. 2014, MNRAS, 441, 3733, doi: 10.1093/mnras/stu854

Mentel, R. T., Kenworthy, M. A., Cameron, D. A., et al. 2018, A&A, 619, A157, doi: 10.1051/0004-6361/201834004

Metzger, B. D., Shen, K. J., & Stone, N. 2017, MNRAS, 468, 4399, doi: 10.1093/mnras/stx823

Meyer, M. R., Calvet, N., & Hillenbrand, L. A. 1997, AJ, 114, 288, doi: 10.1086/118474

Monet, D. G., Levine, S. E., Canzian, B., et al. 2003, AJ, 125, 984, doi: 10.1086/345888

Montargès, M., Cannon, E., Lagadec, E., et al. 2021, Nature, 594, 365, doi: 10.1038/s41586-021-03546-8

Montet, B. T., & Simon, J. D. 2016, ApJ, 830, L39, doi: 10.3847/2041-8205/830/2/L39

Moór, A., Ábrahám, P., Kóspál, Á., et al. 2022, MNRAS, 516, 5684, doi: 10.1093/mnras/stac2595

Morales-Calderón, M., Stauffer, J. R., Hillenbrand, L. A., et al. 2011, ApJ, 733, 50, doi: 10.1088/0004-637X/733/1/50

Morton, T. D. 2015, isochrones: Stellar model grid package, Astrophysics Source Code Library, record ascl:1503.010

Mrnjavac, N., Wimmer, J. L. E., Brabender, M., et al. 2023, ChemPlusChem, 88, e202300270

Nagel, E., Bouvier, J., & Duarte, A. E. 2024, A&A, 688, A61, doi: 10.1051/0004-6361/202450085

Nealon, R., Cuello, N., & Alexander, R. 2020, MNRAS, 491, 4108, doi: 10.1093/mnras/stz3186

Nealon, R., Dipierro, G., Alexander, R., Martin, R. G., & Nixon, C. 2018, MNRAS, 481, 20, doi: 10.1093/mnras/sty2267

Nielsen, M. B., Gizon, L., Schunker, H., & Karoff, C. 2013, A&A, 557, L10, doi: 10.1051/0004-6361/201321912

NSF-DOE Vera C. Rubin Observatory. 2026a, Alerts and Brokers, https://rubinobservatory.org/for-scientists/data-products/alerts-and-brokers

—. 2026b, Template generation, Rubin Prompt Products documentation, https://prompt-products.lsst.io/processing/templates/index.html

Nun, I., Protopapas, P., Sim, B., et al. 2015, arXiv e-prints, arXiv:1506.00010, doi: 10.48550/arXiv.1506.00010

Oberst, T. E., Rodriguez, J. E., Colón, K. D., et al. 2017, AJ, 153, 97, doi: 10.3847/1538-3881/153/3/97

Offner, S. S. R., Moe, M., Kratter, K. M., et al. 2023, in Astronomical Society of the Pacific Conference Series, Vol. 534, Protostars and Planets VII, ed. S. Inutsuka, Y. Aikawa, T. Muto, K. Tomida, & M. Tamura, 275, doi: 10.48550/arXiv.2203.10066

Onken, C. A., Wolf, C., Bessell, M. S., et al. 2024, PASA, 41, e061, doi: 10.1017/pasa.2024.53

—. 2019, PASA, 36, e033, doi: 10.1017/pasa.2019.27

Osborn, H. P., Rodriguez, J. E., Kenworthy, M. A., et al. 2017, MNRAS, 471, 740, doi: 10.1093/mnras/stx1249

Otto, J. M., Frinchaboy, P. M., Myers, N. R., et al. 2026, AJ, 171, 91, doi: 10.3847/1538-3881/ae28d8

Paczynski, B. 1997, in Variables Stars and the Astrophysical Returns of the Microlensing Surveys, ed. R. Ferlet, J.-P. Maillard, & B. Raban, 357, doi: 10.48550/arXiv.astro-ph/9609073

Panja, A., Sun, Y., Chen, W. P., & Mondal, S. 2022, ApJ, 939, 46, doi: 10.3847/1538-4357/ac940f

Parthasarathy, M., & Frueh, M. L. 1986, Ap&SS, 123, 31, doi: 10.1007/BF00649121

Paxton, B., Bildsten, L., Dotter, A., et al. 2011, ApJS, 192, 3, doi: 10.1088/0067-0049/192/1/3

Paxton, B., Cantiello, M., Arras, P., et al. 2013, ApJS, 208, 4, doi: 10.1088/0067-0049/208/1/4

Paxton, B., Marchant, P., Schwab, J., et al. 2015, ApJS, 220, 15, doi: 10.1088/0067-0049/220/1/15

Paxton, B., Schwab, J., Bauer, E. B., et al. 2018, ApJS, 234, 34, doi: 10.3847/1538-4365/aaa5a8

Paxton, B., Smolec, R., Schwab, J., et al. 2019, ApJS, 243, 10, doi: 10.3847/1538-4365/ab2241

Pecaut, M. J., & Mamajek, E. E. 2013, ApJS, 208, 9, doi: 10.1088/0067-0049/208/1/9

Perren, G. I., Pera, M. S., Navone, H. D., & Vázquez, R. A. 2023, MNRAS, 526, 4107, doi: 10.1093/mnras/stad2826

Petigura, E. A., & Marcy, G. W. 2012, PASP, 124, 1073, doi: 10.1086/668291

Petrosky, E., Hwang, H.-C., Zakamska, N. L., Chandra, V., & Hill, M. J. 2021, MNRAS, 503, 3975, doi: 10.1093/mnras/stab592

Pichara, K., Protopapas, P., & León, D. 2016, ApJ, 819, 18, doi: 10.3847/0004-637X/819/1/18

Poppenhaeger, K., Cody, A. M., Covey, K. R., et al. 2015, AJ, 150, 118, doi: 10.1088/0004-6256/150/4/118

Pouilly, K., Bouvier, J., Alecian, E., et al. 2021, A&A, 656, A50, doi: 10.1051/0004-6361/202140850

Pramono, T. H., Kenworthy, M. A., & van Boekel, R. 2024a, A&A, 688, L11, doi: 10.1051/0004-6361/202450288

—. 2024b, A&A, 688, L11, doi: 10.1051/0004-6361/202450288

Prato, L., & Weinberger, A. J. 2007, arXiv e-prints, arXiv:0705.3258, doi: 10.48550/arXiv.0705.3258

Prisinzano, L., Damiani, F., Sciortino, S., et al. 2022, A&A, 664, A175, doi: 10.1051/0004-6361/202243580

Prochaska, J., Hennawi, J., Westfall, K., et al. 2020, The Journal of Open Source Software, 5, 2308, doi: 10.21105/joss.02308

Qian, S.-B., Shi, X.-D., Zhu, L.-Y., et al. 2019, Research in Astronomy and Astrophysics, 19, 064, doi: 10.1088/1674-4527/19/5/64

Queiroz, A. B. A., Anders, F., Chiappini, C., et al. 2020, A&A, 638, A76, doi: 10.1051/0004-6361/201937364

Quintana, E. V., Barclay, T., Borucki, W. J., Rowe, J. F., & Chambers, J. E. 2016a, ApJ, 821, 126, doi: 10.3847/0004-637X/821/2/126

—. 2016b, ApJ, 821, 126, doi: 10.3847/0004-637X/821/2/126

Quintana, E. V., Barclay, T., Borucki, W. J., et al. 2016c, ApJ, 821, 126

Rappaport, N. J., Iess, L., Tortora, P., et al. 2007, Icarus, 190, 175, doi: https://doi.org/10.1016/j.icarus.2007.03.025

Rappaport, S., Levine, A., Chiang, E., et al. 2012a, ApJ, 752, 1, doi: 10.1088/0004-637X/752/1/1

—. 2012b, ApJ, 752, 1, doi: 10.1088/0004-637X/752/1/1

Rappaport, S., Vanderburg, A., Jacobs, T., et al. 2018a, MNRAS, 474, 1453, doi: 10.1093/mnras/stx2735

—. 2018b, MNRAS, 474, 1453, doi: 10.1093/mnras/stx2735

—. 2018c, MNRAS, 474, 1453, doi: 10.1093/mnras/stx2735

Rappaport, S., Zhou, G., Vanderburg, A., et al. 2019, MNRAS, 485, 2681, doi: 10.1093/mnras/stz537

Rayner, J. T., Cushing, M. C., & Vacca, W. D. 2009, ApJS, 185, 289, doi: 10.1088/0067-0049/185/2/289

Rebbapragada, U., Protopapas, P., Brodley, C. E., & Alcock, C. 2009, arXiv e-prints, arXiv:0905.3428, doi: 10.48550/arXiv.0905.3428

Reid, I. N., Brewer, C., Brucato, R. J., et al. 1991, PASP, 103, 661, doi: 10.1086/132866

Rein, E., & Ofir, A. 2019, MNRAS, 490, 1111, doi: 10.1093/mnras/stz2556

Ribas, Á., Bouy, H., & Merín, B. 2015, A&A, 576, A52, doi: 10.1051/0004-6361/201424846

Richards, J. W., Starr, D. L., Butler, N. R., et al. 2011, ApJ, 733, 10, doi: 10.1088/0004-637X/733/1/10

Ricker, G. R., Winn, J. N., Vanderspek, R., et al. 2014, in Society of Photo-Optical Instrumentation Engineers (SPIE) Conference Series, Vol. 9143, Space Telescopes and Instrumentation 2014: Optical, Infrared, and Millimeter Wave, ed. J. Oschmann, Jacobus M., M. Clampin, G. G. Fazio, & H. A. MacEwen, 914320, doi: 10.1117/12.2063489

Ricker, G. R., Winn, J. N., Vanderspek, R., et al. 2015, Journal of Astronomical Telescopes, Instruments, and Systems, 1, 014003, doi: 10.1117/1.JATIS.1.1.014003

Rieke, G. H., Su, K. Y. L., Melis, C., & Gáspár, A. 2021a, ApJ, 918, 71, doi: 10.3847/1538-4357/ac0dc4

—. 2021b, ApJ, 918, 71, doi: 10.3847/1538-4357/ac0dc4

Riello, M., De Angeli, F., Evans, D. W., et al. 2021, A&A, 649, A3, doi: 10.1051/0004-6361/202039587

Rizzo Smith, M., Jayasinghe, T., Stanek, K. Z., et al. 2021, The Astronomer's Telegram, 14879, 1

Robinson, E. L. 1976, ARA&A, 14, 119, doi: 10.1146/annurev.aa.14.090176.001003

Rodriguez, A. C., El-Badry, K., Suleimanov, V., et al. 2025, PASP, 137, 014201, doi: 10.1088/1538-3873/ada185

Rodriguez, J. E., Pepper, J., Stassun, K. G., et al. 2013, AJ, 146, 112, doi: 10.1088/0004-6256/146/5/112

Rodriguez, J. E., Stassun, K. G., Lund, M. B., et al. 2016, AJ, 151, 123, doi: 10.3847/0004-6256/151/5/123

Rodriguez, J. E., Zhou, G., Cargile, P. A., et al. 2017, ApJ, 836, 209, doi: 10.3847/1538-4357/aa5da5

Roggero, N., Bouvier, J., Rebull, L. M., & Cody, A. M. 2021, A&A, 651, A44, doi: 10.1051/0004-6361/202140646

Romanova, M. M., Koldoba, A. V., Ustyugova, G. V., et al. 2021, MNRAS, 506, 372, doi: 10.1093/mnras/stab1724

Romanova, M. M., Kulkarni, A. K., & Lovelace, R. V. E. 2008, ApJ, 673, L171, doi: 10.1086/527298

Röser, S., Schilbach, E., & Goldman, B. 2016, A&A, 595, A22, doi: 10.1051/0004-6361/201629158

Rowan, D. M., Stanek, K. Z., Way, Z., et al. 2021, Research Notes of the American Astronomical Society, 5, 147, doi: 10.3847/2515-5172/ac0c83

Rybizki, J., Green, G. M., Rix, H.-W., et al. 2022, MNRAS, 510, 2597, doi: 10.1093/mnras/stab3588

Saito, R. K., Minniti, D., Ivanov, V. D., et al. 2019, MNRAS, 482, 5000, doi: 10.1093/mnras/sty3004

Sánchez-Sáez, P., Reyes, I., Valenzuela, C., et al. 2021, AJ, 161, 141, doi: 10.3847/1538-3881/abd5c1

Sarro, L. M., Debosscher, J., López, M., & Aerts, C. 2009, A&A, 494, 739, doi: 10.1051/0004-6361:200809918

Scargle, J. D. 1982a, ApJ, 263, 835, doi: 10.1086/160554

—. 1982b, ApJ, 263, 835, doi: 10.1086/160554

Scaringi, S., Maccarone, T. J., D'Angelo, C., Knigge, C., & Groot, P. J. 2017, Nature, 552, 210, doi: 10.1038/nature24653

Scaringi, S., Manara, C. F., Barenfeld, S. A., et al. 2016, MNRAS, 463, 2265, doi: 10.1093/mnras/stw2155

Schaefer, B. E. 2016, ApJ, 822, L34, doi: 10.3847/2041-8205/822/2/L34

—. 2018, Journal of Astronomical History and Heritage, 21, 7, doi: 10.48550/arXiv.1808.01862

Schlafly, E. F., Meisner, A. M., & Green, G. M. 2019, ApJS, 240, 30, doi: 10.3847/1538-4365/aafbea

Schlafly, E. F., Green, G. M., Lang, D., et al. 2018, ApJS, 234, 39, doi: 10.3847/1538-4365/aaa3e2

Schlawin, E., Su, K. Y. L., Herter, T., Ridden-Harper, A., & Apai, D. 2021, AJ, 162, 57, doi: 10.3847/1538-3881/ac0b41

Schlegel, D. J., Finkbeiner, D. P., & Davis, M. 1998, ApJ, 500, 525, doi: 10.1086/305772

Schlichting, H. E., & Chang, P. 2011, ApJ, 734, 117, doi: 10.1088/0004-637X/734/2/117

Schmidt, E. G. 2019, ApJ, 880, L7, doi: 10.3847/2041-8213/ab2e77

Sesar, B., Hernitschek, N., Mitrović, S., et al. 2017, AJ, 153, 204, doi: 10.3847/1538-3881/aa661b

Shridharan, B., Mathew, B., Bhattacharyya, S., et al. 2022, A&A, 668, A156, doi: 10.1051/0004-6361/202244353

Silverman, B. W. 1986, Density estimation for statistics and data analysis

Silvia, D. W., & Agol, E. 2008a, ApJ, 681, 1377, doi: 10.1086/588545

—. 2008b, ApJ, 681, 1377, doi: 10.1086/588545

Skrutskie, M. F., Cutri, R. M., Stiening, R., et al. 2006, AJ, 131, 1163, doi: 10.1086/498708

Smart, R. L., & Nicastro, L. 2014, A&A, 570, A87, doi: 10.1051/0004-6361/201424241

Smith, L. C., Koposov, S. E., Lucas, P. W., et al. 2021, MNRAS, 505, 1992, doi: 10.1093/mnras/stab1211

Speagle, J. S. 2020, MNRAS, 493, 3132, doi: 10.1093/mnras/staa278

Stauffer, J., Cody, A. M., McGinnis, P., et al. 2015, AJ, 149, 130, doi: 10.1088/0004-6256/149/4/130

Steele, A., Hughes, A. M., Carpenter, J., et al. 2016, ApJ, 816, 27, doi: 10.3847/0004-637X/816/1/27

Stencel, R. E. 2012, , 40, 618

Stencel, R. E. 2016, in Society of Photo-Optical Instrumentation Engineers (SPIE) Conference Series, Vol. 9907, Optical and Infrared Interferometry and Imaging V, ed. F. Malbet, M. J. Creech-Eakman, & P. G. Tuthill, 990717, doi: 10.1117/12.2231091

Stencel, R. E., Kloppenborg, B. K., Wall, Randall E., J., et al. 2011, AJ, 142, 174, doi: 10.1088/0004-6256/142/5/174

Stephenson, C. B. 1986, PASP, 98, 467, doi: 10.1086/131779

Stolker, T., Quanz, S. P., Todorov, K. O., et al. 2020, A&A, 635, A182, doi: 10.1051/0004-6361/201937159

Stoll, R., Martini, P., Derwent, M. A., et al. 2010, in Society of Photo-Optical Instrumentation Engineers (SPIE) Conference Series, Vol. 7735, Ground-based and Airborne Instrumentation for Astronomy III, ed. I. S. McLean, S. K. Ramsay, & H. Takami, 77354L, doi: 10.1117/12.857893

Strassmeier, K. G. 2009, A&A Rev., 17, 251, doi: 10.1007/s00159-009-0020-6

Stringer, K. M., Long, J. P., Macri, L. M., et al. 2019, AJ, 158, 16, doi: 10.3847/1538-3881/ab1f46

Su, K. Y. L., Jackson, A. P., Gáspár, A., et al. 2019, AJ, 157, 202

Su, K. Y. L., Kennedy, G. M., Schlawin, E., Jackson, A. P., & Rieke, G. H. 2022a, ApJ, 927, 135, doi: 10.3847/1538-4357/ac4bbb

—. 2022b, ApJ, 927, 135, doi: 10.3847/1538-4357/ac4bbb

Su, K. Y. L., Rieke, G. H., Melis, C., et al. 2020, The Astrophysical Journal, 898, 21, doi: 10.3847/1538-4357/ab9c9b

Su, K. Y. L., Jackson, A. P., Gáspár, A., et al. 2019, AJ, 157, 202, doi: 10.3847/1538-3881/ab1260

Su, K. Y. L., Moór, A., Xie, C., et al. 2025, ApJ, 988, L2, doi: 10.3847/2041-8213/ade872

Suárez Mascareño, A., Rebolo, R., & González Hernández, J. I. 2016, A&A, 595, A12, doi: 10.1051/0004-6361/201628586

Szabados, L. 2014, arXiv e-prints, arXiv:1404.1688, doi: 10.48550/arXiv.1404.1688

Theissen, C. A., & West, A. A. 2017, AJ, 153, 165, doi: 10.3847/1538-3881/aa6343

Thompson, M. A., Scicluna, P., Kemper, F., et al. 2016, MNRAS, 458, L39

Tisserand, P. 2012, A&A, 539, A51, doi: 10.1051/0004-6361/201117874

Tisserand, P., Clayton, G. C., Bessell, M. S., et al. 2020, A&A, 635, A14, doi: 10.1051/0004-6361/201834410

Tokovinin, A., & Kiyaeva, O. 2016, MNRAS, 456, 2070, doi: 10.1093/mnras/stv2825

Tonry, J. L., Stubbs, C. W., Lykke, K. R., et al. 2012, ApJ, 750, 99, doi: 10.1088/0004-637X/750/2/99

Toriumi, S., & Wang, H. 2019, Living Reviews in Solar Physics, 16, 3, doi: 10.1007/s41116-019-0019-7

Torres, G., & Sakano, K. 2022, MNRAS, 516, 2514, doi: 10.1093/mnras/stac2322

Tucker, J. M., & Mukhopadhyay, S. 2014, Earth and Planetary Science Letters, 393, 254

Tzanidakis, A., & Bellm, E. C. 2025, Periodicity Analysis in Alert Production, Data Management Technical Note DMTN-221, Vera C. Rubin Observatory

Tzanidakis, A., & Davenport, J. R. A. 2026, ApJ, 1000, L5, doi: 10.3847/2041-8213/ae3ddc

Tzanidakis, A., Davenport, J. R. A., Bellm, E. C., & Wang, Y. 2023, ApJ, 955, 69, doi: 10.3847/1538-4357/aceda7

Tzanidakis, A., Davenport, J. R. A., Caplar, N., et al. 2025, ApJ, 991, 118, doi: 10.3847/1538-4357/adf5bb

Udalski, A., Szymanski, M., Kaluzny, J., Kubiak, M., & Mateo, M. 1992, Acta Astron., 42, 253

van Dam, D. M., & Kenworthy, M. A. 2024a, A&A, 687, A11, doi: 10.1051/0004-6361/202245620

—. 2024b, A&A, 687, A11, doi: 10.1051/0004-6361/202245620

van Groeningen, M. G. J., Castro-Ginard, A., Brown, A. G. A., Casamiquela, L., & Jordi, C. 2023, A&A, 675, A68, doi: 10.1051/0004-6361/202345952

van Roestel, J., Kupfer, T., Ruiz-Carmona, R., et al. 2018, MNRAS, 475, 2560, doi: 10.1093/mnras/stx3291

Vanderbosch, Z. P., Rappaport, S., Guidry, J. A., et al. 2021, ApJ, 917, 41, doi: 10.3847/1538-4357/ac0822

Vanderburg, A., Johnson, J. A., Rappaport, S., et al. 2015a, Nature, 526, 546, doi: 10.1038/nature15527

—. 2015b, Nature, 526, 546, doi: 10.1038/nature15527

Vanderplas, J., Connolly, A., Ivezić, Ž., & Gray, A. 2012, in Conference on Intelligent Data Understanding (CIDU), 47 –54, doi: 10.1109/CIDU.2012.6382200

VanderPlas, J. T., & Ivezić, Ž. 2015, ApJ, 812, 18, doi: 10.1088/0004-637X/812/1/18

Vines, J. I., & Jenkins, J. S. 2022, MNRAS, 513, 2719, doi: 10.1093/mnras/stac956

Vioque, M., Oudmaijer, R. D., Schreiner, M., et al. 2020, A&A, 638, A21, doi: 10.1051/0004-6361/202037731

Virtanen, P., Gommers, R., Oliphant, T. E., et al. 2020, Nature Methods, 17, 261, doi: 10.1038/s41592-019-0686-2

von Neumann, J. 1941a, The Annals of Mathematical Statistics, 12, 367 , doi: 10.1214/aoms/1177731677

—. 1941b, The Annals of Mathematical Statistics, 12, 367 , doi: 10.1214/aoms/1177731677

Wagg, T., Breivik, K., Renzo, M., & Price-Whelan, A. M. 2025, The Astrophysical Journal Supplement Series, 276, 16, doi: 10.3847/1538-4365/ad8b1f

Walton, N. A., Drew, J., Barlow, M. J., et al. 2004, in American Astronomical Society Meeting Abstracts, Vol. 205, American Astronomical Society Meeting Abstracts, 113.03

Watkins, L. L., Evans, N. W., Belokurov, V., et al. 2009, MNRAS, 398, 1757, doi: 10.1111/j.1365-2966.2009.15242.x

Watson, C. L., Henden, A. A., & Price, A. 2006, Society for Astronomical Sciences Annual Symposium, 25, 47

Werner, M. W., Roellig, T. L., Low, F. J., et al. 2004, ApJS, 154, 1, doi: 10.1086/422992

Wetherill, G. W. 1994, Geochim. Cosmochim. Acta, 58, 4513

Wilhite, B. C., Vanden Berk, D. E., Kron, R. G., et al. 2005, ApJ, 633, 638, doi: 10.1086/430821

Williams, J. P., & Cieza, L. A. 2011, ARA&A, 49, 67, doi: 10.1146/annurev-astro-081710-102548

Williams, R. E. 1980, ApJ, 235, 939, doi: 10.1086/157698

Wilson, A. J., Lakeland, B. S., Wilson, T. J., & Naylor, T. 2023, MNRAS, 521, 354, doi: 10.1093/mnras/stad301

Windemuth, D., & Herbst, W. 2014, AJ, 147, 9, doi: 10.1088/0004-6256/147/1/9

Winn, J. N. 2010, in Exoplanets, ed. S. Seager, 55–77, doi: 10.48550/arXiv.1001.2010

WISE Team. 2020, WISE All-Sky Single Exposure (L1b) Source Table, IPAC, doi: 10.26131/IRSA139

Witham, A. R., Knigge, C., Gänsicke, B. T., et al. 2006, MNRAS, 369, 581, doi: 10.1111/j.1365-2966.2006.10395.x

Wood, F. B. 1985a, in NASA Conference Publication, Vol. 2384, NASA Conference Publication, 1–6

Wood, F. B. 1985b, in NASA Conference Publication, Vol. 2384, NASA Conference Publication, 1–6

Woźniak, P. R., Vestrand, W. T., Akerlof, C. W., et al. 2004, AJ, 127, 2436, doi: 10.1086/382719

Wright, E. L., Eisenhardt, P. R. M., Mainzer, A. K., et al. 2010a, AJ, 140, 1868, doi: 10.1088/0004-6256/140/6/1868

—. 2010b, AJ, 140, 1868, doi: 10.1088/0004-6256/140/6/1868

—. 2010c, AJ, 140, 1868, doi: 10.1088/0004-6256/140/6/1868

—. 2019, AllWISE Source Catalog, IPAC, doi: 10.26131/IRSA1

Wright, J. T. 2018, Research Notes of the American Astronomical Society, 2, 16

Wright, J. T., Cartier, K. M. S., Zhao, M., Jontof-Hutter, D., & Ford, E. B. 2016, ApJ, 816, 17, doi: 10.3847/0004-637X/816/1/17

Wright, J. T., & Sigurdsson, S. 2016, ApJ, 829, L3, doi: 10.3847/2041-8205/829/1/L3

Wyatt, M. C. 2008a, ARA&A, 46, 339, doi: 10.1146/annurev.astro.45.051806.110525

—. 2008b, ARA&A, 46, 339, doi: 10.1146/annurev.astro.45.051806.110525

—. 2018, in Handbook of Exoplanets, ed. H. J. Deeg & J. A. Belmonte (Springer Nature), 146, doi: 10.1007/978-3-319-55333-7_146

Wyatt, M. C., & Jackson, A. P. 2016a, Space Sci. Rev., 205, 231, doi: 10.1007/s11214-016-0248-1

—. 2016b, Space Sci. Rev., 205, 231

York, D. G., Adelman, J., Anderson, Jr., J. E., et al. 2000, AJ, 120, 1579, doi: 10.1086/301513

Zackay, B., Ofek, E. O., & Gal-Yam, A. 2016, ApJ, 830, 27, doi: 10.3847/0004-637X/830/1/27

Zakamska, N. L., Adamane Pallathadka, G., Bizyaev, D., et al. 2025a, arXiv e-prints, arXiv:2507.05367, doi: 10.48550/arXiv.2507.05367

—. 2025b, arXiv e-prints, arXiv:2507.05367, doi: 10.48550/arXiv.2507.05367

Zhang, J., Xiang, M., Yu, J., et al. 2024, ApJS, 272, 40, doi: 10.3847/1538-4365/ad41b6

Zhu, W., Bernhard, K., Dai, F., et al. 2022, ApJ, 933, L21, doi: 10.3847/2041-8213/ac7b2d

Ziegler, C., Tokovinin, A., Briceño, C., et al. 2020, AJ, 159, 19, doi: 10.3847/1538-3881/ab55e9